PEOPLE'S DEMOCRATIC REPUBLIC OF ALGERIA
Ministry of Higher Education and Scientific Research
University of Mohamed El Bachir El Ibrahimi
Faculty of Science and Technology
Department of Electronics

DOCTORAL THESIS
Presented to obtain the degree of **DOCTOR**
In: Electronics
Specialty: Medical Electronics
By: Abdelghani TAKHA

Topic

Contribution to the Modeling of Non-Stationary Biomedical Signals

Publicly defended, on **09/07/2025**, before a jury composed of:

Mr. Farid BOUTTOUT	Professor	at UBBA	President
Mr. Mohamed L.TALBI	Professor	at UBBA	Thesis Director
Mr. Philippe RAVIER	Professor	at univ-orleans-France	Thesis Co-Director
Mrs. Zoubeida MESSALI	Professor	at UBBA	Examinator
Mr. Amar MEZACHE	Professor	at UM'sila	Examinator
Mr. Houcine OURIDA	Professor	at UM'sila	Examinator

Abstract

This thesis explores the application of fractional-order calculus to the modeling of non-stationary biomedical signals, with a particular focus on electrocardiogram (ECG) signals. Traditional ECG models based on integer-order differential equations, such as the widely used McSharry model, provide a solid foundation for synthetic ECG generation but often fall short in capturing the long-memory and complex dynamics inherent in physiological signals. To address these limitations, this work extends classical models by incorporating fractional differential equations (FDEs), which enable the representation of memory and hereditary properties intrinsic to biological systems.

The proposed fractional-order ECG model integrates fractional derivatives into the McSharry framework, enhancing its flexibility and accuracy while preserving essential morphological features of the PQRST complex. The Predictor-Corrector method is employed for numerically solving the fractional differential equations, and Genetic Algorithms are utilized for robust parameter optimization. This hybrid approach allows for precise tuning of model parameters, resulting in synthetic ECG signals that closely fit real physiological data.

Extensive numerical simulations were conducted and validated against clinical ECG recordings from the MIT-BIH Arrhythmia Database. The fractional-order model demonstrated a significant improvement over the classical integer-order model, achieving a 48.40% reduction in mean squared error (MSE) and a 23.18% increase in compression efficiency across five distinct heartbeat types. The optimized fractional orders ($alpha$) consistently ranged between 0.96 and 0.99, indicating that subtle deviations from integer order substantially enhance model performance.

In addition to fractional modeling, this thesis contributes novel methodologies including the integration of Hopf bifurcation dynamics into the ECG generation process to simulate realistic cardiac rhythms and the application of the Grey Wolf Optimizer for efficient parameter estimation. These advancements further improve the fidelity of synthetic

ECG signals and broaden the scope of arrhythmia simulation.

Overall, the findings underscore the potential of fractional-order models combined with advanced optimization techniques to advance biomedical signal processing. This framework facilitates more accurate simulation, analysis, and classification of complex non-stationary physiological signals, with significant implications for computational cardiology, personalized healthcare, and the development of automated diagnostic tools.

Résumé

Cette thèse explore l’application du calcul fractionnaire à l’étude des signaux biomédicaux non stationnaires, avec un accent particulier sur les signaux électrocardiogramme (ECG). Les modèles traditionnels d’ECG basés sur des équations différentielles d’ordre entier, tels que le modèle largement utilisé de McSharry, constituent une base solide pour la génération synthétique d’ECG, Toutefois, ils peinent souvent à capturer la mémoire longue et la complexité dynamique inhérentes aux signaux physiologiques. Pour pallier ces limitations, ce travail étend les modèles classiques en intégrant des équations différentielles fractionnaires (EDF), permettant ainsi de représenter les propriétés de mémoire et d’hérédité propres aux systèmes biologiques.

Le modèle ECG proposé d’ordre fractionnaire intègre des dérivées fractionnaires dans le cadre du modèle de McSharry, améliorant sa flexibilité et sa précision tout en préservant les caractéristiques morphologiques essentielles du complexe PQRST. La méthode prédicteur-correcteur est employée pour la résolution numérique des équations différentielles fractionnaires, tandis que des algorithmes génétiques sont utilisés pour une optimisation robuste des paramètres. Cette approche hybride permet un ajustement précis des paramètres du modèle, produisant des signaux ECG synthétiques qui reproduisent fidèlement les données physiologiques réelles.

Des simulations numériques étendues ont été réalisées et validées par comparaison avec des enregistrements cliniques issus de la base de données MIT-BIH Arrhythmia. Le modèle d’ordre fractionnaire a démontré une amélioration significative par rapport au modèle classique d’ordre entier, avec une réduction de 48,40% de l’erreur quadratique moyenne (MSE) et une augmentation de 23,18% de l’efficacité de compression sur cinq types de battements cardiaques distincts. Les ordres fractionnaires optimaux (a) se situaient systématiquement entre 0,96 et 0,99, indiquant que de subtiles déviations par rapport à l’ordre entier améliorent considérablement la performance du modèle.

Outre la modélisation fractionnaire, cette thèse apporte des contributions méthodologiques

novatrices, notamment l'intégration de la dynamique de bifurcation de Hopf dans le processus de génération d'ECG pour simuler des rythmes cardiaques réalistes, ainsi que l'application de l'optimiseur Grey Wolf pour une estimation efficace des paramètres. Ces avancées renforcent la fidélité des signaux ECG synthétiques et élargissent le champ de simulation des arythmies.

Dans l'ensemble, les résultats soulignent le potentiel des modèles d'ordre fractionnaire combinés à des techniques d'optimisation avancées pour faire progresser le traitement des signaux biomédicaux. Ce cadre offre une simulation, une analyse et une classification plus précises des signaux physiologiques complexes et non stationnaires, avec des implications majeures pour la cardiologie computationnelle, les soins personnalisés et le développement d'outils diagnostiques automatisés.

ملخص

تتناول هذه الرسالة البحثية تطبيق حساب التفاضل والتكامل الجزئي في نمذجة الإشارات الطبية غير الثابتة، مع تركيز خاص على إشارات تخطيط القلب الكهربائي (ECG). تعتمد النماذج التقليدية لتخطيط القلب على معادلات تفاضلية ذات ترتيب صحيح، مثل نموذج ماكشاري الشهير، والتي توفر أساسًا قويًا لتوليد إشارات ECG تركيبية، لكنها غالبًا ما تعجز عن التقاط خصائص الذاكرة الطويلة والديناميكيات المعقدة المتأصلة في الإشارات الفسيولوجية. وللتغلب على هذه القيود، توسع هذه الدراسة النماذج الكلاسيكية من خلال دمج المعادلات التفاضلية الجزئيّة التي تتيح تمثيل خصائص الذاكرة والوراثة المميزة للأنظمة البيولوجية.

يُدمج النموذج المقترح لتخطيط القلب ذو الترتيب الجزئي مشتقات كسريّة ضمن إطار نموذج ماكشاري، مما يعزز من مرونته ودقته مع الحفاظ على الخصائص الشكلية الأساسية لمركب PQRST. تم استخدام طريقة المتنبئ-المصحح للحل العددي للمعادلات التفاضلية الجزئيّة، إلى جانب خوارزميات جينية لتحسين المعاملات بشكل قوي. تتيح هذه المنهجية المختلطة ضبطًا دقيقًا لمعاملات النموذج، مما ينتج إشارات ECG تركيبية تحاكي بدقة البيانات الفسيولوجية الحقيقية.

أُجريت محاكاة عددية موسعة وتم التحقق من صحتها بالمقارنة مع تسجيلات سريرية مأخوذة من قاعدة بيانات MIT-BIH Arrhythmia. أظهر النموذج ذو الترتيب الجزئي تحسنًا ملحوظًا مقارنة بالنموذج التقليدي، حيث حقق انخفاضًا بنسبة ٠٤.٨٤٪ في متوسط الخطأ التربيعي (MSE) وزيادة بنسبة ٨١.٣٢٪ في كفاءة الضغط عبر خمسة أنواع مختلفة من ضربات القلب. تراوحت القيم المحسّنة للترتيب الجزئي بين ٦٩.٠ و٩٩.٠، مما يشير إلى أن الانحرافات الطفيفة عن الترتيب الصحيح تعزز بشكل كبير أداء النموذج.

بالإضافة إلى النمذجة الجزئيّة، تقدم هذه الرسالة إسهامات منهجية جديدة، تشمل دمج ديناميكيات تفرّع هوبف في عملية توليد إشارات ECG لمحاكاة الإيقاعات القلبية الواقعية، وتطبيق خوارزمية الذئب الرمادي لتحسين فعّال لمعاملات النموذج. تعزز هذه التطورات من دقة الإشارات التركيبية وتوسع نطاق محاكاة اضطرابات نظم القلب.

بشكل عام، تؤكد النتائج على إمكانات النماذج ذات الترتيب الجزئي المدمجة مع تقنيات

تحسين متقدمة في تطوير معالجة الإشارات الطبية. يوفر هذا الإطار محاكاة وتحليل وتصنيفاًا أكثر دقة للإشارات الفسيولوجية المعقدة وغير الثابتة، مع تأثيرات كبيرة في مجال القلب الحاسوبي، والرعاية الصحية الشخصية، وتطوير أدوات التشخيص الآلي.

Dedication

I would like to express my deepest gratitude to Allah for blessing me with the faith, strength, courage, and patience to complete this thesis.

I wholeheartedly dedicate this humble work to my beloved parents, siblings, and entire family, whose unwavering support, constant encouragement, and sincere prayers have been a guiding light and a pillar of strength throughout this journey.

To my beloved wife and precious daughter, Alaa Erahmanae — your presence brings joy, meaning, and purpose to my life. Your love, patience, and unshakable belief in me have been an enduring source of motivation.

This achievement is not mine alone; I share it with all of you, with deep appreciation and love.

Acknowledgment

I would like to express my sincere gratitude to my supervisor, **Professor Mohamed Lamine TALBI** from the University of Bordj Bou Arréridj, for his unwavering trust and continuous support. His humility, insightful guidance, valuable advice, and generous companionship—both as a mentor and as a brother—have played a pivotal role in the development and successful completion of this thesis.

I also extend my heartfelt thanks to my co-supervisor, **Professor Philippe RAVIER** from the University of Orléans, France, for his expert guidance, patience, and unwavering support. His deep insights and thoughtful reflections have significantly enhanced the quality and depth of this work.

I am deeply grateful to my esteemed examiners: **Professor Farid BOUTTOUT, Professor Zoubeida MESSALI, Professor Amar MEZACHE**, and **Professor Houcine OURIDA**. It has been a true honor to have my work evaluated by such distinguished scholars, whose constructive feedback and academic rigor have contributed meaningfully to the refinement of this thesis

Table of contents

List of Abbreviations

CORR correlation coefficient

CR Compression Ratio

ECG Electrocardiogram

EEG Electroencephalogram

EMG Electromyogram

ENG Electroneurogram

FDEs Fractional Differential Equations

GA Genetic Algorithm

GL Grünwald–Letnikov

GWO Grey Wolf Optimizer

IDE Integer-order Differential Equation

MAE Mean Absolute Error

MIT-BIH MIT–Beth Israel Hospital Arrhythmia Database

MSE Mean Squared Error

NRMSE Normalized Root Mean Square Error

PC Predictor-Corrector

PCG Phonocardiogram

PRD Percent Root-Mean-Square Difference

QS Quality Score

RL Riemann-Liouville

RMSE Root Mean Square Error

VIES Volterra Integral Equations

List of Figures

List of Tables

General Introduction

The human body's function is often linked to electrical, chemical, or auditory signals. Such signals provide information that may not be immediately discernible but is concealed inside the signal's structure. This information must be "decoded" or retrieved before the signals are assigned meaningful interpretations. These signals reflect the underlying physiological characteristics of their respective biological systems, and their interpretation has proven beneficial in elucidating and diagnosing numerous disease situations.The decoding procedure can occasionally be uncomplicated and require minimal manual effort, such as visually inspecting the signal on a printed page or computer display. Nonetheless, the intricacy of a signal is frequently substantial, making biomedical signal processing an essential instrument for extracting therapeutically relevant information concealed within the signal. Biomedical signal processing constitutes an interdisciplinary field. Understanding human physiology is essential to prevent the development of an analytical procedure that distorts or eliminates critical information.[1]

A comprehensive understanding of anatomy, linear algebra, mathematics, statistics, and circuit design is also advantageous.

Some regard biomedical signal processing as a precursor to creating diagnostic systems that provide entirely automated analysis. Automation was the primary objective when computers entered the medical field several decades ago. This objective has significantly evolved over the years, not only due to the intrinsic challenges of building such systems but also because the physician must ultimately bear responsibility for the diagnostic conclusions made. Although complete analysis automation may be justified in certain circumstances, today's objective is to create computer systems that support physicians in making informed decisions. In these systems, biological signal processing has assumed a crucial role.

Biomedical signal processing involves acquiring and interpreting signals from biological and physiological systems. As important diagnostic instruments for clinicians and researchers, these signals offer essential insights into living organisms' conditions and functions. Nonetheless, their study is complicated by the intricacy of the fundamental biological systems, vulnerability to noise, and intrinsic unpredictability over time. [1].

Biomedical signals are generally acquired using noninvasive measurements and display a blend of localized features, such as spikes, and more widespread ones, such as oscillations. This complexity requires signal processing methods to manage various time-frequency localization demands [8, 9].

Signals can be categorized into deterministic and non-deterministic (random) types. Deterministic signals have a known pattern and may be clearly defined as time functions. In contrast, random signals possess intrinsic uncertainty, necessitating probabilistic and statistical methods for their interpretation. A signal is deemed non-stationary when its statistical features, including mean and variance, fluctuate over time . These signals, distinguished by their time-varying spectral characteristics, necessitate particular analytical methods. Numerous real-world biological signals, such as Electrocardiogram (ECG), Electroencephalogram (EEG), Electromyogram (EMG), Electroneurogram (ENG), and Phonocardiogram(PCG), are fundamentally non-stationary. Adequate study of these signals yields essential physiological data, facilitating progress in healthcare diagnoses. Efficiently analyzing and deriving significant insights from such signals enables the creation of more precise and noninvasive diagnostic instruments.

Notwithstanding its importance, analyzing non-stationary signals poses substantial difficulties. Numerous real-world signals have overlapping structures and multi-component attributes, rendering conventional analysis approaches insufficient. An optimal signal processing framework should represent time and frequency domains, measure time-dependent fluctuations, and efficiently distinguish overlapping components. [10].

Mathematical signal modelling and simulation are significant objectives in biological signal processing. By appropriately defining model equations, one can simulate signals that mimic those captured at the cellular level or on the body's surface, thereby providing insights into the correlation between model parameters and the properties of the observed signals. Bioelectrical models encompass representations of the head and brain for the localization of neural activity and models of the thorax and heart for modelling various cardiac rhythms. Signal modelling is fundamental to "model-based signal processing," wherein algorithm development optimizes a chosen performance criterion [1].

The mathematical modeling of biological signals is thoroughly explored. Conventional methods frequently depend on deterministic differential equations; however, new studies have underscored the benefits of fractional calculus in representing long-term memory effects and intricate dynamics. Fractional calculus, an extension of classical calculus, facilitates differentiation and integration of arbitrary orders, rendering it especially advantageous for modeling biological systems that display memory and hereditary characteristics.

ECG signals are essential in cardiovascular research for identifying cardiac diseases because of their simplicity, cost-effectiveness, and noninvasive characteristics. They represent the heart's electrical activity and can signify cardiac disorders, including arrhythmias and myocardial infarctions. However, ECG signals are frequently affected by noise, exhibit individual variability, and are difficult to interpret, requiring the implementation of robust computer-aided analytic techniques.

The mathematical modeling of ECG signals has been extensively studied. Initial models depended on differential equations and nonlinear dynamic systems, including Van der Pol oscillators, Markov chains, and reaction-diffusion systems [11–24]. Nonetheless, these models frequently inadequately portray the intricate nature of ECG waveforms, especially in depicting diseased changes.

Recent studies have included fractional calculus in ECG simulation to address these constraints [25, 26]. Fractional-order models offer more flexibility and precision by incorporating memory effects and intricate dynamics. Numerous research studies have investigated fractional differential equations (FDEs) for ECG signal generation, highlighting their potential for enhanced accuracy and flexibility [27–31].

Our research improves current ECG models by integrating fractional-order derivatives into McSharry's established integer-order framework. The suggested model comprises three interconnected fractional differential equations for generating realistic synthetic ECG signals. The Predictor-Corrector (PC) approach solves the FDEs, whereas the Genetic Algorithm (GA) facilitates practical parameter estimation. This approach enhances ECG signal synthesis by accurately representing both normal and pathological waveforms through fractional calculus.

Advancements in fractional-order ECG modeling present considerable potential for clinical applications, facilitating enhanced diagnosis, monitoring, and individualized healthcare solutions.

The first contribution of this research is the generation of synthetic ECG signals. We present a modeling technique for generating synthetic ECG signals that exhibit realistic PQRST architecture and specified heart rate dynamics, encompassing diverse cardiac arrhythmias. The model consists of three interconnected ordinary differential equations, with the initial two equations integrating Hopf bifurcation. The fourth-order Runge-Kutta method is employed for numerical simulation. The results illustrate the model's capability to produce diverse synthetic ECG signals, encompassing standard and arrhythmic patterns. A visual analysis of authentic ECG signals from the MIT-BIH Arrhythmia Database was performed to ascertain suitable model parameters.

The second contribution involves the optimization of ECG signal simulation using the Grey Wolf Optimizer (GWO). Specifically, we optimize the parameters of a synthetic ECG generator based on a system of three differential equations. This enhancement significantly improves the fidelity of the simulated ECG waveforms in comparison with real signals from the MIT-BIH database. The GWO-based optimization approach effectively tunes the model parameters, ensuring higher accuracy in reproducing ECG signals. A comparative analysis with actual ECG recordings confirms the effectiveness of this strategy in enhancing simulation performance.

The third contribution is Fractional-Order ECG Modeling for Improved Representation. We offer a novel approach for modeling ECG waveforms with FDEs. Integrating fractional calculus into the established McSharry model enhances signal representation and modeling accuracy. A hybrid optimization strategy that integrates the Predictor-Corrector method for solving Functional Differential Equations with Genetic Algorithms for parameter optimization ensures effective parameter estimation.

A comparative investigation demonstrates that our fractional-order model surpasses the conventional McSharry Integer Differential Equation (IDE) model, enhancing modeling quality by 48.40% in mean squared error (MSE) and compression efficiency by 23.18%

when applied to five-beat patterns from the MIT-BIH. The fractional-order model preserves the essential features of the McSharry model while improving its adaptability for diverse cardiac situations.

This manuscript comprises four chapters, along with an introduction and a conclusion.

Chapter 1: Introduction to Non-Stationary Biomedical Signals.

Chapter 2: Foundations of Fractional Calculus and Differential Equation Theory.

Chapter 3: Mathematical Modeling of ECG signal.

Chapter 4: Integer-Order Differential Equation Models for ECG Signal Generation.

Chapter 5: ECG Modeling Using Fractional Differential Equations (FDEs).

Chapter 1

Introduction to Non-Stationary Biomedical Signals

1.1 Introduction

Biomedical signals are crucial in understanding physiological processes, diagnosing diseases, and monitoring patient health. Bioelectrical signals such as the ECG, EEG, ENG, and EMG are widely used in clinical and research settings. These signals are inherently non-stationary, meaning their characteristics vary over time due to physiological changes, external influences, and pathological conditions.

This chapter provides an overview of non-stationary biomedical signals, with a particular focus on the ECG, as it forms the core of this study in subsequent chapters. After discussing the fundamentals of bioelectrical signals and their physiological origins, we explore the principles underlying ECG signal generation, acquisition, and processing. Key topics include cardiac electrical activity, ECG recording techniques, heart rhythm analysis, and regular and pathological patterns. Additionally, this chapter highlights the challenges associated with the non-stationarity of these signals, such as variability, noise, and dynamic fluctuations, thus emphasizing the need for advanced signal processing techniques.

While other biomedical signals, including the phonocardiogram (PCG), have significant diagnostic applications, the focus remains on the ECG due to its relevance to the modeling objectives of this research. This foundation provides the basis for the subsequent chapters, which will delve deeper into mathematical modeling and computational approaches for ECG analysis and interpretation.

1.2 Fundamentals of Bioelectrical Signals

This manuscript dissertation focuses on modeling of non-stationary biomedical signals, which requires comprehension of the biological origins of bioelectrical signals. These signals originate from ionic processes influenced by the electrochemical activity of excitable cells, essential for brain communication, heart function, and muscular contractions.

Although excitable cells perform many physiological tasks, they possess fundamental electrical mechanisms that control signal transmission in the nervous system and regulate vital processes such as cardiac rhythm and muscular activity.Understanding these mechanisms is crucial for developing accurate signal models, particularly for non-stationary biological signals.

This chapter prioritizes signal modeling, offering only a brief introduction to the physiological foundation of bioelectrical signals. Readers interested in a comprehensive examination of cellular and physiological processes are referred to specialized literature [32, 33], whereas essential mathematical modeling principles and biomedical signal processing techniques are elaborated in [34–37].

1.2.1 At the Cellular Level

The generation of bioelectrical signals originates from the selective permeability of the cell membrane, which allows ions such as sodium (Na^+), potassium (K^+), and chloride (Cl^-), to move across it. This ion movement establishes a transmembrane potential, typically ranging from -60 mV to -100 mV depending on the cell type (Fig 1.1).

When a stimulus exceeds a threshold, rapid changes in membrane permeability generate an action potential—a nonlinear, all-or-nothing response involving depolarization (membrane potential reverses) and repolarization (return to resting potential).

Action potential durations vary due to a plateau phase: approximately 1 ms in neurons and up to 300 ms in cardiac cells. This mechanism ensures the propagation of the electrical signal along excitable tissues, maintaining continuity without degradation—a foundational process for understanding cardiac electrophysiology and ECG signal formation.

1.2.2 On the External Body Surface

In excitable cells, action potentials produce currents propagating through adjacent conductive tissue, creating a volume conductor. Bioelectrical signals can be recorded noninvasively using electrodes on the body's surface. Clinical recordings generally employ many electrodes to capture spatial variations in electrical activity; however, noninvasive techniques cannot directly resolve intricate cellular characteristics.

Despite these limitations, analyzing bioelectrical signals from the body's surface has proven significant for clinical decision-making. Modeling the source as a dipole while considering the body's geometric and resistive attributes helps relate cellular activity to

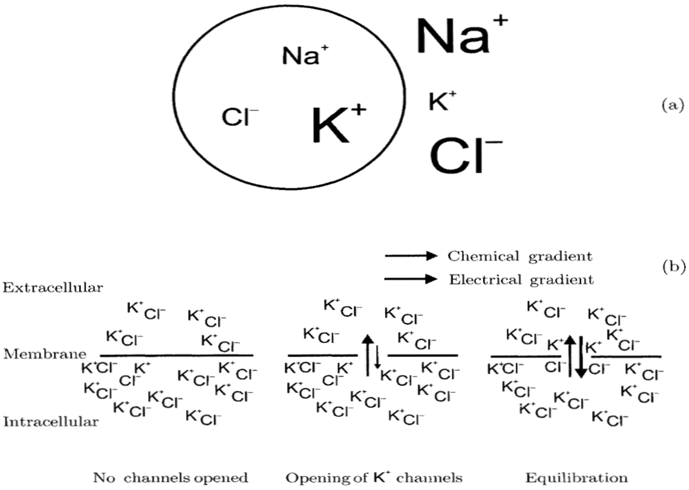

Figure 1.1: Ion Dynamics and Membrane Behavior: Potassium Channel Activity
(a) Distribution of K^+, Na^+, and Cl^- ions across the cellular membrane.
(b) Interplay between chemical and electrical gradients in K^+ ion transport. [1].

recorded signals. The inverse problem, which involves determining the electrical source based on body surface measurements, remains a major challenge in biomedical modeling (Fig1.2).

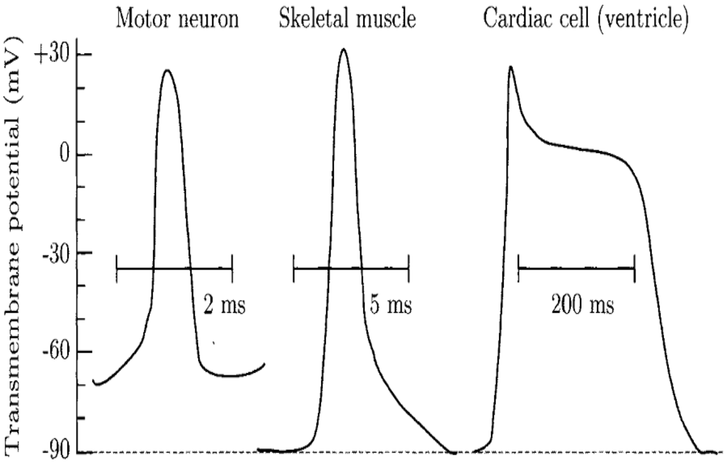

Figure 1.2: Illustrations of action potentials display forms ranging from the spikelike waveform typical of a nerve cell (left) to the somewhat extended waveform of a cardiac cell (right). The transmembrane potential difference was evaluated by placing one microelectrode inside the cell and another outside. The duration differs among various waveforms. [1].

1.2.3 Bioelectrical Signals

Bioelectrical signals represent activities of the brain, heart, and muscles. Some signals, like those from the brain, display continuous activity, while others arise solely from external stimuli. The diverse nature of these signals requires tailored processing approaches. Sometimes, a single waveform indicates a clinical condition, while other cases demand the analysis of multiple waveforms to achieve a significant interpretation.

Electroencephalogram (EEG)
EEG captures the brain's electrical activity through scalp electrodes see Figure 1.3(a) and is commonly used to diagnose cerebral illnesses, including epilepsy and sleep disorders. For higher precision, electrodes may be placed directly on the brain's surface (electrocorticogram, ECoG).

Evoked potentials (EPs) measure cerebral responses to sensory stimuli, assisting in identifying visual pathway and brainstem disorders. Due to their minimal amplitudes, EPs are often imperceptible against the EEG background see Figure 1.4(a).

Electrocardiogram(ECG)
The ECG records the heart's electrical activity via electrodes on the chest, arms, and legs see Figure 1.3(b). With each heartbeat, electrical impulses regulate rhythm and contract the heart muscle to circulate blood. ECG is essential for diagnosing cardiac conditions like myocardial infarction.

Intracardiac electrograms (EGs)—recorded from electrodes inside the heart—are used in pacemakers and defibrillators.

Electromyography (EMG)
EMG measures skeletal muscle electrical activity, identifying neuromuscular conditions such as muscular dystrophy or nerve injuries. Surface EMG uses skin electrodes, while intramuscular EMG involves needle insertion see Figure 1.3(c).

Electroneurogram (ENG)
ENG measures nerve signal propagation velocity. It is primarily used to assess nerve damage and conduction efficiency.

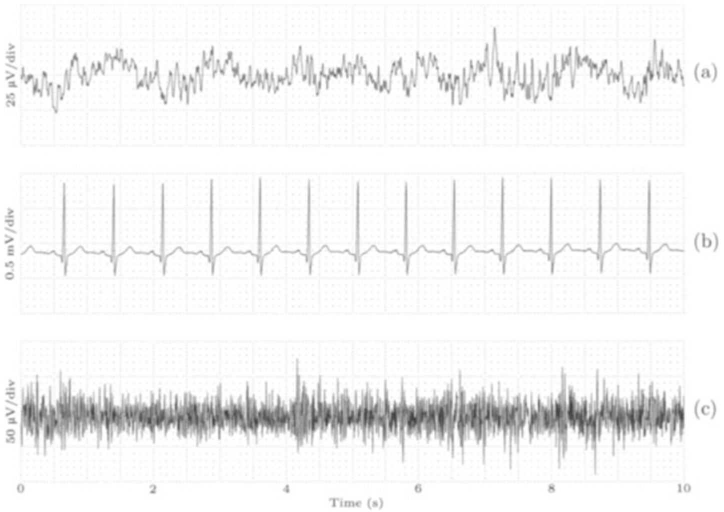

Figure 1.3: Representative examples of the three main types of bioelectrical signals measured at the body surface [2]:
(a) EEG signal showing alpha wave patterns,
(b) ECG signal indicating normal sinus rhythm,
(c) EMG signal collected from the chin during wakefulness.
Each trace was obtained from a different healthy subject.

Electroneurogram (ENG)

The ENG records nerve conduction velocity (NCV) by stimulating a peripheral nerve and capturing responses at two points along its trajectory. By calculating latency differences between the recordings, nerve conduction velocity is estimated see Fig 1.4(b).

ENG findings, such as reduced compound motor action potential (CMAP) amplitudes and slowed conduction velocity, indicate axonal injury characteristic of critical illness polyneuropathy (CIP). These changes may appear early during intensive care [38, 39]

Standard conduction velocity values include: :

- 45–70 m/s in nerve fibers
- 0.2–0.4 m/s in cardiac muscle
- 0.03–0.05 m/s in atrioventricular conduction fibers [40]

A reduction in conduction velocity frequently signifies neurological disorders.

Electroretinogram(ERG)

ERG measures retinal responses to light stimulation, assessing the function of rods and cones. It helps diagnose retinal disorders, including arteriosclerosis or detachment (Figure

1.4(c)).

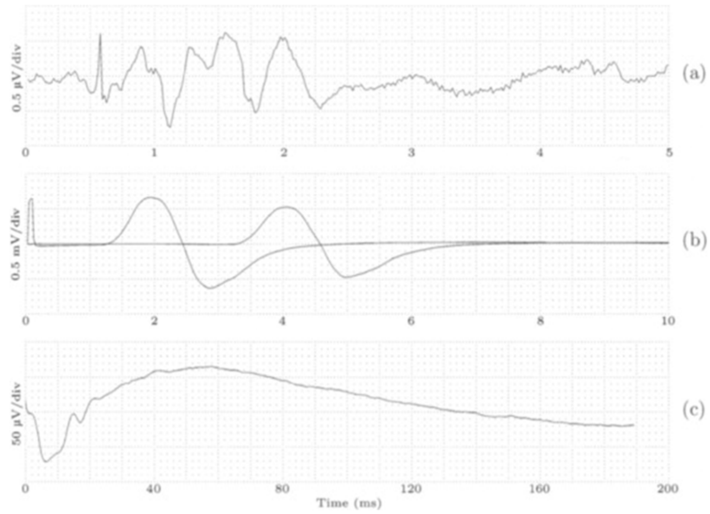

Figure 1.4: Examples of bioelectrical signals elicited by stimulation [1]:
(a) Evoked potential (EP) from auditory stimulation (brainstem response).
(b) ENG recordings used to estimate nerve conduction velocity.
(c) ERG recorded after a light flash stimulus.

Electrooculogram(EOG)

EOG measures the corneal-retinal potential linked to eye movements, assisting in gaze direction tracking and sleep studies (Figure 1.5(a)). It is also beneficial in virtual reality and artifact removal from EEG signal processing.

Electrogastrogram (EGG)

EGG records stomach muscle electrical activity to study gastric motility (Figure 1.5(b)). It detects abnormalities when the stomach fails to empty properly. In healthy individuals, gastric rhythms increase post-meal; symptomatic patients show irregular patterns.

1.2.4 Databases

Biomedical signal databases are critical for developing and testing signal processing algorithms. These datasets support robust modeling across diverse waveforms, enabling generalization and validation.

Biomedical signal databases is essential for developing and evaluating signal processing algorithms, ensuring robustness across diverse waveform patterns. To prevent algorithmic bias, datasets are typically divided into training and evaluation subsets.

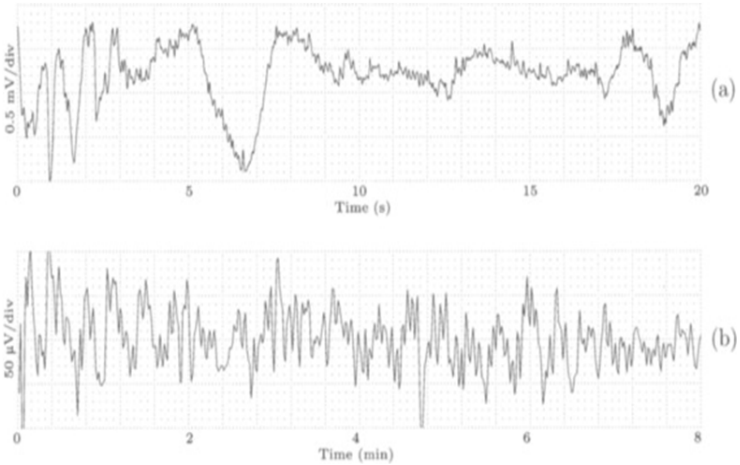

Figure 1.5: (a) EOG recording from the right eye.
(b) EGG showing stomach muscle activity. Note that the two timescales differ. [1].

A standardized database contains recorded signals from healthy subjects and patients, ranging from single modalities (e.g., EEG, ECG) to multimodal datasets combining brain, heart, and respiratory activity. Annotations—manually labeled by clinicians —highlight physiological and non-physiological events (e.g., heartbeats, seizures, noise artifacts). Multiple annotators increase reliability, though discrepancies require consensus. Additional metadata (e.g., age, weight, medications) enhances dataset utility.

Several databases support specific clinical and modeling applications:

- **MIT-BIH Arrhythmia Database** — widely used for cardiac rhythm detection [41, 42].
- **AHA Database** — evaluates ventricular arrhythmia detectors [43].
- **European ST-T and LTST Databases** — focus on ischemia detection [44, 45].
- **MIT-BIH Noise Stress Test Database** — tests algorithm robustness with controlled noise [46].

Multimodal biomedical datasets—such as MIMIC, IBIS, and IMPROVE—include continuously recorded signals from ICU monitoring and sleep studies [47, 48]. While many are publicly available (e.g., via PhysioNet)[49], others remain private. These datasets are essential for both research and medical device development.

However, reusing datasets beyond their intended clinical scope poses risks. Excluding medical experts may cause misinterpretation, while improper repurposing could yield flawed results. Researchers must collect new data when necessary to maintain scientific rigor.

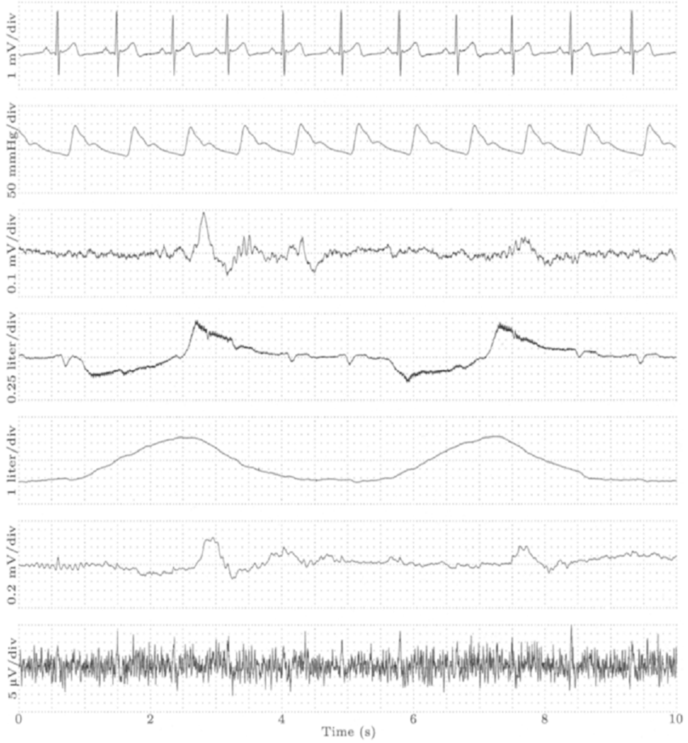

Figure 1.6: Simultaneously recorded signals from a multimodal database: ECG, blood pressure, EEG, nasal and abdominal respiration, EOG, and EMG. This method supports sleep disorder studies (MIT-BIH polysomnographic database) [47].

1.3 The electrocardiogram (ECG)

The ECG is a fundamental diagnostic tool that captures the heart's electrical activity using surface electrodes. These electrodes detect voltage fluctuations from cardiac action potentials, generating waveforms that reveal cardiac diseases and offer insights into cardiac function.

The ECG technique began with Augustus Waller's recordings in the 1880s. Willem Einthoven revolutionized the method using a string galvanometer and standardized electrode positions, earning the 1924 Nobel Prize in Medicine. Modern ECGs are applied in resting, ambulatory, and stress-testing contexts, relying on advanced signal processing techniques [50]. Recent advancements allow detection of subtle rhythm variations and micro-potentials, increasing diagnostic precision.

Recording setups vary:

- **Basic rhythm analysis uses fewer electrodes**
- **Waveform morphology assessments require 10 electrodes**
- **Body surface mapping may employ 100–200 electrodes for high-resolution imaging** [51, 52]

Body surface potential mapping improves detection of local gradients that standard systems might overlook [53].

Electrograms, recorded via intracardiac catheters or implanted electrodes, provide higher spatial resolution. They are critical in localizing arrhythmic regions, guiding pacemaker implantation, and enabling implantable cardioverter defibrillators (ICDs) to detect and treat life-threatening arrhythmias with high-energy shocks [54].

1.3.1 Cardiac Electrical Activity

The heart, a muscular pump, circulates oxygenated blood through rhythmic contractions. It comprises two symmetrical sides, each with an atrium and a ventricle, separated by the septum see Figure **??**(a). Four valves ensure unidirectional blood flow.

The myocardium, rich in myocytes, contracts in response to electrical signals from the sinoatrial (SA) node, the heart's natural pacemaker.

Each cardiac cycle involves:

- **Depolarization (electrical activation and contraction)**
- **Repolarization (electrical recovery and relaxation)**

Depolarization starts with rapid voltage changes in cardiac cells, propagating through the conduction system (Figure **??**(b)). The electrical impulse:

- **Triggers atrial contraction**

- **Passes through the atrioventricular (AV) node (delaying to optimize ventricular filling)**
- **Continues via the bundle of His and Purkinje fibers, ensuring coordinated ventricular contraction**

Conduction velocity varies from 0.05 m/s at the AV node to 4 m/s in the Purkinje fibers.

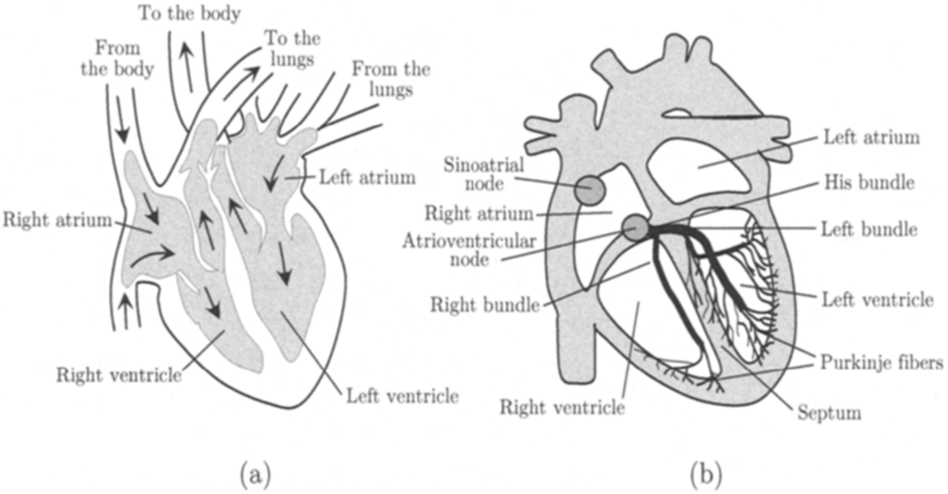

Figure 1.7: Schematic representation of (a) the anatomical structure of the heart (the arrows indicate the pathways of blood flow into and out of the heart) and (b) its electrical conduction system. [1]

The SA node regulates the heart rate via automaticity, while the autonomic nervous system modulates it. Parasympathetic activation reduces, and sympathetic stimulation increases heart rate. The refractory period (200–250 ms) limits maximum rates to about 240–300 bpm; however, young individuals seldom exceed 220 bpm in practice. Maximum heart rate declines with age.

The ECG provides a non-invasive assessment of the heart's electrical activity, reflecting the sum of extracellular currents from millions of cardiac cells. It represents depolarization and repolarization as waveform deflections from baseline, with depolarization waves appearing steeper than repolarization.

1.3.1.1 Generation and Recording of an ECG

During the cardiac cycle, groups of myocardial cells depolarize simultaneously, forming equivalent current dipole vectors. These vectors sum to create a dominant vector representing the primary electrical impulse direction (see Figure 1.8).

The body surface ECG waves reflect these vector changes during depolarization and repolarization phases (see Figure 1.9).

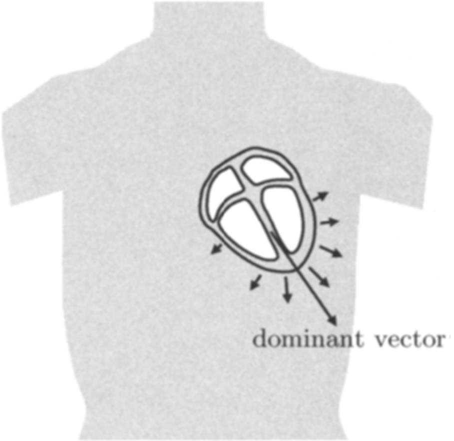

Figure 1.8: During depolarization and repolarization, the vector linked to each cluster of myocardial cells can be aggregated into a principal vector that delineates the primary direction of the electrical impulse.[1]

At rest, the heart is in an isoelectric state. Atrial depolarization, initiated by the SA node, produces a small positive wave due to the atria's low muscle mass (see Figure 1.9(b)). After an AV nodal delay, ventricular depolarization begins at the septum, producing a negative wave, followed by a strong left-ventricle-directed vector due to its larger mass —this generates positive ECG waves (see Figures 1.9(d-g)).

Ventricular repolarization follows, producing a positive T wave (see Figure 1.9(h)). Atrial repolarization is masked by stronger ventricular signals.

1.3.2 ECG Recording Techniques

The ECG records spatial and temporal changes in the heart's electrical activity using electrodes. A lead represents the potential difference between electrode pairs. Two main types exist:

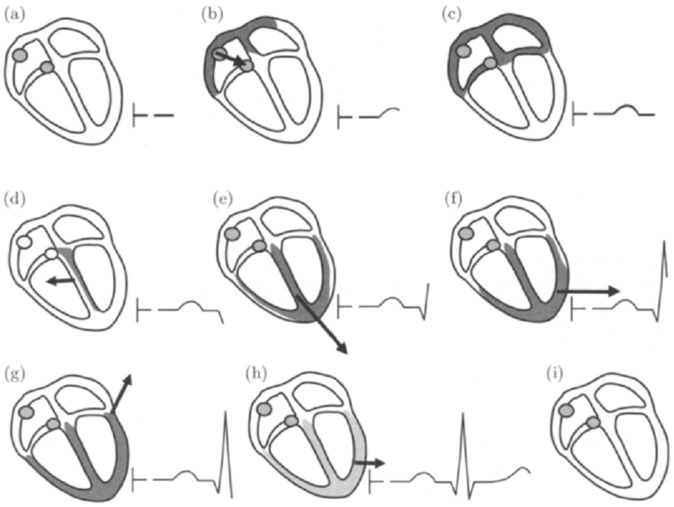

Figure 1.9: The ECG was recorded by an electrode placed at the area of symbol ⊢. (a) All cardiac cells at rest, (b) atrial depolarization, (c) the electrical impulse via the AV node, (d)-(g) ventricular depolarization, (h) ventricular repolarization, and (i) all cardiac cells once more at rest.[1]

- **Unipolar leads:** Measure voltage relative to a reference electrode (see figure 1.10).
- **Bipolar leads:** Measure the difference between two active electrodes

The standard 12-lead ECG system includes:

- Three bipolar limb leads (I, II, III)
- Three augmented unipolar limb leads (aVR, aVL, aVF)
- Six unipolar precordial leads (V1–V6)

Bipolar Leads (Einthoven's Triangle):

Measure potential differences:

- **Lead I:** Left Arm (VL) - Right Arm (VR): **I = VL - VR**
- **Lead II:**: Left Leg (VF) - Right Arm (VR): **II = VF - VR**
- **Lead III:** Left Leg (VF) - Left Arm (VL) :**III = VF - VL**

Augmented Unipolar Leads (Goldberger's Modification):

These examine frontal plane variations. Wilson [55] introduced them in 1934, refined

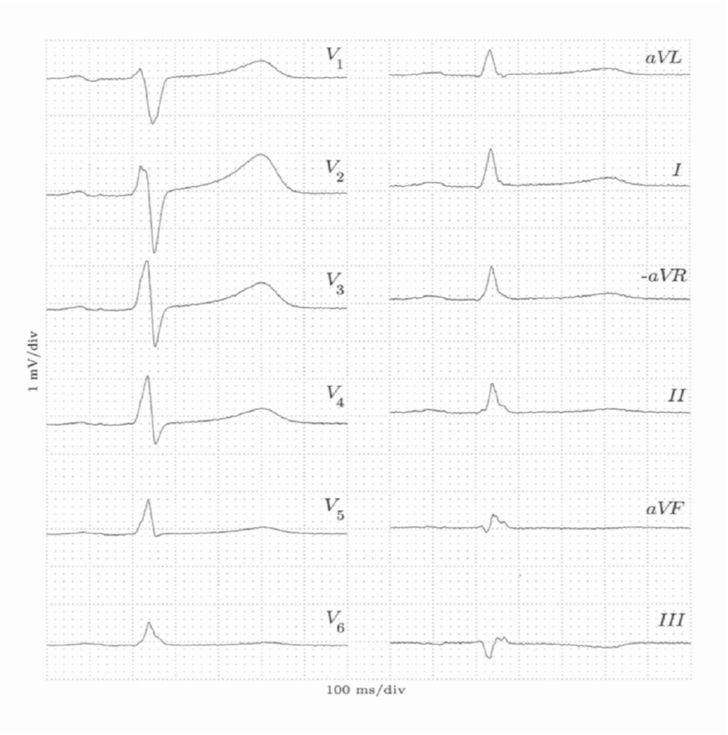

Figure 1.10: Illustration of the standard 12-lead ECG system. Bipolar leads (I, II, III), augmented unipolar leads (aVF, aVL, aVR), and chest leads (V1–V6).[3]

by Goldberger [56]. They provide higher amplitude readings

- **aVR** $= VR - \frac{VL+VF}{2}$
- **aVL** $= VL - \frac{VR+VF}{2}$
- **aVF** $= VF - \frac{VL+VR}{2}$

These six leads provide a comprehensive frontal view of the heart's electrical activity, aiding clinical and modeling analysis (see Figure 1.11)

Precordial Leads (V1–V6)

Six precordial leads (V1–V6) are unipolar chest leads examining electrical activity in the transverse plane (see Figure 1.11):

- **V1 and V2:** Placed on either side of the sternum at the 4th intercostal space, reflecting septal activity.
- **V3 and V4:** Positioned anteriorly, with V4 at the 5th intercostal space midclavicular, focusing on the anterior wall.

- **V5 and V6:** Along anterior and midaxillary lines at V4's horizontal level, highlighting lateral wall activity.

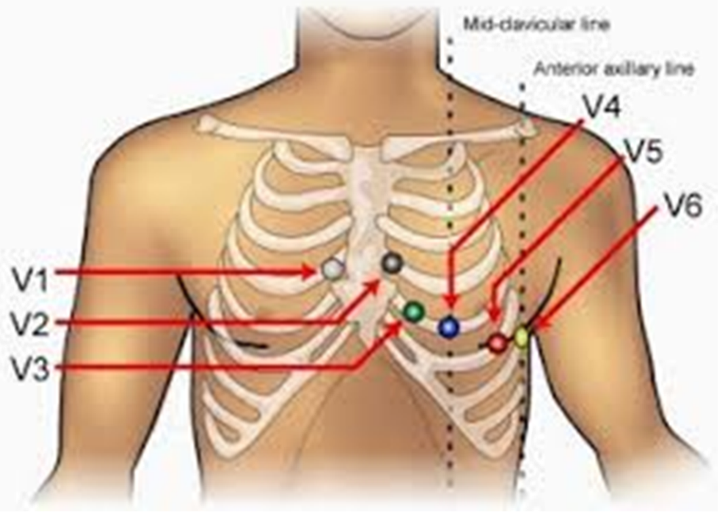

Figure 1.11: Illustration of the six precordial ECG leads (V1–V6) and their anatomical positions [4].

Together, these leads provide a three-dimensional heart view, improving diagnostic accuracy for ischemia, infarction, and hypertrophy.

1.3.2.1 ECG Waves and Time Intervals

The ECG waveform comprises characteristic deflections; abnormalities signify dysfunction. Figure 1.12 illustrates standard waveforms and intervals.

P wave :

Represents atrial depolarization from SA node to AV node. Duration ≈ 90 ms, may be positive or negative. Often subtle and challenging to detect in noisy signals.

QRS complex:

Reflects ventricular depolarization before contraction. It has the largest ECG amplitude, comprising:

- **Q wave** negative initial deflection
- **R wave** positive peak
- **S wave** negative deflection after R

Duration : 85-95 ms

T wave:

Represents ventricular repolarization, smaller than QRS. Typically positive but may vary. Occurs after the QRS returns to baseline.

U Wave (if visible):

May represent late Purkinje fiber repolarization.

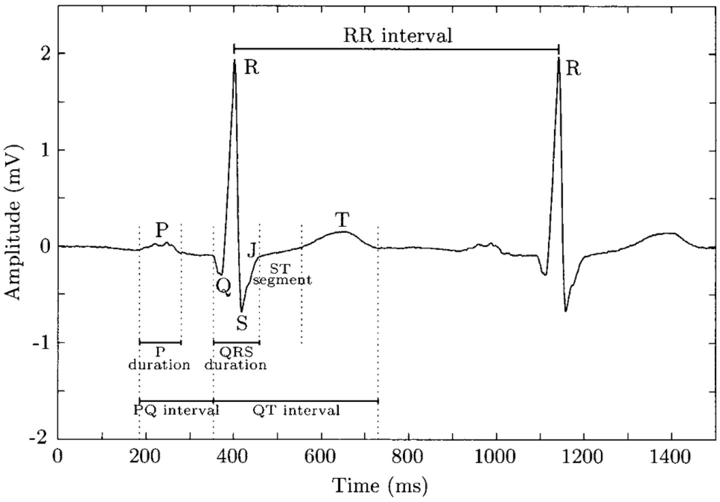

Figure 1.12: Cardiac cycle waves with durations and intervals. J-point marks QRS end and ST segment start [1].

Time Intervals: Key to Modeling

- **RR interval:** Time between two R waves, determines ventricular rate and heart rhythm.
- **PR Interval:** From P wave start to QRS start (0.12–0.20 sec). Prolongation suggests AV block.
- **QRS Duration:** Normal 0.08–0.10 sec; widening indicates bundle branch block or ventricular origin.
- **ST Segment:** Marks end of depolarization, start of repolarization. Elevation or depression signals ischemia.
- **QT Interval:** From QRS start to T wave end. Prolongation increases ventricular

arrhythmia risk.

1.3.3 Heart Rhythms and Arrhythmias

Normal sinus rhythm originates in the SA node with 50–100 bpm at rest. Any deviation defines arrhythmia, caused by:

- **Abnormal impulse formation:** Ectopic foci override SA node due to enhanced automaticity or SA failure.
- **Impulse conduction issues:** Partial/complete conduction blocks cause brady- or tachyarrhythmias.

Reentry Mechanism: Electrical impulses loop continuously due to conduction speed and refractory period variations, causing many atrial and ventricular arrhythmias.

Arrhythmia Classification:

- **Synchronized rhythms:** Atrial and ventricular activity aligned.
- **Faster atrial rate:** Suggests atrial origin.
- **Faster ventricular rate:** Suggests ventricular origin.
- **Independent rhythms:** One chamber dominates.

Arrhythmias may be:

- **Paroxysmal:** Sudden onset/termination
- **Persistent/permanent:** Continuous

1.3.3.1 Sinus Rhythm and Heart Rate Variability (HRV)

Sinus rhythm originates from the sinoatrial (SA) node, maintaining a heart rate of 50–100 beats per minute at rest(see Figure 1.13(a)).Deviations define:

- **Sinus bradycardia:** <50 bpm
- **Sinus tachycardia:** >100 bpm

Although heart rate is generally regular, minor variations occur due to autonomic nervous system influence—parasympathetic slows, sympathetic accelerates.

Heart Rate Variability (HRV) provides insights into autonomic control and cardiovascular health. Reduced HRV correlates with higher post-myocardial infarction mortality, reflecting increased arrhythmic risk [57, 58].

Respiratory sinus arrhythmia influences HRV—heart rate rises during inhalation, falls during exhalation (see Figure 1.13(b))). HRV is assessed using deep breathing, orthostatic, and Valsalva maneuvers [59].

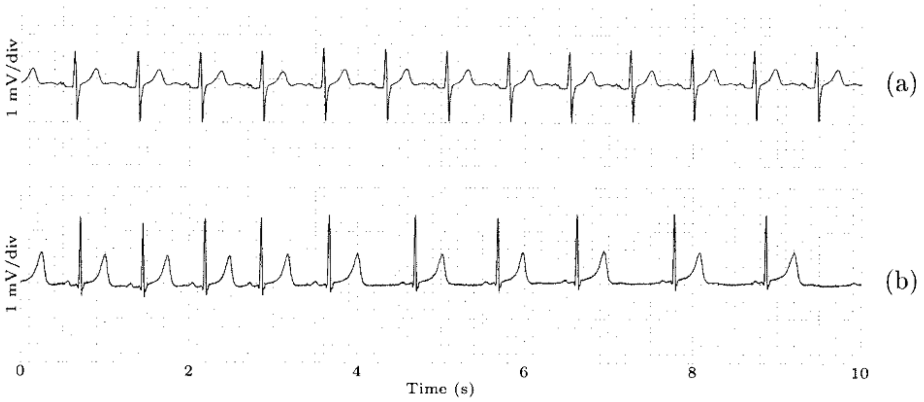

Figure 1.13: (a) Normal sinus rhythm (b) respiratory sinus arrhythmia.[1]

1.3.3.2 Premature Beats and Ectopic Activity

Occasionally, premature beats interrupt sinus rhythm before the expected discharge. Originating from atrial or ventricular ectopic foci, they are classified as:

- **Supraventricular premature beats (SVPBs):** Arise from atria or AV node, **showing altered P wave morphology** (see Figure 1.14(a)).
- **Ventricular premature beats (VPBs):** Originate below the AV node, producing **wide and bizarre QRS complexes** (see Figure 1.14(b)).

VPBs may cause a compensatory pause before normal rhythm resumes. Patterns include:

- **Bigeminy:** Every second beat ectopic
- **Trigeminy:** Every third beat ectopic (see Figure 1.14(c)-(d))

Frequent ectopic beats may signal underlying cardiac pathology.

Figure 1.14: ((a) SVPB with a small negative P wave after the third sinus beat.
(b) VPB followed by compensatory pause. RR interval sum equals twice normal RR.
(c) Bigeminy
(d) Trigeminy
(e) Interpolated VPB[1]

1.3.3.3 Atrial Arrhythmias: Flutter and Fibrillation

Atrial arrhythmias stem from enhanced automaticity or reentrant circuits within the atria.

- **Atrial tachycardia**: Characterized by a heart rate of 140–220 bpm, often with hidden P waves due to overlap with T waves.
- **Atrial flutter**: A more organized reentrant rhythm, usually around 300 bpm, where flutter waves (F waves) resemble a sawtooth pattern in the ECG (see Figure 1.15(a)).
- **Atrial fibrillation**: A chaotic, high-rate arrhythmia (400–700 bpm) with irregular ventricular responses and a lack of distinct P waves (see Figure 1.15(b)). It increases the risk of blood clots and strokes due to reduced atrial contraction.

1.3.3.4 Ventricular Arrhythmias and Life-Threatening Rhythms

Ventricular arrhythmias, primarily caused by reentry circuits, can lead to severe hemodynamic instability.

- Ventricular tachycardia: A rapid ventricular rhythm (>120 bpm) with vast QRS complexes. Sustained VT can compromise cardiac output and progress to more severe arrhythmias.
- Ventricular flutter: A rapid, organized rhythm with broad oscillations but no distinct QRS or T waves (Figure 1.15(c)).
- Ventricular fibrillation: A chaotic, disorganized rhythm where the ventricles quiver rather than contract, leading to cardiac arrest and immediate defibrillation (Figure 1.15(d)).

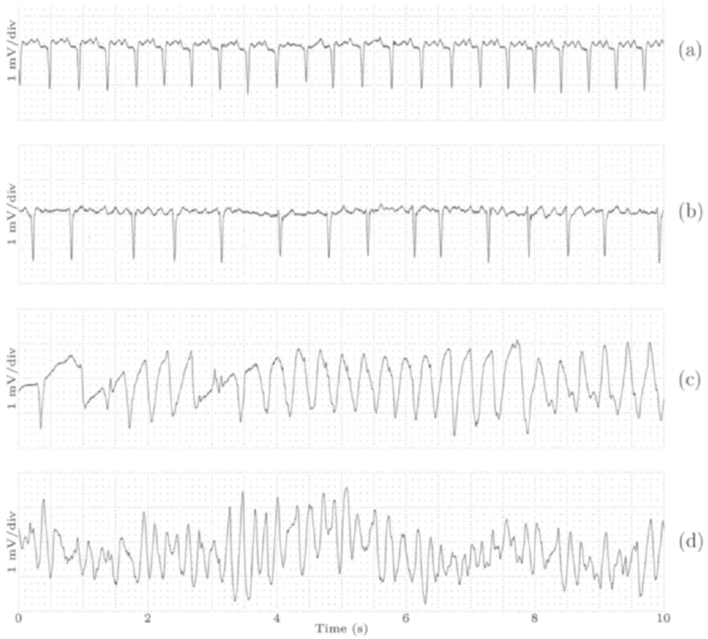

Figure 1.15: Illustrations of atrial and ventricular tachyarrhythmias. (a) Atrial flutter; (b) Atrial fibrillation; (c) Ventricular flutter; (d) Ventricular fibrillation.[1]

1.3.3.5 Conduction Blocks: Cataclysms in Electrical Pathways

Conduction blocks arise when the propagation of electrical impulses is delayed or blocked.

Atrioventricular (AV) blocks:

- First-degree: Delayed conduction (prolonged PR interval).
- Second-degree: Intermittent failure of impulse conduction.
- Third-degree (complete block): No conduction between atria and ventricles, leading to independent atrial and ventricular rhythms.

Bundle branch blocks: Occur in the right or left bundle branches, affecting ventricular depolarization and leading to prolonged QRS complexes.

1.4 Conclusion

This chapter has provided a comprehensive overview of non-stationary biomedical signals, with a particular emphasis on the ECG due to its central role in this study. We explored the physiological basis of bioelectrical signals, their acquisition methods, and their clinical significance, focusing on understanding the generation and recording of ECG signals. The characterization of normal and abnormal heart rhythms was also examined, highlighting the importance of accurate detection and interpretation in medical diagnostics.

A key challenge in biomedical signal analysis lies in the inherent non-stationarity of these signals, which manifests as dynamic variations, noise interference, and inter-individual differences. Addressing these challenges requires advanced signal processing techniques to enhance signal interpretation and improve diagnostic precision.

While various biomedical signals, including the EEG, EMG, and ENG, have been discussed, the primary focus of this chapter has remained on the ECG, given its relevance to the research presented in the following chapters. This chapter establishes a foundation for more advanced ECG modeling and analysis investigations, where sophisticated mathematical and computational techniques will address the complexities associated with non-stationary biomedical signals.

Chapter 2

Foundations of Fractional Calculus and Differential Equation Theory

2.1 Introduction

Fractional calculus, a mathematical field with origins spanning over three centuries, generalizes the classical notions of differentiation and integration to non-integer orders. Its roots trace back to the foundational work of luminaries like Leibniz, Newton, and Gauss, who laid the groundwork for modern calculus. This idea intrigued prominent mathematicians such as Euler, Lagrange, Laplace, Fourier, and Riemann, whose contributions shaped the early development of fractional calculus. The theory matured significantly throughout the 19th and 20th centuries, with figures like Liouville, Grunwald, Letnikov, and Heaviside advancing the field. Their work laid the foundation for contemporary fractional calculus, which has since transcended mathematics to become a versatile tool in engineering, physics, chemistry, and beyond. Applications range from modeling viscoelastic materials to analyzing diffusion processes, mechanical systems, and control theory. One of the most striking features of fractional calculus is its inherent non-locality: fractional derivatives and integrals depend not only on the behavior of a function at a single point but also on its values over an extended domain. This characteristic enables fractional calculus to capture complex, memory-dependent, and distributed phenomena, making it an elegant framework for describing the intricate dynamics of natural systems.

As science and engineering grapple with complex systems, fractional calculus has emerged as a powerful tool with significant implications for fields as diverse as fractal science, economics, and biology [60, 61]. This chapter elucidates significant terminology in fractional calculus and reiterates essential properties that will be employed in later sections. Fractional calculus generalizes classical calculus to encompass integrals and derivatives of non-integer order, providing a comprehensive framework for modeling intricate systems characterized by memory and hereditary attributes. For readers desiring a more thorough introduction, seminal texts such as those by Podlubny [62], Gorenflo and Mainardi [63], Kilbas et al. [64], and Das [60], as well as review articles [61, 65–76] , provide critical theoretical perspectives.

This chapter is primarily influenced by Diethelm's book [64], which offers a comprehensive analysis of fractional differential equations, and Garrappa's article [75], which investigates numerical solutions and computational methodologies for fractional models, accompanied by practical software tutorials.

Collectively, these references establish a solid basis for comprehending fractional calculus's theoretical and numerical methodologies.

2.2 Birth and Origins of Fractional Calculus

The concept of fractional calculus originated from the question: Can the notion of differentiation $\frac{d^n y}{dx^n}$, of integer order be extended to non-integer values of n? This inquiry, first posed in the 17th century by Leibniz and L'Hospital, laid the foundation for the generalization of classical calculus to arbitrary orders.

Subsequent contributions by Euler, Lagrange, Laplace, Lacroix, and Fourier further developed the theory. Euler investigated the algebraic meaning of non-integer order derivatives in 1730, while Lagrange formulated the law of exponents for differential operators:

$$\frac{d^m}{dx^m}.\frac{d^n}{dx^n}y = \frac{d^{m+n}}{dx^{m+n}}y. \tag{2.1}$$

This property later became a cornerstone for extending differentiation to fractional orders. In the 19th century, Laplace defined fractional derivatives via integrals, and Lacroix derived expressions generalizing derivatives for non-integer , linking the concept to what later became known as the Gamma function:

$$\frac{d^n y}{dx^n} = \frac{\Gamma(m+1)}{\Gamma(m-n+1)}x^{m-n}. \tag{2.2}$$

where $m > n$.

Fourier also contributed by introducing derivatives of arbitrary order in the context of integral transforms, showing early applications of fractional operations to harmonic analysis. Thus, although the early development of fractional calculus was largely theoretical, these foundational ideas paved the way for its modern applications in modeling complex, memory-dependent phenomena.

2.3 Generalization of Fractional Calculus

Let n be an integer. When we write x^n, it is naturally understood as x multiplied by itself n times. For example, although 2^π is mathematically valid, it is not straightforward to visualize. Similarly, the concept of a fractional derivative, while abstract, can be formally defined as follows:

$$\frac{d^\pi}{dx^\pi} f(x) \tag{2.3}$$

Although difficult to conceptualize intuitively, fractional derivatives are well-defined mathematical objects.

As real numbers exist between integers, fractional derivatives and integrals interpolate between traditional integer-order differentiation and n-fold integration. The subsequent generalizations observed are:

- For exponentiation:

$$\begin{aligned} x^n &= x \cdot x \cdot x \cdot \ldots \cdot x && \text{(for integer } n\text{)} \\ x^n &= e^{n \ln x} && \text{(for real } n\text{)} \end{aligned} \tag{2.4}$$

- For factorial:

$$\begin{aligned} n! &= 1 \cdot 2 \cdot 3 \cdot \ldots \cdot (n-1) \cdot n && \text{(for integer } n\text{)} \\ n! &= \Gamma(n+1) && \text{(for real } n\text{)} \end{aligned} \tag{2.5}$$

Where the Gamma function is defined as:

$$\Gamma(x) = \int_0^\infty t^{x-1} e^{-t}\, dt. \tag{2.6}$$

Figure 2.1 illustrates the number line extended for mapping fractional differintegrals, where:

- Negative values correspond to integration,
- Positive values correspond to differentiation.

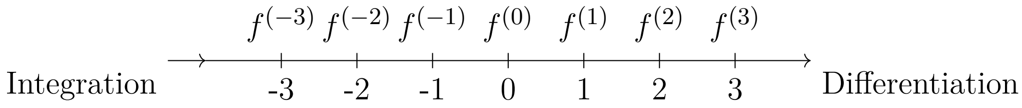

Figure 2.1: Number line representation and its extension to fractional differintegrals in fractional calculus.

Heaviside (1871) recognized that there exists a mathematical domain between complete differentiation and integration where fractional operators emerge and hold equal validity.[60]

We recognize terms such as natural numbers and real numbers. Although these terms are widely used, they are abstractions rather than true reflections of physical quantities.

Fractional calculus does not refer to the calculus of fractions, nor does it pertain to a fraction of any calculus involving differentiation, integration, or the calculus of variations. Rather, fractional calculus refers to the theory of integrations and derivatives of arbitrary (non-integer) order, unifying and generalizing the concept of classical integer-order calculus. Thus, fractional derivatives and integrals are referred to as generalized differences.

2.4 The origin of the Riemann-Liouville (RL) definition

The initial study that eventually led to the Riemann-Liouville definition was N. Ya. Sonin's paper from 1869, titled On Differentiation with Arbitrary Index. Sonin's work referenced Cauchy's integral formula as a starting point.

Between 1868 and 1872, A. V. Letnikov expanded on Sonin's ideas, notably in his publication An Explanation of the Main Concepts of the Theory of Differentiation of Arbitrary Index (1872). The n-th derivative via Cauchy's integral formula is given by:

$$D^n f(z) = \frac{n!}{2\pi i} \int_c \frac{f(\zeta)}{(\zeta - z)^{n+1}} .d\zeta \tag{2.7}$$

where n is an integer.

Generalizing n! to arbitrary values using $\nu = \Gamma(\nu + 1)$ is straightforward. However, when n is non-integer, the integrand no longer has a pole but a branch point, requiring branch cuts for contour integration.

In 1884, H. Laurent made a significant advancement by applying contour integration on Riemann surfaces, establishing a foundation for generalized operators. Laurent's method generalized Cauchy's integral formula into an open circuit contour, leading to the definition[61]:

$${}_c\mathrm{D}_x^{-\nu} f(x) = \frac{1}{\Gamma(\nu)} \int_c^x (x-t)^{\nu-1} f(t) dt, \quad Re\ \nu > 0. \tag{2.8}$$

When c=0 ((2.8)) simplifies to the most common form:

$${}_0\mathrm{D}_x^{-\nu} f(x) = \frac{1}{\Gamma(\nu)} \int_0^x (x-t)^{\nu-1} f(t) dt, \quad Re\ \nu > 0. \tag{2.9}$$

This expression is now known as the Riemann-Liouville fractional integral. A necessary condition for the convergence of ((2.9)) is that

$$f(x) = O(x^{1-\epsilon}), \quad \epsilon > 0. \tag{2.10}$$

or equivalenty :

$$f(x) = O(x^{a}), \quad a > -1. \tag{2.11}$$

When c is negative infinity, (2.8) becomes

$${}_{-\infty}\mathrm{D}_x^{-\nu} f(x) = \frac{1}{\Gamma(\nu)} \int_{-\infty}^x (x-t)^{\nu-1} f(t) dt, \quad Re\ \nu > 0. \tag{2.12}$$

A sufficient condition that (2.12) converge is that

$$f(-x) = O(x^{-\nu-\epsilon}), \quad \epsilon > 0, \quad x \to \infty \tag{2.13}$$

Functions possessing this condition are called Liouville class functions.

For example, $f(x) = x^{-a}, \quad a > \nu > 0$ belongs to this class.

Examples :

For $f(x) = e^{az}$ with $a > 0$, from (2.12) :

$$_{-\infty}\mathrm{D}_x^{-\nu} e^{ax} = a^{-\nu} e^{ax} \tag{2.14}$$

Assuming the rule of exponents $D[D^{-\nu} f(x)] = D^{1-\nu} f(x)$, for $0 < \nu < 1$, so $\mu = 1 - \nu > 0$, yields:

$$_{-\infty}\mathrm{D}_x^{\mu} e^{ax} = a^{\mu} e^{ax}, \quad Re \quad a > 0 \tag{2.15}$$

If $f(x) = x^{-a}$, with $a > \nu > 0$, then

$$_{-\infty}\mathrm{D}_x^{-\nu} x^{-a} = (-1)^{-\nu} \frac{\Gamma(a-\nu)}{\Gamma(a)} x^{-a+\nu} \tag{2.16}$$

and for x < 0 ,and if 0 < ν < 1,then $\mu = 1 - \nu > 0$ and

$$_{-\infty}\mathrm{D}_x^{\mu} x^{-a} = (-1)^{\mu} \frac{\Gamma(a+\mu)}{\Gamma(a)} x^{-a-\mu} \tag{2.17}$$

Similarly, For $f(x) = x^a$ and $\nu > 0$:

$$_{0}\mathrm{D}_x^{-\nu} x^{a} = \frac{\Gamma(a+1)}{\Gamma(a+\nu+1)} x^{a+\nu}, \quad a > -1. \tag{2.18}$$

and appmying the operator rule :

$$
{}_0\mathrm{D}_x^{\nu} x^a = \frac{\Gamma(a+1)}{\Gamma(a-\nu+1)} x^{a-\nu}, \quad a > -1. \tag{2.19}
$$

Special Case : If $f(x) = 1$ and $\nu = \frac{1}{2}$, then (2.19) :

$$
{}_0\mathrm{D}_x^{1/2}(1) = \frac{1}{\sqrt{\pi x}}, \tag{2.20}
$$

showing that the fractional derivative of a constant is non-zero.

2.5 Fractional Derivatives

The notation for fractional derivatives has evolved over time and remains partially non-standardized [65, 72]. Leibniz and Euler used d^α; Riemann wrote Θ_x^α; Liouville preferred $\frac{d^\alpha}{dx^\alpha}$. Grünwald used $\left\{\frac{d^\alpha f}{dx^\alpha}\right\}_{x=a}$ or $D^\alpha[f]_{x=a}$; Marchaud used $D^\alpha[f]_{(\alpha)}$; and Hardy–Littlewood wrote f^α. Modern authors also employ notations such as $I^{-\alpha}$, $I_x^{-\alpha}$, ${}_a\mathrm{D}_x^\alpha$, $\frac{d^\alpha}{dx^\alpha}$, and occasionally $\frac{d^\alpha}{d(x-\alpha)^\alpha}$ instead of D_{a+}^α.

Fractional derivatives are defined through integrals, making them non-local operators. The time-fractional derivative reflects past states of the system, exhibiting a memory effect. Due to this non-locality, they are useful in developing generalized models and governing principles. They have important applications in astrophysics, economics, fusion plasmas, mechanics, and viscoelasticity. [73]

We now restate a foundational definition. For further reading, see [61, 62, 74]

2.5.1 RL Fractional Derivative

Definition 1 *Let* $-\infty \le a \le x \le b \le \infty$*. The Riemann–Liouville fractional integral of order* $\alpha > 0$*, with lower limit* a *(or upper limit* b*), is defined for functions satisfying* $f \in L^1([a,b])$ *and* $f * K^{n-\alpha} \in W^{n,1}([a,b])$ *as follows:*

$$
(D_{a\pm}^\alpha f)(x) = (\pm 1)^n \frac{d^n}{dx^n} (I_{a\pm}^{n-\alpha} f)(x), \tag{2.21}
$$

and $(D_{a\pm}^\alpha f)(x) = f(x) \quad for \quad \alpha = 0.$

Here, $n = [\alpha] + 1$ is the smallest integer greater than α, and

$W^{k,p}(G) = \{f \in L^p(G) : f^{(kp)} \in L^p(G)\}$

denotes a Sobolev space. For $k = p = 1$, we have $W^{1,1}([a,b]) = AC^0([a,b])$,the space of absolutely continuous functions.

2.5.2 Caputo Fractional Derivative

Let $f(x)$ be uniformly continuous on the closed interval $[a,b]$. Then its first derivative f' exists almost everywhere on $[a,b]$ and satisfies $f' \in L^1([a,b])$. In this case, the function f can be represented as:

$$f(x) = \int_a^x f'(y)dy + f(a) = (\mathrm{I}^1_{a+} f')(x) + f(a), \tag{2.22}$$

Substituting this into the fractional integral operator I^α_{a+} gives :

$$(\mathrm{I}^\alpha_{a+} f)(x) = (\mathrm{I}^1_{a+}\mathrm{I}^\alpha_{a+} f')(x) + \frac{f(a)}{\Gamma(\alpha+1)}(x-a)^\alpha, \tag{2.23}$$

Using the commutativity of fractional integrals, we derive:

$$(\mathrm{D}\mathrm{I}^\alpha_{a+} f)(x) = (\mathrm{I}^\alpha_{a+} f')(x) + \frac{f(a)}{\Gamma(\alpha)}(x-a)^{\alpha-1}, \tag{2.24}$$

For $0 < \alpha < 1$, we define $(Df)(x) = \frac{df(x)}{dx} = f'(x)$, which denotes the first-order derivative.

This motivates the definition of the Caputo fractional derivative as a modified form of the Riemann–Liouville derivative:

$$({}^c\mathrm{D}^\alpha_{a+} f)(x) := \mathrm{I}^{n-\alpha}_{a+} f^{(n)} = \frac{1}{\Gamma(n-\alpha)} \int_a^x \frac{f^{(n)}(y)}{(x-y)^{\alpha-n+1}} dy, \tag{2.25}$$

where $n = [\alpha] + 1$. The function f must be at least n-times differentiable.

Although the expression was introduced by Liouville, it is now commonly attributed to Caputo. Henceforth, we denote the Caputo derivative of order α by $\frac{d^\alpha}{dx^\alpha}$ instead of ${}^C\mathrm{D}^\alpha_{0+}$. When the function maps into a Banach space X, the integrals and derivatives are taken in the Bochner sense.

2.5.3 Basic Properties of RL and Caputo Fractional Derivatives

Let λ, μ, α, a be constants, and let f, g be functions for which the involved operations are defined. The fractional derivatives satisfy linearity:

$$\mathrm{D}^\alpha_{a\pm}(\lambda f + \mu g) = \lambda \mathrm{D}^\alpha_{a\pm}(f) + \mu \mathrm{D}^\alpha_{a\pm}(g), \tag{2.26}$$

$${}^c\mathrm{D}^\alpha_{a\pm}(\lambda f + \mu g) = \lambda {}^c\mathrm{D}^\alpha_{a\pm}(f) + \mu {}^c\mathrm{D}^\alpha_{a\pm}(g), \tag{2.27}$$

If a function f is expressed as a uniformly convergent infinite series, the derivative distributes over the sum:

$$\left(\mathrm{D}^\alpha_{a\pm} \sum_{k=0}^{\infty} f_k\right)(x) = \sum_{k=0}^{\infty} (\mathrm{D}^\alpha_{a\pm} f_k)(x) \tag{2.28}$$

$$\left({}^c\mathrm{D}^\alpha_{a\pm} \sum_{k=0}^{\infty} f_k\right)(x) = \sum_{k=0}^{\infty} ({}^c\mathrm{D}^\alpha_{a\pm} f_k)(x) \tag{2.29}$$

Particularly for a finite lower bound, we must focus solely on the uniform convergence associated with derivatives, as integrals remain uniformly convergent by default.

The Caputo operator is commutative with respect to composition:

$$({}_0^C\mathrm{D}^{\alpha C}_{x_0}\mathrm{D}^\beta_x f)(x) = ({}_0^C\mathrm{D}^{\beta C}_{t_0}\mathrm{D}^\alpha_x f)(x) = (({}_0^C\mathrm{D}^{\alpha+\beta}_x f)(x), \quad \forall \alpha, \beta \in \mathbb{R}_+, \tag{2.30}$$

$${}_0^C\mathrm{D}^\alpha_x c = 0 \quad for \quad any \quad constant \quad c.$$

In contrast, the Riemann–Liouville derivative of a constant is generally non-zero:

$$
{}_0\mathrm{D}_x^{\alpha} c = \frac{c x^{-\alpha}}{\Gamma(\alpha - 1)} \tag{2.31}
$$

The relationship between the Riemann–Liouville and Caputo derivatives is given by:

$$
(\mathrm{D}_{a+}^{\alpha} f)(x) = ({}^{C}\mathrm{D}_{a+}^{\alpha} f)(x) + \sum_{k=0}^{n-1} \frac{(x-\alpha)^{k-a}}{\Gamma(k-\alpha+1)} f^{(k)}(a), \quad \alpha \geq 0. \tag{2.32}
$$

This illustrates that the Riemann–Liouville and Caputo operators differ by terms dependent on initial conditions.

The Riemann–Liouville integral and differential operators are mutual inverses under appropriate conditions:

$$
(D_{a+}^{\alpha} I_{a+}^{\alpha} f(x) = f(x); \tag{2.33}
$$

$$
I_{a+}^{\alpha} D_{a+}^{\alpha} f(x) = f(x) - \sum_{k=0}^{n-1} \frac{(x-\alpha)^{\alpha-k-1}}{\Gamma(\alpha-k)} (D^{n-k-1} I_{a+}^{n-\alpha} f)(a), \tag{2.34}
$$

where $\mathrm{I}_{a+}^{n-\alpha} f \in AC^m([a,b]) := \left\{ f \in C^m([a,b]) | f^{(n)} \quad is \quad absolutely \quad continuous \right\}$

$f \in L^1([a,b]), \alpha > 0 \quad and \quad n = [\alpha] + 1.$

2.5.4 The Generalized RL Fractional Derivative

The generalized Riemann–Liouville fractional derivative of order $0 < \alpha < 1$ and type $0 \leq \beta \leq 1$ with lower (respectively upper) limit a is defined as :

$$
\left(D_{a\pm}^{\alpha,\beta} f \right)(x) = \left(\pm I_{a\pm}^{\beta(1-\alpha)} \frac{d}{dx} \left(I_{a\pm}^{(1-\beta)(1-\alpha)} f \right) \right)(x), \tag{2.35}
$$

The function f must be such that the right-hand side is well-defined.

Special cases:

- $D_{a\pm}^{\alpha} = D_{a\pm}^{\alpha,0}$ (Riemann–Liouville derivative)

- ${}^{C}\mathrm{D}^{\alpha}_{a\pm} = D^{\alpha,1}_{a\pm}$. (Caputo derivative)

The type parameter β enables a continuous transition between the two classical derivatives.

2.6 Relations Between RL Integrals and Derivatives

After introducing the Riemann–Liouville integral and derivative operators separately, we now examine their interrelationship.

Under certain conditions, the RL derivative acts as the left inverse of the RL integral. This leads to the following result:

Let $n > 0$. If there exists some $\phi \in L_1[a,b]$ such that $f = I^n_a \phi$, then

$$I^n_a D^n_a f = f \tag{2.36}$$

almost everywhere.

Proof. This follows directly:

$$I^n_a D^n_a f = I^n_a [D^n_a I^n_a \phi] = I^n_a \phi = f \tag{2.37}$$

If f does not meet the criteria above, the composition $I^n_a D^n_a f$ can still be expressed explicitly as follows.

Let $n > 0$ and $m = \lfloor n \rfloor + 1$. Assume that f is such that $I^{m-n}_a f \in A^m[a,b]$. Then,

$$I^n_a D^n_a f(x) = f(x) - \sum_{k=0}^{m-1} \frac{(x-a)^{n-k-1}}{\Gamma(n-k)} \lim_{z \to a+} I^{m-n}_a f(z). \tag{2.38}$$

Specifically, for 0 < n < 1 we obtain :

$$I^n_a D^n_a f(x) = f(x) - \frac{(x-a)^{n-1}}{\Gamma(n)} \lim_{z \to a+} I^{1-n}_a f(z) \tag{2.39}$$

Proof. Assume that $D^{m-1}J_a^{m-n}f$ exists and is continuous. Then, there exists a function $\phi \in L^1$ such that

$$D^{m-1}J_a^{m-n}f = D^{m-1}J_a^{m-n}f(a) + J_a^1\phi.$$

From this we get:

$$I_a^{m-n}f(x) = -\sum_{k=0}^{m-1}\frac{(x-a)^k}{k!}\lim_{z\to a+} I_a^{m-n}f(z) + I_a^m\phi(x). \tag{2.40}$$

Now, substitute into:

$$I_a^nD_a^nf(x) = I_a^nD_a^mI_a^{m-n}f(x), \tag{2.41}$$

Since:

$$D^m\left[\sum_{k=0}^{m-1}\frac{(x-a)^k}{k!}\lim_{z\to a+} D^kI_a^{m-n}f(z)\right] = 0, \tag{2.42}$$

It follows:

$$I_a^nD_a^nf(x) = I_a^nD^mI_a^m\phi(x) = I_a^n\phi(x) \tag{2.43}$$

Then rewrite f(x) as :

$$f(x) = \sum_{k=0}^{m-1}\frac{(x-a)^{k+n-m}}{\Gamma(k+n-m+1)}\lim_{z\to a+} D^kI_a^{m-n}f(z) + I_a^m\phi(x). \tag{2.44}$$

Finally, substitute and isolate to get:

$$I_a^nD_a^nf(x) = f(x) - \sum_{k=0}^{m-1}\frac{(x-a)^{n-k-1}}{\Gamma(n-k)}\lim_{z\to a+} D^{m-k-1}I_a^{m-n}f(x). \tag{2.45}$$

2.7 Taylor and Fractional Taylor Expansion

A fundamental result in classical analysis is Taylor's theorem. It can be expressed in a more insightful form than is often found in standard texts, as it reveals structural information about the function space A^m .

The classical version of this theorem follows by setting y=a in the general form below.

The following statements are equivalent:

Theorem 1 (Taylor Expansion) *The following statements are equivalent:*

1. $f \in A^m[a,b]$,
2. *For every* $x, y \in [a,b]$, *the following identity holds:*

$$f(x) = \sum_{k=0}^{m-1} \frac{(x-y)^k}{k!} D^k f(y) + I_y^m D^m f(x), \tag{2.46}$$

where

$$I_y^m D^m f(x) = f(x) - T_{m-1}[f;y](x). \tag{2.47}$$

Here, $T_{m-1}\left[f;a\right](x)$ denotes the Taylor polynomial of degree m-1 centered at y:

$$T_{m-1}\left[f;a\right](x) = \sum_{k=0}^{m-1} \frac{(x-y)^k}{k!} D^k f(y) \tag{2.48}$$

A fractional generalization of Taylor's theorem can be formulated using the previous results. Under the assumptions of Theorem 1, we have:

Theorem 2 ***(Fractional Taylor expansion)****. Under the assumptions of Theorem (1), we have*

$$f(x) = \frac{(x-a)^{n-m}}{\Gamma(n-m+1)} \lim_{z \to a+} I_a^{m-n} f(z) + \sum_{k=1}^{m-1} \frac{(x-a)^{k+n-m}}{\Gamma(k+n-m+1)} \lim_{z \to a+} D_a^{k+n-m} f(z) + I_a^n D_a^n f(x) \tag{2.49}$$

Note that when $n \in \mathbb{N}$, $m = n+1$, the first limit term vanishes, and the classical Taylor expansion is recovered.

Proof Sketch. From the previous results, we have:

$$f(x) = \sum_{k=0}^{m-1} \frac{(x-a)^{k+n-m}}{\Gamma(k+n-m+1)} \lim_{z \to a^+} D^k I_a^{m-n} f(z) + I_a^n D_a^n f(x). \tag{2.50}$$

Rewriting the sum by substituting $k \to m-k-1$, and rearranging terms, yields the desired expression.

2.8 GL Fractional Derivatives

The GL approach generalizes classical finite differences to non-integer orders.

Definition 2 *The GL fractional derivative of order* $\alpha > 0$ *with a lower bound* a *is defined as*

$${}^{GL}\mathrm{D}_{a+}^{\alpha}(f)(x) = \lim_{h \to 0^+} \frac{1}{h^\alpha} \sum_{k=0} [(x-a)/h](-1)^k \binom{\alpha}{k} f(x-kh) \tag{2.51}$$

The GL fractional derivative of order α with upper limit b is defined as the limit.

$$({}^{GL}\mathrm{D}_{b-}^{\alpha}(f)(x) = \lim_{h \to 0^+} \frac{1}{h^\alpha} \sum_{k=0}^{[(b-x)/h]} (-1)^k \binom{\alpha}{k} f(x+kh) \tag{2.52}$$

Here, $\binom{\alpha}{k}$ denotes the generalized binomial coefficient:

$$\binom{\alpha}{k} = \frac{\Gamma(\alpha+1)}{\Gamma(k+1)\Gamma(\alpha-k+1)} \tag{2.53}$$

2.8.1 GL Approach

The GL method is a fundamental tool in the numerical treatment of fractional derivatives, as it is based directly on the definition of the derivative as a limit of fractional differences.

Let h be the time step, and define the backward difference operator as:

$$\nabla_h^n f(t) = \sum_{k=0}^{\left\lfloor \frac{t}{h} \right\rfloor} (-1)^k \binom{n}{k} f(t-kh) \tag{2.54}$$

Then the GL approximation of the left-sided derivative of order α is:

$$D_t^\alpha f(t) \approx \frac{1}{h^\alpha} \sum_{k=0}^{n} (-1)^k \binom{\alpha}{k} f(t-kh) \tag{2.55}$$

This method results in a convolution-type sum, incorporating the entire past of the solution at each time step. However, it can become computationally expensive for long simulations due to the accumulation of terms.

To alleviate this, algorithms such as short-memory principle and fast convolution are introduced in practice.

2.9 Numerical Techniques for Resolving Fractional Differential Equations (FDEs)

One of the most critical applications of Caputo's derivative lies in solving FDEss. Unlike FDEs involving the RL derivative—which require initial conditions expressed as fractional-order derivatives—an initial value problem for an FDE (or a system of FDEs) involving the Caputo derivative of order $\alpha > 0$ (with $m-1 < \alpha \leq m$) can be formulated as follows [75, 76]:

$$\begin{cases} D_{t_0}^\alpha y(t) = f(t, y(t)), \\ y(t_0) = y_0, \quad y'(t_0) = y_0^{(1)}, \quad \ldots, \quad y^{(m-1)}(t_0) = y_0^{(m-1)}. \end{cases} \tag{2.56}$$

where $f(t,y)$ is presumed to be continuous and $y_0, y_0^{(1)}, \ldots, y_0^{(m-1)}$ are the specified values of the derivatives at t_0. Initializing the FDE with designated values of integer-order derivatives is more advantageous due to their explicit physical significance in relation to fractional-order derivatives.

The application of the RL integral $J_{t_0}^a$ to both sides of Equation (2.56), in conjunction with Theorem 1, results in the reformulation of the FDE as a weakly-singular Volterra integral equation (VIE):

$$y(t) = T_{m-1}[y;t_0](t) + \frac{1}{\Gamma(a)} \int_{t_0}^{t} (t-t_0)^{a-1} f(t,y(t))\, dt. \tag{2.57}$$

The integral formulation (2.57) is undoubtedly advantageous as it enables the utilization of existing theoretical and numerical results for this category of Volterra Integral Equations (VIEs) to analyze and resolve Fractional Differential Equations (FDEs). We emphasize the nonlocal characteristic of FDEs: the existence of absolute power in the kernel precludes the decomposition of the solution of Equation (2.57) at any point t_n into the solution at a prior point $t_n - h$ plus an increment term associated with the interval $[t_n - h, t_n]$, as is typical with IDEs. Moreover, as demonstrated by Lubich [77] [9], the solution of the VIE (2.57) exhibits an expansion in mixed (i.e., integer and fractional) powers:

$$y(t) = T_{m-1}(t) + \sum_{i,j \in \mathbb{N}} (t-t_0)^{i+j}\, a_{i,j} \tag{2.58}$$

This indicates a lack of smoothness at t_0; as is widely recognized, the absence of smoothness at $t = t_0$ presents challenges for numerical calculation, as approaches reliant on polynomial approximations are ineffective in yielding precise answers when smoothness is compromised.

FDEs are widely used to model complex systems in science and engineering due to their ability to capture memory and hereditary effects. However, solving FDEs poses unique challenges because of their nonlocal nature and the fractional-order derivatives involved. Several numerical methods have been developed to address these challenges, broadly categorized into two prominent families[78]:

- **Approximation of derivatives** [76]
  - GL scheme for derivatives

  - L1 and L2 algorithms

- **Methods based on integral formulation**[76]
  - GL scheme for integrals
  - Product-integration rules
  - Fractional Linear Multistep Methods

2.9.1 GL Scheme for Derivatives

The general fractional differential equation is expressed as:

$$^{C}\mathrm{D}_{t_0}^{\alpha} y(t) = f(t, y(t)), \tag{2.59}$$

where $^{C}\mathrm{D}_{t_0}^{\alpha}$ represents the Caputo fractional derivative.

The GL derivative is defined as:

$$^{GL}\mathrm{D}_{t_0}^{\alpha}(y)(t) = \lim_{h \to 0} \frac{1}{h^{\alpha}} \sum_{k=0}^{N} (-1)^k \begin{pmatrix} \alpha \\ k \end{pmatrix} y(t - kh), \tag{2.60}$$

with

$$\begin{pmatrix} \alpha \\ k \end{pmatrix} = \frac{\Gamma(\alpha+1)}{k!\,\Gamma(\alpha-k+1)}. \tag{2.61}$$

The relationship between the Caputo and GL derivatives is given by:

$$^{C}\mathrm{D}_{t_0}^{\alpha}(y)(t) =^{GL} \mathrm{D}_{t_0}^{\alpha}[y(t) - y_0], \quad 0 < \alpha \leq 1. \tag{2.62}$$

To numerically implement the GL derivative for a fixed step size $h > 0$, we use:

$$\frac{1}{h^{\alpha}}\sum_{k=0}^{n}(-1)^{k}\begin{pmatrix}\alpha\\k\end{pmatrix}[y_{n-k}-y_{0}]=f(t_{n},y_{n}),\quad 0<\alpha\leq 1. \tag{2.63}$$

The GL scheme is thus formulated as:

$$\sum_{k=0}^{n}(-1)^{k}\begin{pmatrix}\alpha\\k\end{pmatrix}[y_{n-k}-y_{0}]=h^{\alpha}f(t_{n},y_{n}),\quad 0<\alpha\leq 1. \tag{2.64}$$

Properties The GL scheme

- Order of Convergence: The scheme has a first-order convergence, expressed as:

$$y(t_{n})-y_{n}=\mathcal{O}(h). \tag{2.65}$$

- Special case for $\alpha=1$: When $\alpha=1$, the coefficients simplify as:

$$(-1)^{k}\begin{pmatrix}\alpha\\k\end{pmatrix}=(-1)^{k}\frac{\Gamma(\alpha+1)}{k!\Gamma(k-\alpha+1)}=\begin{cases}1, & k=0,\\ -1, & k=1,\\ 0, & k>1.\end{cases} \tag{2.66}$$

In this case, the scheme reduces to the standard backward Euler method for IDE:

$$y_{n}=y_{n-1}+hf(t_{n},y_{n}). \tag{2.67}$$

- General Formulation of the GL Scheme

The general scheme is:

$$\sum_{k=0}^{n}w_{k}^{\alpha}[y_{n-k}-y_{0}]=h^{\alpha}f(t_{n},y_{n}), \tag{2.68}$$

with weights defined as:

$$w_k^{\alpha} = (-1)^k \begin{pmatrix} \alpha \\ k \end{pmatrix}, \quad 0 < \alpha \leq 1. \tag{2.69}$$

- Reformulation of the Scheme

  The scheme can also be reformulated as:

$$\begin{aligned} \sum_{k=0}^{n} w_k^{\alpha} &= w_n^{\alpha-1}, \\ \sum_{k=0}^{n} w_k^{\alpha} y_k &= w_n^{\alpha-1} y_0 + h^{\alpha} f(t_n, y_n). \end{aligned} \tag{2.70}$$

- For the RL derivative , no initial term is required because:

$$^{RL}\mathrm{D}_{t_0}^{\alpha} y(t) =^{GL} \mathrm{D}_{t_0}^{\alpha} y(t). \tag{2.71}$$

- For $\alpha > 1$, the term y_0 is replaced by the Taylor expansion of order $m-1$:

$$T_{m-1}(t_n) = \sum_{j=0}^{m-1} \frac{(t_n - t_0)^j}{j!} y^{(j)}(t_0). \tag{2.72}$$

2.9.2 L1 and L2 Algorithms

- **L1 Algorithm** $(0 < \alpha \leq 1)$

Starting from the definition of Caputo's derivative for $0 < \alpha \leq 1$, we have:

$$^{C}\mathrm{D}_{t_0}^{\alpha} y(t) = \frac{1}{\Gamma(1-\alpha)} \int_{t_0}^{t} (t-\tau)^{-\alpha} y'(\tau) d\tau \tag{2.73}$$

- On a grid $t_n = t_0 + nh$, the integral can be written piecewise as:

$$^{C}\mathrm{D}_{t_0}^{\alpha} y(t_n) = \frac{1}{\Gamma(1-\alpha)} \sum_{j=0}^{n-1} \int_{t_j}^{t_{j+1}} (t_n - \tau)^{-\alpha} y'(\tau) d\tau \tag{2.74}$$

- On each interval $[t_j, t_{j+1}]$, approximate $y'(\tau)$ as:

$$y'(\tau) = \frac{y(t_{j+1}) - y(t_j)}{h} + \mathcal{O}(h) \quad \text{as } h \to 0 \tag{2.75}$$

- Substitute this approximation into the integrals and evaluate exactly:

$${}^{C}\mathrm{D}^{\alpha}_{t_0} y(t_n) \approx \frac{1}{\Gamma(1-\alpha)} \sum_{j=0}^{n-1} \int_{t_j}^{t_{j+1}} (t_n - \tau)^{-\alpha} \left[\frac{y(t_{j+1}) - y(t_j)}{h} \right] d\tau \tag{2.76}$$

The approximated derivative becomes:

$${}^{C}\mathrm{D}^{\alpha}_{t_0} y(t_n) \approx \frac{1}{\Gamma(1-\alpha)} \sum_{j=0}^{n-1} \left[\frac{y(t_{j+1}) - y(t_j)}{h} \right] \int_{t_j}^{t_{j+1}} (t_n - \tau)^{-\alpha} d\tau \tag{2.77}$$

The standard integral evaluation is:

$$\int_{t_j}^{t_{j+1}} (t_n - \tau)^{-\alpha} d\tau = h^{1-\alpha} \frac{(n-j)^{1-\alpha} - (n-j-1)^{1-\alpha}}{1-\alpha} \tag{2.78}$$

Thus, the approximated operator becomes:

$${}^{L1}\mathrm{D}^{\alpha}_{t_0} y(t_n) = \frac{1}{\Gamma(1-\alpha)} \sum_{j=0}^{n-1} h^{1-\alpha} \frac{(n-j)^{1-\alpha} - (n-j-1)^{1-\alpha}}{1-\alpha} \cdot \frac{y(t_{j+1}) - y(t_j)}{h} \tag{2.79}$$

Simplifying:

$$\Gamma(1-\alpha) \cdot \Gamma(1-\alpha) = \Gamma(2-\alpha) \tag{2.80}$$

The L1 Approximation($0 < \alpha \leq 1$):

$${}^{L1}\mathrm{D}^{\alpha}_{t_0} y(t_n) = \frac{1}{\Gamma(1-\alpha)} \left[\overline{w}_{n,0} y(t_0) + \sum_{j=1}^{n} w_{n-j} y(t_j) \right] \tag{2.81}$$

where:

$$\overline{w}_{n,0} = \frac{(n-1)^{1-\alpha} - n^{1-\alpha}}{\Gamma(2-\alpha)} \tag{2.82}$$

$$w_n = \begin{cases} \frac{1}{\Gamma(2-\alpha)} & \text{if } n = 0, \\ \frac{(n+1)^{1-\alpha} - 2n^{1-\alpha} + (n-1)^{1-\alpha}}{\Gamma(2-\alpha)} & \text{if } n \geq 1. \end{cases} \tag{2.83}$$

Special case $\alpha = 1$:

$$\overline{w}_{n,0} = 1, \quad w_0 = 1, \quad w_1 = -1, \quad w_n = 0 \text{ for } n \geq 2 \tag{2.84}$$

$$^{L1}\mathrm{D}_{t_0}^{1} y(t_n) = \frac{y_n - y_{n-1}}{h} \quad \text{(Standard difference quotient).} \tag{2.85}$$

Application to solve FDEs:

$$^{C}\mathrm{D}_{t_0}^{\alpha} y(t) = f(t, y(t)) \tag{2.86}$$

$$\begin{cases} ^{C}\mathrm{D}_{t_0}^{\alpha} y(t) = f(t, y(t)), \\ y(t_0) = y_0. \end{cases} \tag{2.87}$$

The solution becomes:

$$y_n = -\overline{w}_{n,0} y_0 - \sum_{j=1}^{n-1} w_{n-j} y_j + h^{\alpha} f(t_n, y_n) \tag{2.88}$$

- **L2 Algorithm** $(1 < \alpha \leq 2)$

Starting from the definition of Caputo's derivative for $1 < \alpha \leq 2$:

$$^{C}\mathrm{D}_{t_0}^{\alpha} y(t) = \frac{1}{\Gamma(2-\alpha)} \int_{t_0}^{t} (t-\tau)^{1-\alpha} y''(\tau) d\tau \tag{2.89}$$

- On a grid $t_n = t_0 + nh$, write the integral piecewise:

$$^{C}\mathrm{D}_{t_0}^{\alpha} y(t_n) = \frac{1}{\Gamma(2-\alpha)} \sum_{j=0}^{n-1} \int_{t_j}^{t_{j+1}} (t_n - \tau)^{1-\alpha} y''(\tau) d\tau \tag{2.90}$$

- On each interval $[t_j, t_{j+1}]$, approximate $y''(\tau)$ as:

$$y''(\tau) = \frac{y(t_{j+1}) - 2y(t_j) + y(t_{j-1})}{h^2} + \mathcal{O}(h) \quad \text{as } h \to 0 \tag{2.91}$$

Substitute and evaluate the integral exactly:

$$\int_{t_j}^{t_{j+1}} (t_n - \tau)^{1-\alpha} d\tau = h^{2-\alpha} \frac{(n-j)^{2-\alpha} - (n-j-1)^{2-\alpha}}{2-\alpha} \tag{2.92}$$

The L2 Approximation:

$$^{C}\mathrm{D}_{t_0}^{\alpha} y(t_n) = \frac{1}{h^{\alpha}\Gamma(3-\alpha)} \left[\bar{v}_{n,0} y(t_0) + \tilde{v}_{n,0} y(t_1) + \sum_{j=2}^{n} v_{n-j} y(t_j) \right] \tag{2.93}$$

General Formulation of Approximations (for $\alpha > 0$, $m-1 < \alpha \leq m$):

$$^{C}\mathrm{D}_{t_0}^{\alpha} y(t_n) \approx \frac{1}{h^{\alpha}} \left[\sum_{j=0}^{m-1} w_{n,j} y(t_j) + \sum_{j=m}^{n} w_{n-j} y(t_j) \right] \tag{2.94}$$

2.9.3 GL for Integrals

Methods based on integral formulations are powerful tools for solvingFDEs. These approaches reformulate FDEs into equivalent integral equations, leveraging the close relationship between fractional derivatives and integrals. This reformulation allows for the use of established numerical techniques, such as Volterra integral equations (VIEs), to address the challenges posed by the nonlocal nature of fractional calculus.

The integral formulation provides a flexible framework for numerical approximations, enabling techniques like product-integration rules, predictor-corrector methods, and fractional linear multistep methods. These methods are well-suited for handling the memory effects inherent in fractional systems, making them widely applicable in physics, engineering, and biology. By transforming FDEs into integral forms, these methods ensure stability and convergence while maintaining computational efficiency.

Reformulation in integral form:

$$\begin{cases} {}^{c}\mathrm{D}_{t_0}^{\alpha} y(t) = f(t, y(t)) \\ y(t_0) = y_0 \end{cases} \quad 0 < \alpha < 1 \quad \text{(for simplicity)} \tag{2.95}$$

Volterra integral equation formulation:

$$y(t) = y_0 + \frac{1}{\Gamma(\alpha)} \int_{t_0}^{t} (t-\tau)^{\alpha-1} f(\tau, y(\tau))\, d\tau \tag{2.96}$$

Reformulation in integral form for $\alpha > 0$ and $m-1 < \alpha \leq m$:

- **Volterra integral equation (VIE) formulation:**

$$y(t) = T_{m-1}(t) + \frac{1}{\Gamma(\alpha)} \int_{t_0}^{t} (t-\tau)^{\alpha-1} f(\tau, y(\tau))\, d\tau, \quad T_{m-1}(t) = \sum_{k=0}^{m-1} \frac{(t-t_0)^k}{k!} y_0^{(k)} \tag{2.97}$$

The GL definition of the fractional integral is given by:

$$J_{t_0}^{\alpha} f(t) = \lim_{h \to 0} h^{\alpha} \sum_{n=0}^{N} (-1)^n \binom{-\alpha}{n} f(t - nh), \quad N = \left\lfloor \frac{t - t_0}{h} \right\rfloor \tag{2.98}$$

where

$$(-1)^n \binom{-\alpha}{n} = (-1)^n \frac{\Gamma(-\alpha+1)}{n!\Gamma(-\alpha-n+1)} = \frac{\Gamma(\alpha+n)}{n!\Gamma(\alpha)}. \tag{2.99}$$

Fixing the step size $h > 0$, we have:

$$y_n = T_{m-1}(t_n) + h^{\alpha} \sum_{j=0}^{n} (-1)^j \binom{-\alpha}{j} f(t_{n-j}, y_{n-j}). \tag{2.100}$$

2.9.4 Product-Integration Rules

Young's method, initially proposed in 1954 for Volterra integral equations (VIEs), garnered attention for its effectiveness in solving integral equations[79]. Its applicability expanded significantly when Diethelm et al. adapted it for FDEs in 1999[80]. This work introduced a predictor-corrector scheme that enhanced the robustness and efficiency of the method for solving FDEs, leading to its widespread use in fractional calculus. The method has been further generalized into four different solution approaches, each improving accuracy and computational efficiency in solving fractional differential equations. These methods include the explicit rectangular rule, implicit rectangular rule, implicit trapezoidal rule, and product-integration rules using higher-degree interpolants.

The main idea is as follows:

(1) On a grid $t_n = t_0 + nh$, write the VIE in a piecewise manner:

$$y(t_n) = T_{m-1}(t_n) + \frac{1}{\Gamma(\alpha)} \sum_{j=0}^{n-1} \int_{t_j}^{t_{j+1}} (t_n - \tau)^{\alpha-1} f(\tau, y(\tau))\, d\tau \tag{2.101}$$

(2) Approximate $f(\tau, y(\tau))$ on $[t_j, t_{j+1}]$ using a k-degree interpolant polynomial.

(3) Evaluate the integral exactly.

1. **Product-Integration Rules: Explicit rectangular rule**

$$y(t_n) = T_{m-1}(t_n) + \frac{1}{\Gamma(\alpha)} \sum_{j=0}^{n-1} \int_{t_j}^{t_{j+1}} (t_n - \tau)^{\alpha-1} f(t_j, y_j)\, d\tau \tag{2.102}$$

For the 0-degree polynomial $f(\tau, y(\tau)) \approx f(t_j, y_j)$ on $\tau \in [t_j, t_{j+1}]$, the explicit integral becomes:

$$\frac{1}{\Gamma(\alpha)} \int_{t_j}^{t_{j+1}} (t_n - \tau)^{\alpha-1} f(t_j, y_j)\, d\tau = \frac{(t_n - t_j)^{\alpha} - (t_n - t_{j+1})^{\alpha}}{\Gamma(\alpha+1)} f(t_j, y_j). \tag{2.103}$$

This leads to:

$$y_n = T_{m-1}(t_n) + h^{\alpha} \sum_{j=0}^{n-1} b_{n-j-1}^{(\alpha)} f(t_j, y_j), \tag{2.104}$$

where

$$b_n^{(\alpha)} = \frac{(n+1)^\alpha - n^\alpha}{\Gamma(\alpha+1)}.$$

2. **Product-Integration: Implicit rectangular rule**.

   For the implicit rule, we approximate $f(\tau, y(\tau))$ by $f(t_{j+1}, y_{j+1})$ on $\tau \in [t_j, t_{j+1}]$, yielding:

$$y_n = T_{m-1}(t_n) + h^\alpha \sum_{j=1}^{n} b_{n-j}^{(\alpha)} f(t_j, y_j), \tag{2.105}$$

3. **Product-Integration: Implicit trapezoidal rule**

   Using a 1-degree interpolant polynomial:

$$f(\tau, y(\tau)) \approx \frac{\tau - t_{j+1}}{t_j - t_{j+1}} f(t_j, y_j) + \frac{\tau - t_j}{t_{j+1} - t_j} f(t_{j+1}, y_{j+1}) \quad \tau \in [t_j, t_{j+1}], \tag{2.106}$$

   the integral is computed as shown in the following equations.

   The final result is:

$$y(t_n) = T_{m-1}(t_n) + h^\alpha \left(\tilde{a}_n^{(\alpha)} f(t_0, y_0) + \sum_{j=1}^{n} a_{n-j}^{(\alpha)} f(t_j, y_j) \right), \tag{2.107}$$

   where:

$$\tilde{a}_n^{(\alpha)} = \frac{(n-1)^{\alpha+1} - n^{\alpha+1}(n-\alpha-1)}{\Gamma(\alpha+2)}, \quad a_n^{(\alpha)} = \begin{cases} \frac{1}{\Gamma(\alpha+2)} & \text{if } n = 0, \\ \frac{(n-1)^{\alpha+1} - 2n^{\alpha+1} + (n+1)^{\alpha+1}}{\Gamma(\alpha+2)} & \text{if } n = 1, 2, \ldots \end{cases}$$

2.9.4.1 Convergence order of Product-Integration rules

The error in the approximation can be expressed as:

$$y(t_n) - y_n = \mathcal{O}(h^P). \tag{2.108}$$

Theorem 3 *If* $f(t,y(t)) \in \mathcal{C}^{k+1}[t_0,T]$, *then*

$$y(t_n) - y_n = \mathcal{O}(h^{k+1}). \tag{2.109}$$

(1) Explicit Rectangular Rule:

$$|y(t_n) - y_n| = \mathcal{O}(h^{\alpha}). \tag{2.110}$$

(2) Implicit Rectangular Rule:

$$|y(t_n) - y_n| = \mathcal{O}(h^{\alpha+1}). \tag{2.111}$$

(3) Implicit Trapezoidal Rule:

$$|y(t_n) - y_n| = \mathcal{O}(h^{\alpha+1}). \tag{2.112}$$

2.9.4.2 Generalization of Product-Integration rules

The generalization of these rules entails employing a mix of higher-degree interpolants and advanced integral approximations, enhancing accuracy and convergence.

To circumvent solving the nonlinear equations in Equation (2.107) for the assessment of y_n, a predictor-corrector (PC) method is occasionally favored. This method involves initially estimating y_n using the explicit PI rectangular rule (2.104), followed by a correction through the implicit PI trapezoidal rule (2.107) as outlined:

$$\begin{cases} y_n^p = T_{m-1}[y;t_0](t_n) + h^{\alpha} \sum_{j=0}^{n-1} b_{n-j-1}^{(\alpha)} f(t_j,y_j), \\ y_n = T_{m-1}[y;t_0](t_n) + h^{\alpha} \left(\tilde{a}_n^{(\alpha)} f_0 + \sum_{j=1}^{n-1} a_{n-j}^{(\alpha)} f(t_j,y_j) + a_0^{(\alpha)} f(t_n,y_P^n) \right), \end{cases} \tag{2.113}$$

where y_P^n represents the predicted value and y_n denotes the corrected value.

The PC approach for FDEs has been well examined (see, for example, [81–84]. To enhance the approximation, numerous corrective iterations, denoted as m, may be employed:

$$\begin{cases} y_P^n = T_{m-1}[y;t_0](t_n) + h^\alpha \sum_{j=0}^{n-1} b_{n-j-1}^{(\alpha)} f(t_j, y_j), \\ y_n = T_{m-1}[y;t_0](t_n) + h^\alpha \left(\tilde{a}_n^{(\alpha)} f_0 + \sum_{j=1}^{n-1} a_{n-j}^{(\alpha)} f(t_j, y_j) + a_0^{(\alpha)} f(t_n, y_P^n) \right), \quad \mu = 1, 2, \ldots \end{cases} \tag{2.114}$$

Each repetition is anticipated to enhance the order of convergence from the first-order convergence of the predictor technique until the convergence order of the corrector method is attained. Generally, only a single or a limited number of correction iterations are required. The explicit PI rectangle rule (2.104) is derived for $m = 0$, whereas the typical predictor-corrector approach (2.113) necessitates $m = 1$.

2.9.5 Fractional Linear Multistep Methods

One of the most efficient classes of numerical schemes for solving FDEss is the family of Fractional Linear Multistep Methods (FLMMs). These methods:

- Were developed by Lubich between 1986 and 1988 [85, 86].
- Represent an extension of classical Linear Multistep Methods (LMMs) for ordinary and integral differential equations (IDEs) to the fractional-order case.
- Are based on convolution quadrature techniques, allowing for stable and accurate approximations of fractional derivatives.

The standard IDE:

$$\begin{cases} y'(t) = f(t, y(t)) \\ y(t_0) = y_0. \end{cases} \tag{2.115}$$

Standard LMM for IDEs:

$$\sum_{j=0}^{k} \rho_j y_{n-j} = h \sum_{j=0}^{k} \sigma_j f(t_{n-j}, y_{n-j}), \quad n \geq k. \tag{2.116}$$

First and second characteristic polynomials:

$$\rho(\xi) = \sum_{j=0}^{k} \rho_j \xi^{k-j}, \quad \sigma(\xi) = \sum_{j=0}^{k} \sigma_j \xi^{k-j} \tag{2.117}$$

Generating function of the Linear Multistep Methods (LMM):

$$\delta(\xi) = \frac{\rho(1/\xi)}{\sigma(1/\xi)} \tag{2.118}$$

When applied to IDE:

$$y'(t) = f(t, y(t)) \quad \Leftrightarrow \quad y(t) = y_0 + \int_{t_0}^{t} f(\tau, y(\tau))\, d\tau \tag{2.119}$$

Laplace transform:

$$G(\tau) = f(\tau, y(\tau)) \quad \int_{t_0}^{t} G(\tau)\, d\tau \div s^{-1}\hat{G}(s) \tag{2.120}$$

LMM in the form of convolution quadrature:

$$y_n = y_0 + h\sum_{j=0}^{k-1} w_{n,j} f(t_j, y_j) + h\sum_{j=0}^{n} w_{n-j} f(t_j, y_j), \quad \sum_{j=0}^{\infty} w_n \xi^n = \left(\frac{\delta(\xi)}{h}\right)^{-1} \tag{2.121}$$

When applied to FDEs ($0 < \alpha < 1$):

$${}^{c}D_{t_0}^{\alpha}(t) = f(t, y(t)) \quad \Leftrightarrow \quad y(t) = y_0 + \frac{1}{\Gamma(\alpha)} \int_{t_0}^{t} (t-\tau)^{\alpha-1} f(\tau, y(\tau))\, d\tau \tag{2.122}$$

Laplace transform:

$$G(\tau) = f(\tau, y(\tau)) \quad \frac{1}{\Gamma(\alpha)} \int_{t_0}^{t} (t-\tau)^{\alpha-1} G(\tau)\, d\tau \div s^{-\alpha} G(s) \tag{2.123}$$

Convolution quadrature for fractional-order problems:

$$y_n = y_0 + h^{\alpha}\sum_{j=0}^{s} w_{n,j} f(t_j, y_j) + h^{\alpha}\sum_{j=0}^{n} w_{n-j} f(t_j, y_j), \quad \sum_{j=0}^{\infty} w_n \xi^n = (\delta(\xi))^{-\alpha} \tag{2.124}$$

$$y_n = y_0 + \underbrace{h^\alpha \sum_{j=0}^{s} w_{n,j} f(t_j, y_j)}_{\text{Starting term}} + \underbrace{h^\alpha \sum_{j=0}^{n} w_{n-j} f(t_j, y_j)}_{\text{Convolution term}} \tag{2.125}$$

Convolution term:

$$h^\alpha \sum_{j=0}^{n} w_{n-j} f(t_j, y_j) \quad \text{is a discretization of} \quad \frac{1}{\Gamma(\alpha)} \int_{t_0}^{t} (t-\tau)^{\alpha-1} f(\tau, y(\tau))\, d\tau \tag{2.126}$$

$$\sum_{j=0}^{n} w_n \xi^n = (\delta(\xi))^{-\alpha} \tag{2.127}$$

$$\delta(\xi) = \frac{\rho(1/\xi)}{\sigma(1/\xi)} \tag{2.128}$$

Where ρ and σ are the characteristic polynomials of the LMM.

Starting term:

$$h^\alpha \sum_{j=0}^{s} w_{n,j} f(t_j, y_j) \quad \text{to couple with the singular behavior at} \quad t_0 \tag{2.129}$$

Coefficients obtained by imposing exact rule for $f(t, y(t)) = (t - t_0)^\nu, \quad \nu \in \mathcal{A}_p$:

$$\sum_{j=0}^{s} w_{n,j} j^\nu = -\sum_{j=0}^{n} w_{n-j} j^\nu + \frac{\Gamma(\nu+1)}{\Gamma(1+\nu+\alpha)} n^{\nu+\alpha}, \quad \nu \in \mathcal{A}_p \tag{2.130}$$

Where:

$$\mathcal{A}_p = \{\gamma \in \mathbb{R} \mid \gamma = i + j\alpha, i, j \in \mathbb{N}, \gamma < p-1\}, \quad s = |\mathcal{A}_p| - 1 \tag{2.131}$$

2.10 Conclusion

This chapter explored the foundations of fractional calculus and its application to FDEs. We began by introducing the key definitions (e.g., RL and Caputo derivatives), highlighting their properties and mathematical relationships. The chapter then focused on numerical methods for solving FDEs, such as product-integration and fractional linear multistep methods. These methods were analyzed in terms of their convergence behavior and computational strategies, including predictor-corrector schemes and convolution quadrature.

Altogether, this chapter provides a theoretical base for modeling complex systems — such as non-stationary biomedical signals — using fractional calculus, which will be applied in the following chapters.

Chapter 3

Mathematical Modeling of ECG Signals

3.1 Introduction

Mathematical modeling of ECG signals is a fundamental approach to quantitatively represent the heart's electrical activity and its manifestation on the body surface. The ECG signal is inherently complex, non-stationary, and subject to physiological variability and noise, which complicates its analysis and interpretation. Mathematical models provide a rigorous framework to capture these complexities, enabling improved diagnostics, signal synthesis, and a deeper understanding of cardiac electrophysiology. Various mathematical methods have been developed to model ECG signals, ranging from detailed biophysical simulations to simplified dynamical and statistical models. This chapter provides an overview of these mathematical modeling methods, emphasizing their strengths and limitations. Particular focus is given to IDE and FDEs based models, which balance physiological relevance and computational efficiency. Subsequently, the chapter discusses optimization methods used to estimate model parameters accurately, highlighting genetic algorithms and grey wolf optimization due to their effectiveness in ECG parameter fitting [87]. This chapter lays the groundwork for the next chapter, which delves into ECG modeling using IDEs, by establishing the theoretical and practical context of mathematical ECG modeling.

3.2 Overview of Mathematical Models for ECG Signals

Mathematical modeling of ECG signals encompasses a variety of approaches, each designed to capture different aspects of the complex cardiac electrical activity. These methods can be broadly classified into four main categories:

1. **Biophysical PDE-Based Models** : The bidomain and monodomain models represent the classical and most physiologically detailed approaches to ECG modeling. They simulate the electrical potentials inside and outside cardiac cells using coupled partial differential equations (PDEs) that incorporate tissue anisotropy, cellular heterogeneity, and the interaction between the heart and torso. These models enable

realistic simulation of 12-lead ECGs with accurate waveform morphology and lead-specific polarity, reflecting the biophysical processes at the cellular and tissue levels. For example, Potse et al. [88] demonstrated how bidomain models can reproduce detailed ECG features by solving coupled PDEs with ionic membrane dynamics and torso conductivity. However, these models are computationally intensive and require significant numerical resources, which limits their use in real-time applications or large-scale simulations.

2. **Polynomial and Curve-Based Models**: To reduce computational complexity, polynomial approximations such as Bézier-Bernstein curves and Gaussian functions have been employed to model individual ECG wave components (P, QRS, T waves) with fewer parameters. These approaches provide smooth and flexible waveform approximations that facilitate efficient synthesis and feature extraction. Soontornvorn and Fujioka [89] used smoothing Bézier-Bernstein curves to optimally model ECG waveforms, achieving good accuracy in waveform reconstruction. While these models improve computational efficiency, they often lack direct physiological interpretability and do not explicitly model the underlying cardiac electrophysiology.

3. **Fourier and Transform-Based Models** :Fourier series and related transform methods represent ECG signals as sums of harmonic components, capturing their periodic and quasi-periodic characteristics with relatively low complexity. These methods are widely used for signal compression, noise filtering, and feature extraction. For instance, Sassi et al.[90] applied autoregressive (AR) spectral models to estimate dominant atrial cycle lengths during atrial fibrillation, demonstrating improved performance over traditional FFT-based spectral approaches. However, Fourier-based methods may struggle to capture the non-stationary and transient features of ECG signals, which are crucial for accurate diagnosis and modeling of arrhythmias.

4. **Statistical and Data-Driven Models**: Statistical approaches model ECG signals by extracting features that characterize variability and noise, improving robustness in real-world applications. Markov-chain Monte Carlo (MCMC) methods have been used to adaptively select ECG signal representations and track varying morphologies, as shown by Roonizi and Sassi [91]. Moreover, Markov models have

been applied to detect ECG instability preceding cardiac arrest, achieving high classification accuracy (ROC AUC of 82%) in clinical datasets . Autoregressive models also serve as effective tools for spectral parameter estimation and feature extraction, particularly in pathological conditions such as atrial fibrillation.

5. **Simplified Gaussian-Based Models:** Models using sums of Gaussian functions represent ECG morphology simply and efficiently, often combined with hybrid optimization techniques for parameter fitting

   This overview highlights the diversity of mathematical methods available for ECG modeling, ranging from detailed biophysical simulations to efficient statistical and transform-based techniques. While each approach has its merits, the choice of model depends on the balance between physiological accuracy, computational feasibility, and the specific application requirements. The following sections focus on IDE and FDEs models, which offer a promising compromise by combining physiological relevance with computational efficiency and flexibility.

3.3 Focus on IDE and FDE Modeling Methods

Mathematical modeling of ECG signals using IDE and FDEs has gained significant attention due to their ability to capture the essential dynamics of cardiac electrical activity while maintaining computational tractability.

3.3.1 IDE Models

IDE-based models represent the ECG waveform as trajectories of a dynamical system in a low-dimensional state space. Typically, these models decompose the ECG signal into its characteristic components—P wave, QRS complex, and T wave—each modeled by localized functions such as Gaussian terms positioned at specific angular locations on a limit cycle. The system of coupled IDEs governs the evolution of the state variables, with parameters controlling the amplitude, width, and timing of each wave, as well as heart rate variability through angular velocity around the limit cycle.

One of the most influential models in the field of synthetic ECG signal generation is the dynamical model developed by McSharry et al.[24]. This approach introduced a physiologically inspired and mathematically rigorous framework based on a system of IDE, enabling the simulation of realistic ECG waveforms. The model is especially valuable for testing biomedical signal processing algorithms, validating clinical diagnostic tools, and studying heart rate variability (HRV) under both healthy and pathological conditions.

The McSharry model is a two-stage synthetic ECG generator composed of:

- **Stage 1: Heart Rate Variability Modeling**:The model begins by generating a time series of RR intervals that captures important temporal characteristics of cardiac dynamics, including the average heart rate and physiological variability such as respiratory sinus arrhythmia and Mayer waves. This is accomplished using a power spectrum composed of low- and high-frequency components to emulate autonomic modulation of heart rate.
- **Stage 2: ECG Waveform Synthesis via IDEs** A synthetic ECG signal is then generated from a 3D dynamical system governed by three coupled IDEs. The trajectory moves in a circular path on the (x, y)-plane—representing the cardiac phase—while the z-component captures the ECG morphology. Distinct waves (P, Q, R, S, T) are modeled as Gaussian functions, modulating the z-direction as the trajectory passes through fixed angular positions on the unit circle.

The dynamical model of McSharry is given by:

$$\begin{cases} \dot{x}_1 &= \alpha x_1 - w x_2, \\ \dot{x}_2 &= \alpha x_2 + w x_1, \\ \dot{x}_3 &= \sum_{i \in \{P,Q,R,S,T\}} a_i \Delta\theta_i \exp\left(-\frac{\Delta\theta_i^2}{2b_i^2}\right) - (x_3 - z_0). \end{cases} \tag{3.1}$$

Here:

- $\alpha = 1 - \sqrt{x^2 + y^2}$ ensures the trajectory evolves on a unit circle.
- w is the angular velocity determining the heart rate.
- θ represents the angle around the circle.

- $\Delta\theta_i = (\theta - \theta_i) \mod 2\pi$ is the angular difference for the ith Gaussian kernel.
- a_i, b_i, and ϕ_i are the amplitude, width, and location of the ith wave (P, QRS, T) respectively.

w represents the angular velocity as it traverses the cycle limit. The baseline wander was introduced by linking the baseline value in equation (3.1) to the respiratory frequency by utilizing:

$$z_0(t) = A\sin(2\pi f_2 t), \tag{3.2}$$

Where A = 0.15 mV , $f_2 = 0.25$.

McSharry et al. used to generate healthy ECG signals the typical parameters as shown in Table 3.1.

Table 3.1: Parameters of the ECG model used in Equation 3.1.

Index (i)	**P**	**Q**	**R**	**S**	**T**
Time (s)	-0.2	-0.05	0	0.05	0.3
θ_i	$-\frac{\pi}{3}$	$-\frac{\pi}{12}$	0	$\frac{\pi}{12}$	$\frac{\pi}{2}$
a_i	1.2	-5.0	30.0	-7.5	0.75
b_i	0.25	0.1	0.1	0.1	0.4

The model is numerically integrated using standard methods such as the fourth-order Runge-Kutta algorithm or Euler's method. The z-component of the solution, z(t), directly represents the synthetic ECG waveform.

A critical feature of this model is its ability to adjust the R-R interval by varying the trajectory's angular velocity (denoted as ω), allowing for the simulation of both regular and irregular rhythms. This combination of Gaussian wave modelling and a dynamic cardiac rhythm framework makes the McSharry model a foundational tool for ECG analysis, advancing research and developing sophisticated processing methods.
Several researchers have expanded on IDE-based modelling approaches:

- **Dabanloo et al.**[11] improved the Zeeman model to include respiratory sinus arrhythmia, Mayer waves, and low-frequency heart rate variability.

- **Li and Ma** [92] introduced a method using piecewise curves to model the P wave, QRS complex, and T wave separately before combining them into a full heartbeat. While this approach adds precision, it also increases complexity due to the many parameters involved.

- **Sameni et al.** [12] proposed a 3D dynamic model using a single dipole to describe the heart's motion and rotation. While it addressed some challenges in multi-lead modelling, it struggled to capture low-frequency components, such as the P wave, accurately.

- **Clifford et al.**[13] extended Sameni's model with first-order Markov chains to simulate transitions between normal and pathological heartbeats.

- **Roonizi et al.** [14] explored signal decomposition methods, showing that B-splines provided the best local control for ECG modelling compared to other basis functions like sinusoidal or Bézier curves.

- **Gidea et al.**[15] developed a chaos-based model to replicate the heart's self-regulatory mechanisms.

- **Quiroz-Juárez et al.** [16] used three nonlinear oscillators to generate ECG data for healthy and rhythm-disturbed conditions.

Various studies have used Van der Pol oscillators to model ECG-like waveforms because they can generate self-sustained oscillations with adjustable amplitude and frequency. These properties make them well-suited to mimic the heart's rhythmic, quasi-periodic behaviour. Initially developed for electrical circuit analysis, Van der Pol oscillators have also proven effective in modelling biological signals, including cardiac rhythms.

- **Kaplan et al.** [20] applied a "filtered" Van der Pol oscillator to biological signal modelling, showing how filtering techniques can better shape oscillator outputs to resemble ECG waveforms

- **Gois and Savi** [21] studied heart rhythm dynamics using a system of three coupled Van der Pol oscillators. This model simulated interactions between oscillators, representing key cardiac features such as the coordination between atrial and ventricular contractions.

- **Ryzhii and Ryzhii** [23] introduced a heterogeneous coupled oscillator model combining multiple Van der Pol oscillators with varying parameters. This design improved the ability to simulate ECG signals under different heart conditions, including complex waveforms seen in arrhythmias.

The Van der Pol oscillator's adaptability in capturing the nonlinear dynamics of cardiac signals makes it a valuable tool for ECG modelling. However, achieving high physiological accuracy for specific features, such as the P and T waves, remains challenging. Despite these limitations, Van der Pol-based models have played a crucial role in advancing the understanding and simulation of ECG signals, aiding research and practical applications in cardiology.

3.3.2 FDEs Models

FDEs Models FDE models extend classical IDEs by incorporating fractional calculus, introducing memory and hereditary effects into system dynamics. This is particularly advantageous for modeling the non-stationary and fractal-like characteristics of ECG signals, which exhibit long-range temporal correlations and complex pathological alterations. FDE-based models provide enhanced accuracy and interpretability in capturing subtle temporal dependencies that integer-order models may overlook. Although still emerging, FDE methods represent a promising frontier in ECG modeling.

While traditional IDE have been widely used to model ECG signals, they face significant challenges in capturing cardiac electrical activity's complex and nonlinear dynamics. One fundamental limitation is the local nature of integer derivatives, which restricts their ability to represent long-term memory effects inherent in biological systems. IDEs have a fixed order, making them less flexible in modelling transitions between dynamic behaviors. As a result, while IDE-based models are mathematically straightforward, they may need more accuracy to fully represent the intricate dynamics of ECG signals and cardiac electrical phenomena.
FDEs offer a more advanced and adaptable approach to overcome these limitations. Unlike IDEs, FDEs involve derivatives of non-integer order, allowing them to incorporate memory effects and model complex system dynamics with greater precision. This flexibility enables FDEs better to capture the time-dependent and nonlinear characteristics

of ECG signals.

FDEs have been successfully applied across various scientific fields, demonstrating their effectiveness in modelling real-world systems:

- **Mathematical Epidemiology** : Researchers have used FDEs to study diseases like bovine babesiosis, analyzing their dynamics with fractional-order models to capture long-term effects and variability [27].
- **Mathematical Biology** : FDEs have been applied to epidemic models, incorporating memory effects to more accurately study disease spread and global dynamics [28].
- **Biochemical Kinetics** : Hybrid proportional fractional derivatives have been employed to forecast enzymatic reactions, providing insights into the dynamics of enzyme-substrate interactions and reaction rates [29, 31].
- **Mathematical Oncology and Epidemiology** : Fractional-order models have been used to explore the chaotic dynamics of HIV-1 and AIDS-associated cancer cells, highlighting their utility in representing complex biological processes [30].

3.3.2.1 Applications of FDEs in ECG Modeling

In the specific domain of ECG signal modelling, FDEs have shown promise in improving the accuracy and flexibility of models:

- One of the pioneering approaches in this area is the work of Das and Maharatna [25], who proposed a novel fractional dynamical model based on filtered, coupled Van der Pol (VdP) oscillators. Their framework utilizes incommensurate fractional-order differential equations, which incorporate memory effects and nonlinear dynamics to more faithfully reproduce the temporal and morphological characteristics of real ECG signals—particularly the QRS complex.

  The model consists of two coupled Van der Pol oscillators, each described by a set of three FDEs. The oscillators are coupled with a time delay to simulate the interaction between the left and right cardiac pacemakers. A first-order low-pass filter is applied to each oscillator's output to produce ECG-like signals. Crucially, the use of fractional derivatives allows the system to emulate the long-term memory and hereditary properties intrinsic to cardiac tissue.

The complete system is described by the following equations:

$$\begin{cases} D^{q_1}x_1(t) = y_1(t) + \varepsilon\left[x_2(t-\tau) - x_1(t)\right] \\ D^{q_2}y_1(t) = \mu_1\left[1 - x_1(t)^2\right]y_1(t) - x_1(t) \\ D^{q_3}z_1(t) = -\alpha z_1(t) + \beta x_1(t) \\ D^{q_4}x_2(t) = y_2(t) + \varepsilon\left[x_1(t-\tau) - x_2(t)\right] \\ D^{q_5}y_2(t) = \mu_2\left[1 - x_2(t)^2\right]y_2(t) - x_2(t) \\ D^{q_6}z_2(t) = -\alpha z_2(t) + \beta x_2(t) \end{cases} \tag{3.3}$$

Where:

- D^{q_i} denotes the Caputo fractional derivative of order $q_i \in (0,1]$,
- $x_i(t)$, $y_i(t)$, and $z_i(t)$ are the state variables of the i-th oscillator, where $i = 1,2$.
- μ_1, μ_2 govern the nonlinearity in each Van der Pol oscillator.
- ε is the coupling strength between the oscillators.
- τ is a time delay representing inter-ventricular conduction latency.
- α and β define the low-pass filtering characteristics.

The ECG-like output is derived from the filtered oscillator signals, typically using:

$$\mathrm{ECG}(t) = z_1(t) + z_2(t) \tag{3.4}$$

or alternatively,

$$\mathrm{ECG}(t) = z_1(t) \tag{3.5}$$

This model captures essential ECG features, including the QRS complex, and with appropriate tuning of the fractional orders and parameters, it can also approximate the full P-QRS-T waveform. Moreover, it is capable of generating both normal and pathological rhythms.

The key characteristics of this model include:

- **Fractional-Order Dynamics:** The incommensurate nature ($q_1 \neq q_2 \neq \cdots \neq q_6$) allows modeling of distinct memory behaviors in different cardiac components.
- **Nonlinearity:** Each oscillator contains the Van der Pol term $\mu_i(1 - x_i^2)y_i$, generating self-sustained oscillations mimicking pacemaker activity.
- **Delay Coupling:** The delay τ introduces synchronization and phase shift, enhancing physiological realism.
- **Filtering:** The variables $z_i(t)$ serve as smoothed outputs, closely resembling realistic ECG morphologies.

The model parameters and fractional orders can be optimized using metaheuristic algorithms such as genetic algorithms (GA) or particle swarm optimization (PSO) to fit actual ECG data or simulate specific pathologies.

This model offers:

1. High flexibility in reproducing diverse ECG morphologies,
2. A physiologically inspired structure incorporating memory and nonlinearity,
3. A platform for in silico investigations of arrhythmias and other cardiovascular abnormalities.

The Das and Maharatna model[25] represents a significant advancement in synthetic ECG modeling, providing a robust foundation for future research in simulation-based diagnostics, algorithm validation, and non-invasive monitoring.

- **Templos-Hernández et al.** developed a six-equation fractional-order model for cardiac rhythm analysis, aiming for a more comprehensive representation of ECG waveforms. However, the model struggled with accuracy, particularly when simulating complex pathological patterns [26].

The exploration of FDEs in ECG signal modeling demonstrates their considerable potential for advancing the field. In comparison to traditional IDE-based approaches—such as the widely cited model by McSharry et al. [24] —FDEs provide a more sophisticated framework for capturing the intrinsic memory effects and nonlinear dynamics of cardiac electrophysiology. Although the McSharry model has served as a foundational tool for generating synthetic ECG signals with high physiological fidelity, it exhibits limitations in accurately simulating pathological conditions and in reproducing less prominent waveform components such as the P and T waves.

The progression from IDE-based to FDE-based modeling reflects a significant methodological advancement, offering improved representational power for cardiac signal variability and long-term dependencies. By incorporating fractional-order dynamics, FDE models enhance the realism of synthetic ECG signals and expand their applicability to more complex physiological and pathological scenarios. Nevertheless, the current generation of FDE-based models still requires further refinement to fully address the challenges of modeling diverse pathological morphologies and achieving high precision in waveform morphology.

Therefore, continued research is essential to optimize these models by integrating more comprehensive physiological constraints, adaptive parameterization, and validation against real-world clinical data. These improvements will be critical for developing robust and clinically meaningful tools for ECG signal analysis, biomedical research, and diagnostic applications.

3.4 The Role of Optimization Methods in Parameter Estimation

Accurate parameter estimation is essential for the success of mathematical ECG models, as the choice of parameters directly affects the fidelity of waveform reconstruction and the model's ability to simulate a wide range of cardiac conditions. Precise parameter tuning ensures that the models can reliably reproduce the morphological and temporal features of ECG signals, which is critical for applications such as noise reduction, feature extraction, arrhythmia detection, and classification.

Optimization methods for ECG model parameter estimation broadly include classical gradient-based algorithms, heuristic approaches, and metaheuristic techniques. Given the nonlinear, multimodal, and often high-dimensional nature of the parameter space, heuristic and metaheuristic methods are generally preferred. These methods excel at avoiding local minima and navigating complex optimization landscapes, which are common challenges in ECG modeling.

This section focuses on two advanced metaheuristic optimization algorithms— GA and GWO—which have shown promising results in ECG parameter estimation tasks. GA, inspired by the principles of natural selection and evolution, iteratively evolve a population of candidate solutions through selection, crossover, and mutation operations to explore the search space effectively. GWO, a nature-inspired algorithm modeled after the social hierarchy and cooperative hunting strategies of grey wolves, balances exploration and exploitation to efficiently converge on optimal solutions.

By leveraging these powerful optimization techniques, ECG modeling can achieve enhanced accuracy and robustness, enabling better fitting of model parameters to real ECG data. This not only improves the quality of synthetic ECG generation but also strengthens downstream applications such as disease diagnosis and personalized cardiac monitoring

3.4.1 GA and Its Application in Parameter Estimation

3.4.1.1 Overview of GA

GAs are optimization methods inspired by natural selection in biology. They are handy for solving complex problems where traditional methods struggle. GAs work by simulating evolution: they start with a group of potential solutions (called a population) and improve them over time using operators like selection, crossover, and mutation. This iterative process helps discover better solutions with each generation [93]

3.4.1.2 Role of GA in coefficient Estimation

Estimating coefficients is an essential task in many areas of science and engineering. The goal is to find parameter values that best describe a system or fit observed data. Traditional techniques, such as gradient-based methods, often fail when dealing with non-linear, noisy, or high-dimensional data. GAs overcome these challenges by exploring a broad solution space, reducing the likelihood of getting stuck in local optima [94]

3.4.1.3 Chromosome Representation and Fitness Function

In GAs for coefficient estimation, a chromosome represents the parameters to be estimated. GAs can be used in parameter optimization problems by encoding a set of parameters in the chromosome of the population. Each chromosome represents a possible set of parameters of the system to be optimized, expressed as:

$$\text{chromosome} = [x_1, x_2, x_3, \ldots, x_k] \tag{3.6}$$

The chromosome with the highest fitness, as determined by the GA, provides the optimum set of parameters.

The structure of a chromosome depends on the type of encoding used. Binary, real, "gray," and other encoding methods have been applied, with binary encoding being closer to Holland's theory and more extensively studied. In binary encoding, each real parameter is mapped to a binary number (substring). Since this approach maps a continuous variable to a discrete one, the length of the binary string is determined based on the desired precision.

The fitness function evaluates how well the parameters fit the data. Standard metrics include the MSE between real and synthetic ECG signals to assess how closely the model's predictions align with the observed values [95].

3.4.1.4 Genetic Operators in coefficient Estimation

GAs use several operators to refine solutions. These steps are repeated across generations until the algorithm converges to an optimal or near-optimal solution(see the following flowchart):

1. **Population:** A set of potential solutions, each represented as a chromosome.
2. **Selection:** Choosing the best solutions to create the next generation based on their fitness.
3. **Crossover:** Combining two solutions to create offspring with characteristics from both parents.
4. **Mutation:** Introducing small random changes to maintain diversity and explore new solutions.
5. **Fitness Function:** Evaluating each solution's performance based on the problem's objective [96]

These steps are repeated across generations until the algorithm converges to an optimal or near-optimal solution (see the following flowchart).

3.4.1.5 Application of GAs in Parameter Estimation

GAs are widely used in parameter estimation for their ability to handle complex, non-linear, and high-dimensional problems. Key applications include:

1. **Engineering Optimization:** GAs optimize structural dimensions or material properties to meet safety and durability requirements while minimizing costs. This is particularly useful in systems with complex constraints [93]
2. **Machine Learning:** GAs fine-tune hyperparameters in models like neural networks, such as learning rates or the number of layers, to improve performance (Golberg, 1989)[97]
3. **Medical Diagnostics:** For example, GAs optimize models for classifying ECG signals to detect ischemic beats, enhancing accuracy and robustness.
4. **Cardiovascular Disease Prediction:** With neural networks, GAs improve disease prediction accuracy based on patient data [98].
5. **Multi-Objective Optimization:** GAs balance conflicting objectives, such as cost

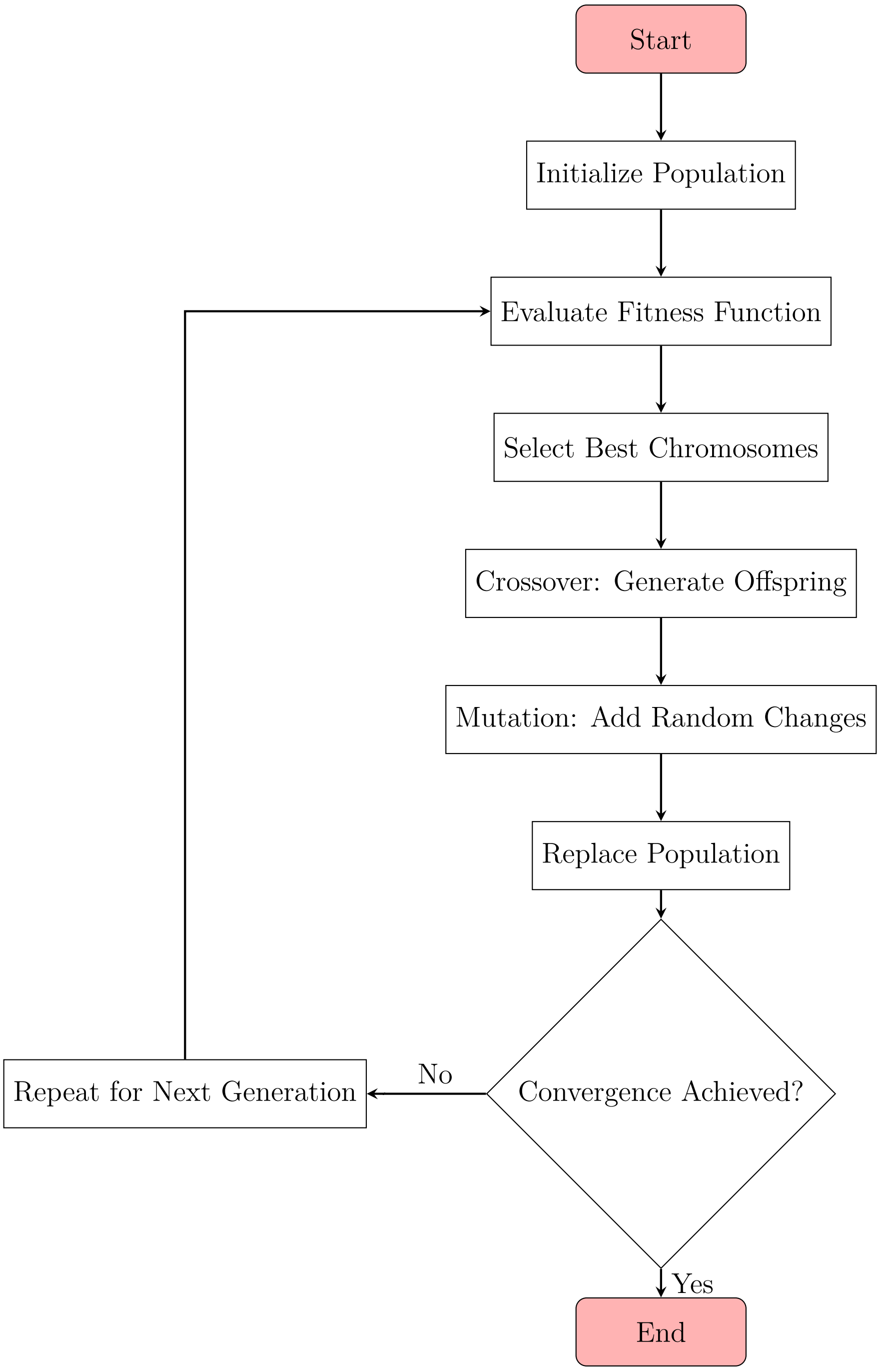

Figure 3.1: Flowchart of the Genetic Algorithm Cycle.

and reliability, in network models and similar systems [96].

3.4.1.6 Advantages of GAs in Coefficient Estimation

GAs offer several benefits:

- **Global Search:** They explore a vast solution space and avoid local optima.
- **Flexibility:** GAs can handle continuous, discrete, and mixed parameters.

- **Robustness:** They perform well even with noisy or incomplete data.
- **Multi-Objective Optimization:** GAs can balance conflicting goals effectively [96].

GAs are powerful for estimating coefficients, particularly in complex and challenging problems. By mimicking evolution, they explore solutions effectively and adapt to various applications, including engineering, machine learning, and medical diagnostics. Continued advancements in GAs will expand their potential for tackling even more demanding optimization tasks.

3.4.2 Grey Wolf Optimizer and Its Application in Parameter Estimation

3.4.2.1 Overview of the GWO

The GWO is a bio-inspired metaheuristic algorithm developed by Mirjalili et al, drawing inspiration from grey wolves' social structure and hunting tactics. The algorithm categorizes solutions into a hierarchical framework comprising alpha (α), beta (β), delta (δ), and omega (ω) wolves. This organization governs how wolves interact and navigate the solution space. The GWO algorithm is widely recognized for its simplicity, robustness, and capability to solve various optimization problems effectively [99, 100].

3.4.2.2 Mechanisms of the GWO Algorithm

The GWO algorithm operates based on three fundamental mechanisms, which are mathematically modelled to balance exploration and exploitation:

1. **Encircling Prey:**

   Wolves position themselves around the prey, modelled as:

$$\mathbf{X}(t+1) = \mathbf{X}_p(t) - \mathbf{A} \cdot |\mathbf{C} \cdot \mathbf{X}_p(t) - \mathbf{X}(t)| \tag{3.7}$$

   Here:

   - $\mathbf{X}(t)$: Position of a wolf at iteration t,

  - $\mathbf{X}_p(t)$: Position of the prey (optimal solution),
  - $\mathbf{A} \quad and \quad \mathbf{C}$: Vectors controlling exploration and exploitation dynamics.

2. **Hunting:** The alpha, beta, and delta wolves guide the pack in locating prey. Wolves adjust their positions by considering the weighted influence of these top three wolves, ensuring a balanced search.

3. **Attacking and Searching:** The transition from exploration to exploitation is governed by the convergence parameter $|\mathbf{A}|$, which decreases over iterations, enabling wolves to fine-tune their positions as they approach the prey.

3.4.2.3 Flowchart of the GWO Algorithm

The following flowchart provides:

- A visual representation of the GWO's operational steps.
- Illustrating how wolves update their positions through encircling.
- Hunting.
- Attacking mechanisms to find the optimal solution.

3.4.2.4 Applications of GWO in Parameter Estimation

GWO has demonstrated exceptional performance in parameter estimation across various domains. Some notable applications include:

1. **Surface Wave Parameter Estimation:** Song et al.[101] used GWO for parameter estimation in surface wave models, achieving high accuracy and computational efficiency in geophysical studies [101].

2. **ECG Signal Denoising:** Deepak and Vijayakumar applied GWO to optimize thresholds for denoising ECG signals, enhancing diagnostic accuracy by preserving signal integrity [102].

3. **Overhead Transmission Line Systems:** Shaikh et al. employed GWO for parameter calculation in transmission line systems, demonstrating its ability to improve system performance [103].

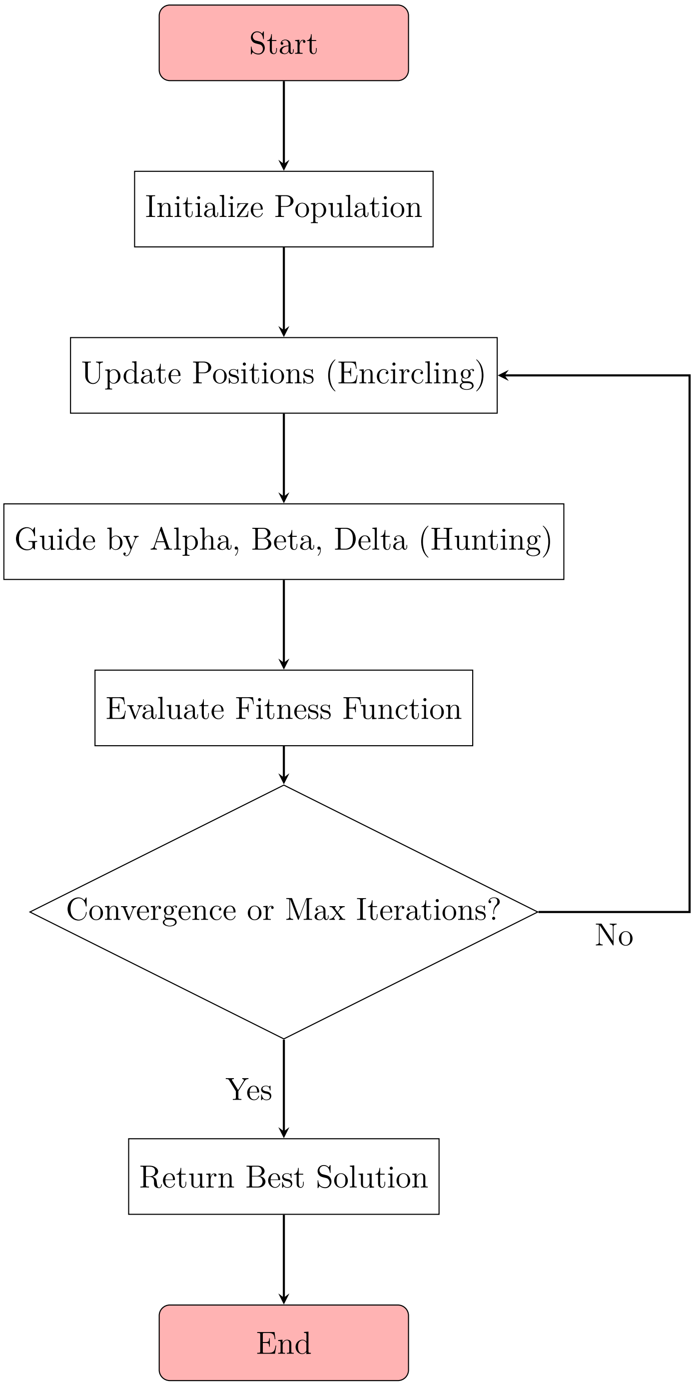

Figure 3.2: Improved Flowchart of the Grey Wolf Optimizer Algorithm with Fitness Evaluation.

4. **Time Series Classification:** Nsour et al. developed a hybrid GWO approach for time series classification, which improved accuracy and computational efficiency [104].

5. **Engineering Optimization:** GWO has been effectively applied in structural design, manufacturing systems, and energy management, showcasing its versatility

[105].

3.4.2.5 Advantages of GWO in Parameter Estimation

The GWO algorithm offers several benefits:

- **Global Search Capability:** Effectively avoids local optima by exploring a vast solution space [99].
- **Simple Implementation:** Minimal parameter tuning makes it computationally efficient [105].
- **Flexibility:** Suitable for optimization problems, including continuous, discrete, and mixed-variable types [100].
- **Balancing Exploration and Exploitation:** Dynamically adjusts control parameters to balance local and global search processes effectively [101].

3.4.2.6 Emerging Trends and Future Directions for GWO Applications

Ongoing research seeks to enhance GWO's efficiency and expand its applicability. Variants and hybrid models integrating GWO with techniques like Particle Swarm Optimization and genetic algorithms show promise for addressing multi-objective and high-dimensional problems. Future advancements aim to optimize its computational scalability and performance in fields such as artificial intelligence, bioinformatics, and renewable energy systems [105].

3.5 Conclusion

This chapter has presented a comprehensive overview of mathematical methods for ECG signal modeling, emphasizing the spectrum from detailed PDE-based biophysical models to efficient polynomial and transform-based approaches. It highlighted the particular importance of IDE and FDE models for their ability to balance physiological realism with computational tractability and to capture complex ECG dynamics.

Furthermore, the chapter underscored the critical role of optimization algorithms, especially GAs and GWO, in accurately estimating model parameters to ensure faithful

ECG signal representation. Building on this foundation, the next chapter will focus in detail on ECG modeling using integer differential equations (IDEs), exploring their formulation, parameterization, and applications in simulating both normal and pathological cardiac rhythms.

The chapter also discusses parameter optimization, a critical step in refining ECG models for precise simulations and analyses. Techniques such as the GA and GWO were highlighted for their efficacy in estimating parameters that enhance model accuracy. These optimization methods leverage nature-inspired principles to overcome challenges associated with traditional optimization techniques.

This chapter establishes a strong foundation for employing advanced mathematical and computational techniques in ECG modelling. It provides the theoretical and practical basis for subsequent discussions on applying these models in modelling ECG signals.

Chapter 4

Integer-Order Differential Equation Models for ECG Signal Generation

4.1 Introduction

The modeling of ECG signals has historically relied on systems of integer- order differential equations due to their analytical tractability and intuitive correspondence with physical systems. Among these, the McSharry model stands out as a benchmark, enabling the synthesis of realistic ECG signals via a limit-cycle oscillator approach. Despite their successes, integer-order models often lack the flexibility to account for complex, long-memory physiological behaviors.

In this chapter, we present and analyze two incremental yet significant contributions to ECG signal modeling based on IDEs. Both are derived from and expand upon the McSharry model, focusing on improving fidelity and physiological realism. The first contribution modifies the original IDE structure by introducing a novel Hopf bifurcation to enhance the system's; dynamic behavior. The second refines parameter estimation using optimization techniques, ensuring that synthetic signals align more closely with real clinical data.

These works serve a dual purpose: they establish a solid mathematical and physiological foundation for modeling the heart's; electrical activity and highlight the inherent limitations of integer-order formulations. These limitations—particularly in handling memory effects and capturing long-term dependencies—justify the transition in the next chapter to FDEs, which offer a more flexible and accurate framework for ECG modeling.

4.2 Generation of ECG synthetic signal using coupled integer differential equations and Hopf bifurcation

This section introduces a modeling technique for generating a synthetic ECG signal that exhibits realistic PQRST morphology and specified heart rate dynamics, encompassing numerous cardiac arrhythmias. The suggested model employs three interconnected IDEs, with the first two equations reliant on Hopf bifurcation. The fourth-order Runge—Kutta method is used to calculate the numerical solution for the model. This section proposes a modification of the McSharry et al. model by introducing a novel Hopf bifurcation mechanism in the first two differential equations, leading to a new formulation for synthetic ECG generation. The proposed approach enables the creation of diverse synthetic ECG signals that can offer clinically relevant insights into human cardiac dynamics.

4.2.0.1 The proposed model

We propose substituting the initial two equations of the McSharry model [24] (Equation 3.1) with a pair of nonlinear differential equations that exhibit a *Hopf bifurcation*, as described in [106]. The new equations are presented in Equation 4.1.

$$\begin{cases} \dot{x}_1 &= -\left(-g + x_1^2 + x_2^2\right) x_1 - w x_2, \\ \dot{x}_2 &= -\left(-g + x_1^2 + x_2^2\right) x_2 - w x_1, \end{cases} \tag{4.1}$$

Theoretical Foundation: A Hopf bifurcation is a critical point in the parameter space of a nonlinear dynamical system where a stable fixed point becomes unstable and gives rise to a stable limit cycle (or vice versa). This bifurcation typically occurs when a pair of complex conjugate eigenvalues of the system's Jacobian cross the imaginary axis as a parameter (here, g) is varied.

In the context of our model, the terms $(-g + x_1^2 + x_2^2)$ act as a control for the stability of the origin. When $g > 0$, the origin is an unstable spiral, and a stable limit cycle emerges—a hallmark of a supercritical Hopf bifurcation. This behavior closely resembles the rhythmic oscillations of the heart and thus serves as a mathematically grounded framework for modeling the pseudo-periodic nature of ECG signals.

By choosing $g = -1$, we set the system near a subcritical regime where small perturbations can lead to sustained oscillations. The angular velocity w determines the speed of rotation around the origin in the phase space.

Full Model Description We extend the Hopf-based system by integrating a third equation that synthesizes the morphological components of the ECG (P, QRS, T waves), similar to the original McSharry formulation. The full model is defined in Equation 4.2

[5]:

$$\begin{cases} \dot{x}_1 &= -\left(-g+x_1^2+x_2^2\right)x_1 - wx_2, \\ \dot{x}_2 &= -\left(-g+x_1^2+x_2^2\right)x_2 - wx_1, \\ \dot{x}_3 &= \sum_{i\in\{P,Q,R,S,T\}} a_i \Delta\theta_i \exp\left(-\frac{\Delta\theta_i^2}{2b_i^2}\right) - (x_3 - z_0). \end{cases} \tag{4.2}$$

We fix the bifurcation parameter as $g = -1$. The parameter w represents the angular frequency governing the circular trajectory of (x_1, x_2), akin to the trajectory around the unit circle in the phase space.

Numerical Integration The system of ordinary differential equations in Equation 4.2 is solved using the classical fourth-order Runge-Kutta method, which is known for its balance of accuracy and computational efficiency. The general form is:

$$\frac{d\overrightarrow{x}}{dt} = \overrightarrow{f}(t, \overrightarrow{x}), \quad \overrightarrow{x}(t_0) = \overrightarrow{x_0}, \tag{4.3}$$

where $\overrightarrow{x} = \begin{pmatrix} x_1 \\ x_2 \\ x_3 \end{pmatrix}$ and

$$\overrightarrow{f}(t, \overrightarrow{x}) = \begin{pmatrix} -(x_1+x_2) - (x_1^2+x_2^2)x_1 \\ -(x_1+x_2) - (x_1^2+x_2^2)x_2 \\ \sum_{i\in\{P,Q,R,S,T\}} a_i\,\Delta\theta_i\,\exp\left(-\frac{(\Delta\theta_i)^2}{2b_i^2}\right) - (x_3 - z_0) \end{pmatrix} \tag{4.4}$$

The Runge-Kutta update formula is:

$$\overrightarrow{x}_{n+1} = \overrightarrow{x}_n + \frac{h}{6}\left(\overrightarrow{k_1} + 2\overrightarrow{k_2} + 2\overrightarrow{k_3} + \overrightarrow{k_4}\right), \tag{4.5}$$

with time step $h = \frac{1}{f_s}$, where f_s is the sampling frequency.

The Runge-Kutta coefficients are computed as:

$$\overrightarrow{k_1} = \overrightarrow{f}(t_n, \overrightarrow{x}_n), \tag{4.6}$$

$$\overrightarrow{k_2} = \overrightarrow{f}\left(t_n + \frac{h}{2}, \overrightarrow{x}_n + \frac{h}{2}\overrightarrow{k_1}\right), \tag{4.7}$$

$$\overrightarrow{k_3} = \overrightarrow{f}\left(t_n + \frac{h}{2}, \overrightarrow{x}_n + \frac{h}{2}\overrightarrow{k_2}\right), \tag{4.8}$$

$$\overrightarrow{k_4} = \overrightarrow{f}(t_n + h, \overrightarrow{x}_n + h\overrightarrow{k_3}). \tag{4.9}$$

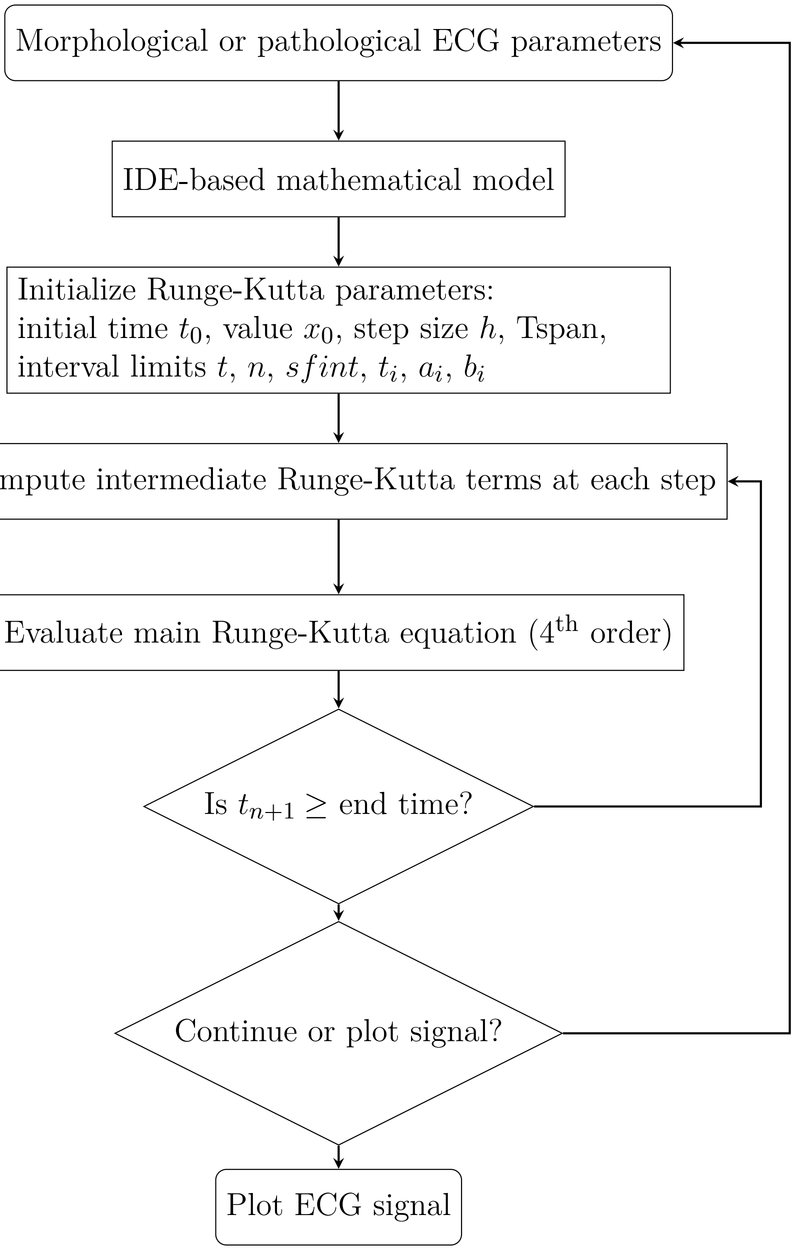

Figure 4.1: Flowchart for ECG signal generation using the 4th-order Runge-Kutta method.

4.2.1 Results and discussion

4.2.1.1 Results

To solve equation 4.2, the fourth-order Runge–Kutta technique is employed with a fixed step size of $\Delta t = \frac{1}{f_s} = 0.0039\,\mathrm{s}$ and an initial condition of $\mathbf{x}_0 = [1, 0, 0.04]$.

We utilized healthy and unhealthy ECG signals to assess our model's capacity to produce realistic synthetic ECG signals from the MIT database [107]. We compared the signals generated by our model with those acquired from the MIT database.
Consequently, visual analysis is employed to propose appropriate values for the parameters of our mathematical model for each type of arrhythmia.Figures 4.2, 4.3, and 4.4 illustrates the standard ECG signal produced by our model. Figure 2. b illustrates the standard ECG signal obtained from the MIT database [107].Tables 4.1–4.8 delineate the discrepancies between the model constructed with parameter values and those derived from the MIT-BIH database.

Table 4.1: Parameter values of the proposed model for generating a sinus bradycardia ECG signal.

Index (i)	**P**	**Q**	**R**	**S**	**T**
Time (s)	-0.2	-0.05	0	0.05	0.3
θ_i	$-\frac{\pi}{3}$	$-\frac{\pi}{12}$	0	$\frac{\pi}{12}$	$\frac{\pi}{2}$
a_i	1.2	-5.0	30.0	-7.5	0.75
b_i	0.25	0.1	0.1	0.1	0.4
w			$\boldsymbol{\frac{15\pi}{10}}$		

Table 4.2: Parameter values of the proposed model for generating a junctional bradycardia ECG signal.

Index (i)	**P**	**Q**	**R**	**S**	**T**
Time (s)	-0.2	-0.05	0	0.05	0.3
θ_i	$-\boldsymbol{\frac{4\pi}{5}}$	$-\frac{\pi}{12}$	0	$\frac{\pi}{12}$	$\frac{\pi}{2}$
a_i	1.2	1.0	30.0	-7.5	0.75
b_i	0.25	0.1	0.1	0.1	0.4
w			$\boldsymbol{\frac{4\pi}{3}}$		

4.2.1.2 Discussion

In all examined scenarios, we note that the proposed model facilitates the generation of high-quality ECGs for cardiac arrhythmias that closely resemble those sourced from

Table 4.3: Parameter values for the proposed model to generate a tachycardia ECG signal.

Index (i)	**P**	**Q**	**R**	**S**	**T**
Time (secs)	-0.2	-0.05	0	0.05	0.3
θ_i	$-\frac{\pi}{3}$	$-\frac{\pi}{12}$	0	$\frac{\pi}{12}$	$\frac{\pi}{2}$
a_i	1.2	1.0	30.0	-7.5	0.75
b_i	0.25	0.1	0.1	0.1	0.4
w			$\boldsymbol{4\pi}$		

Table 4.4: parameters values for the proposed model for producing flutter ECG signal.

Index (i)	**P**	**Q**	**R**	**S**	**T**
Time (secs)	1.2	**1**	**-10**	**-7.5**	**0.075**
θ_i	$-\frac{\pi}{3}$	$-\frac{\pi}{12}$	0	$\frac{\pi}{12}$	$\frac{\pi}{2}$
a_i	**5.0**	**15.0**	30.0	**15**	**5.0**
b_i	0.25	0.1	0.1	0.1	0.4

Table 4.5: parameters values for the proposed model for producing atrial extrasystole ECG signal.

Index (i)	**P**	**Q**	**R**	**S**	**T**
Time (secs)	-0.2	-0.05	0	0.05	0.3
θ_i	$-\frac{3\pi}{4}$	$-\frac{\pi}{12}$	0	$\frac{\pi}{12}$	$\frac{\pi}{2}$
a_i	**-1.2**	-5.0	30.0	-7.5	0.75
b_i	0.25	0.1	0.1	0.1	0.4

Table 4.6: parameters values for the proposed model for producing ventricular extrasystole ECG signal.

Index (i)	**P**	**Q**	**R**	**S**	**T**
Time (secs)	-0.2	-0.05	0	0.05	0.3
θ_i	$-\frac{\pi}{4}$	$-\frac{\pi}{12}$	0	$\frac{\pi}{12}$	$\frac{\pi}{2}$
a_i	**0.5**	**1.0**	**-30.0**	**0.2**	**1**
b_i	0.25	0.1	0.1	0.1	0.4

Table 4.7: parameters values for the proposed model for producing left branch ECG signal.

Index (i)	**P**	**Q**	**R**	**S**	**T**
Time (secs)	-0.2	-0.05	0	0.05	0.3
θ_i	$-\frac{\pi}{3}$	$-\frac{\pi}{12}$	0	$\frac{\pi}{12}$	$\frac{\pi}{2}$
a_i	**-1.2**	**0.0**	**-30.0**	-7.5	0.75
b_i	0.25	0.1	0.1	0.1	0.4

Table 4.8: Parameters values for the proposed model for producing right branch ECG signal.

Index (i)	**P**	**Q**	**R**	**S**	**T**
Time (secs)	-0.2	-0.05	0	0.05	0.3
θ_i	$-\frac{\pi}{3}$	$-\frac{\pi}{12}$	0	$\boldsymbol{-0.4\pi}$	$\boldsymbol{0.4\pi}$
a_i	1.2	-5.0	30.0	0	**-0.3**
b_i	0.25	0.1	0.1	0.1	0.4

the MIT database by employing appropriate parameters. For instance, in figure 4.2b, our model facilitates the development of sinus bradycardia with a heart rate below 50 bpm. However, in figure 4.3a, the model may produce sinus tachycardia with a heart rate exceeding 100 bpm. In figure 4.3a, we can regulate the presence or absence of the P wave or the superimposed P wave in conjunction with the QRS complex (junctional bradycardia).Figure 4.3b illustrates the flutter ECG signal when the frequency exceeds or exceeds 300 BPM ($\mathbf{w} > 10\pi$). The suggested model produces atrial extrasystole, depicted in 4.3c, where a negative P-wave is formed. Figure4.4a illustrates ventricular extrasystole, whereas figure4.4b and figure4.4c depicts the left bundle branch block and Right bundle branch block.

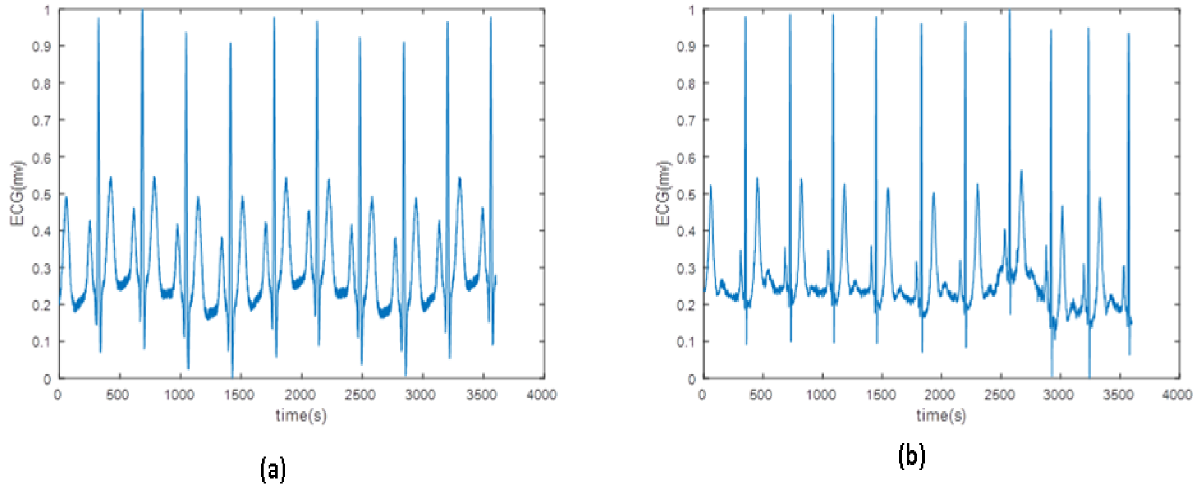

(a) Normal ECG

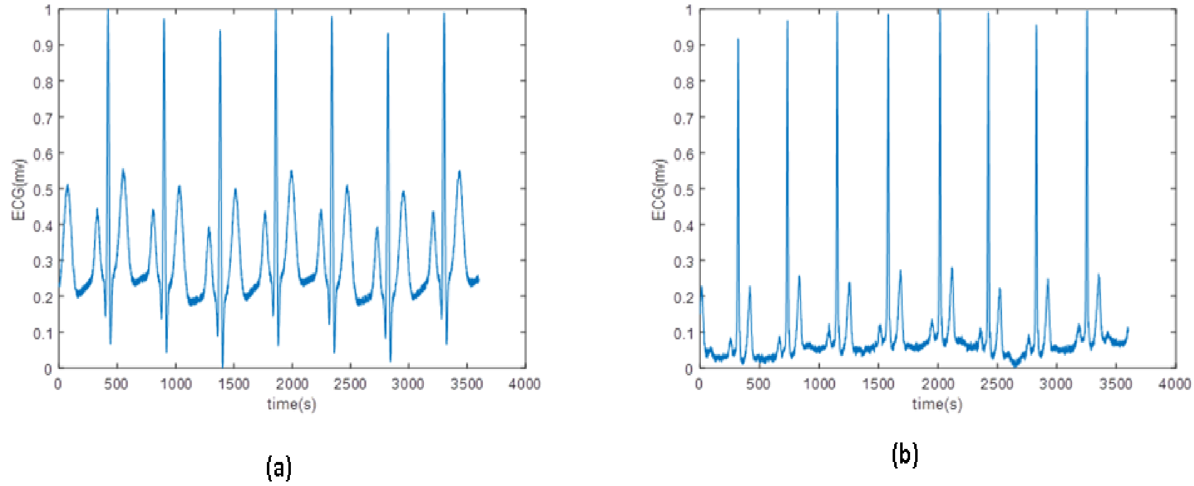

(b) Sinus Bradycardia

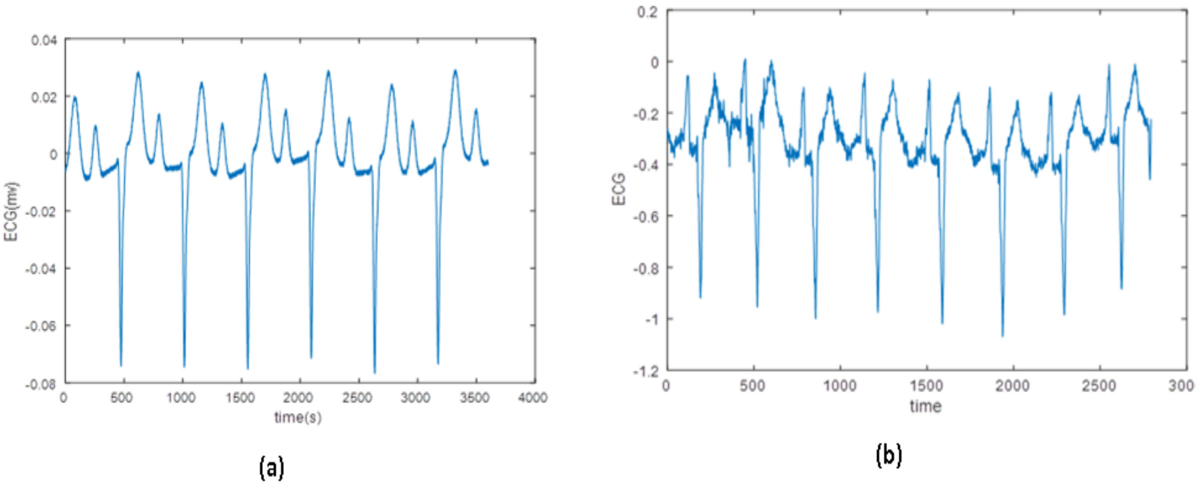

(c) Junctional Bradycardia

Figure 4.2: Comparison between synthetic and real ECG signals . Each subfigure shows: (a) a synthetic ECG signal generated by our model, and (b) a real ECG signal from the MIT-BIH database [5].

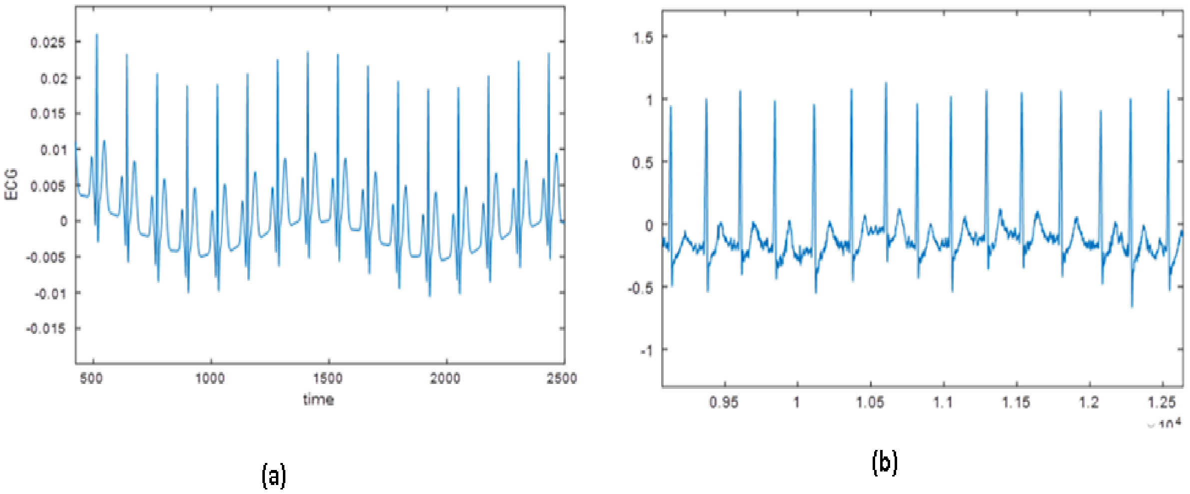

(a) Tachycardia

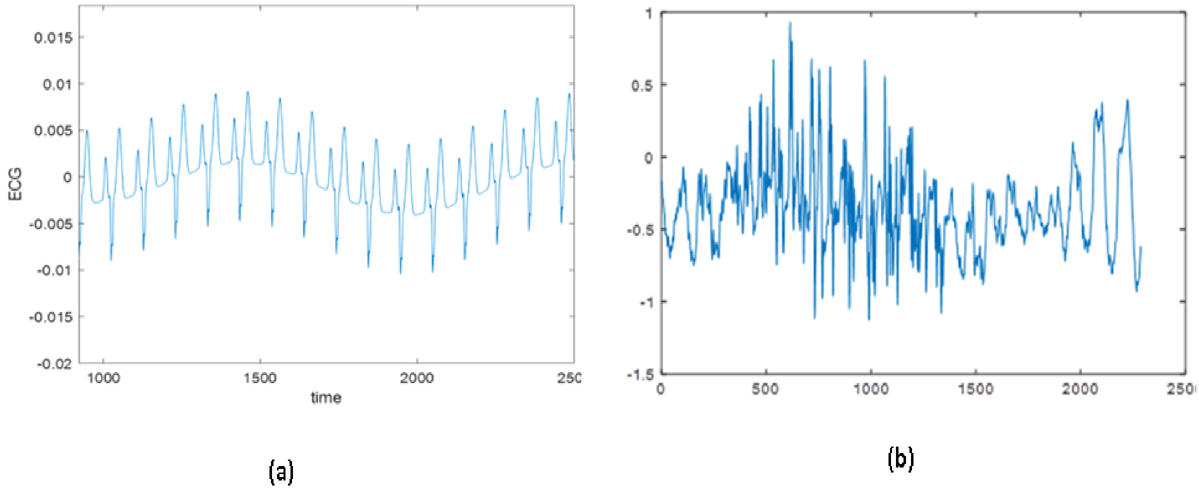

(b) Flutter

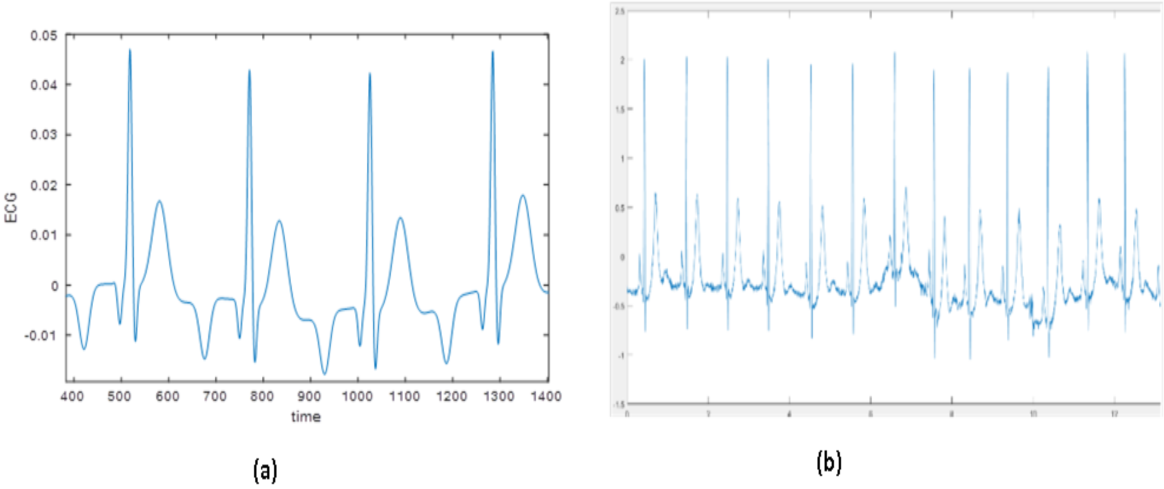

(c) Atrial Extrasystole

Figure 4.3: Comparison between synthetic and real ECG signals. Each subfigure shows: (a) a synthetic ECG signal generated by our model, and (b) a real ECG signal from the MIT-BIH database [5].

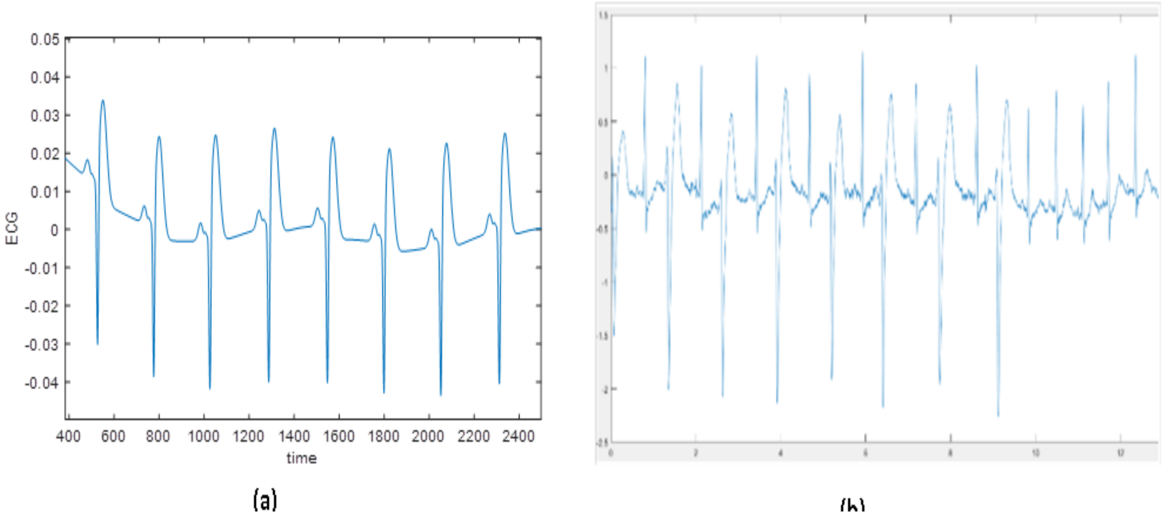

(a) Ventricular Extrasystole

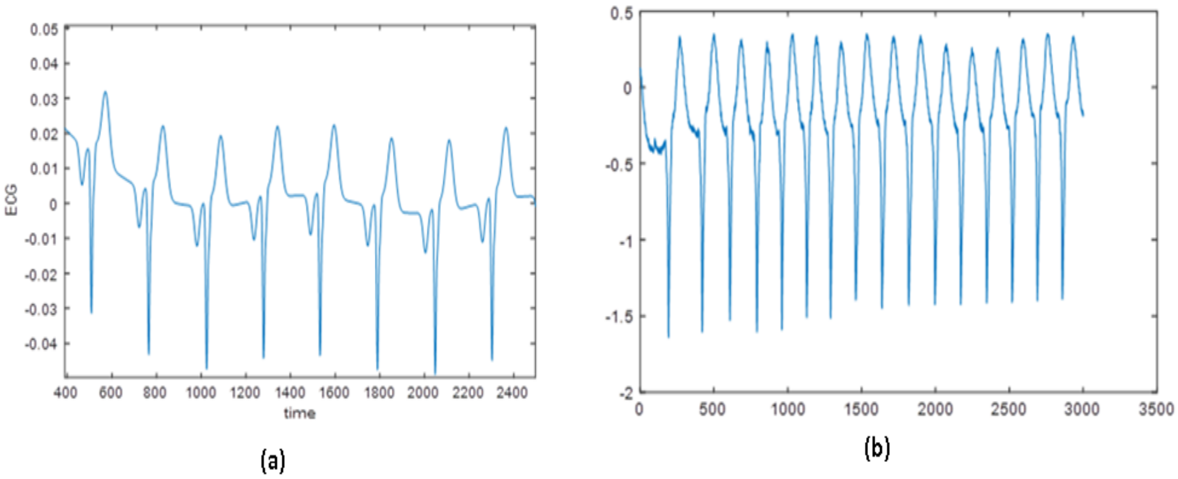

(b) Left Branch Block

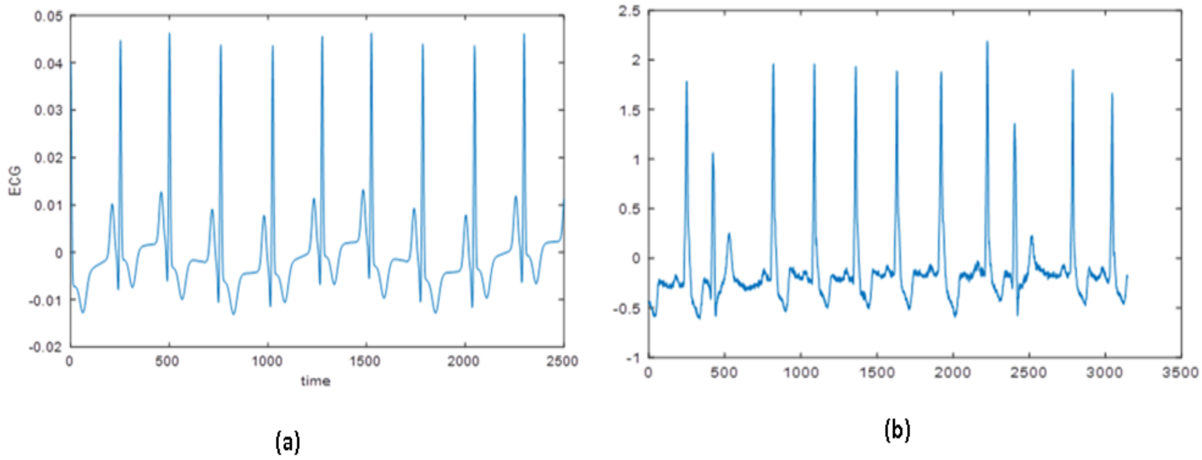

(c) Right Branch Block

Figure 4.4: Comparison between synthetic and real ECG signals . Each subfigure shows: (a) a synthetic ECG signal generated by our model, and (b) a real ECG signal from the MIT-BIH database [5].

The integration of Hopf bifurcation into the first two equations of the McSharry model introduces a significant enhancement to the dynamic behavior of the ECG generator. By promoting autonomous oscillatory behavior, this modification increases the physiological plausibility of the synthetic ECG signals, particularly in capturing the inherent rhythm of cardiac cycles. However, while the model succeeds in generating more realistic trajectories, its reliance on integer-order dynamics constrains its ability to reflect long-term memory effects and subtle signal variations present in real ECG data. These limitations emphasize the need for more flexible mathematical tools, such as fractional derivatives, to further improve the model's fidelity—setting the stage for the developments presented in the next chapter.

4.3 Optimization of Parameters of coupled ordinary differential equations for ECG Signal Generation using Grey Wolf Optimizer

Estimating parameters for ECG signal generation is complex due to several factors. The dynamic nature of cardiac electrical activity requires precise characterization of various physiological parameters, such as heart rate, waveform amplitude, and duration. Furthermore, individual variations in anatomy and physiology introduce additional challenges, as these parameters can differ significantly between patients. Noise and artifacts in actual ECG recordings often obscure the underlying signals, complicating the identification of accurate patterns. Additionally, the non-linear interactions within the cardiac electrical system further increase the complexity, requiring advanced modelling techniques. To overcome these challenges, effective optimization strategies and innovative parameter estimation methods are essential for generating clinically relevant ECG signals. Several studies have investigated optimization approaches for parameter estimation in ECG signal production [108–111]. This research seeks to improve the generation of ECG signals by optimizing the parameters of coupled ordinary differential equations (IDEs) and exploring phenomena like Hopf bifurcation. The focus is on enhancing the accuracy of synthetic ECG waveforms that reflect clinical observations. The GWO, a metaheuristic optimization technique inspired by grey wolves' hierarchical social structure and hunting behaviour, addresses this challenge. The GWO is particularly adept at navigating complex, multidimensional parameter spaces, allowing for effective alignment of simulated ECG signals with actual clinical data. Optimizing the coefficients in the coupled IDEs improves the fidelity of the generated signals, enabling them to capture both normal and arrhythmic cardiac behaviours. The study utilizes GWO to optimize the coefficients governing heart dynamics, aiming to align the simulated ECG waveforms with clinically observed data accurately. Ultimately, the goal is to enhance the reliability of ECG signal simulations, improving their utility in medical research and clinical applications.

4.3.1 Method

4.3.1.1 Model of McSharry et al. by using a novel Hopf bifurcation

The McSharry model for ECG generation [24] thoroughly depicts cardiac dynamics, integrating critical physiological elements that affect ECG waveforms. In our prior publication, [5], we altered the McSharry model by incorporating a fresh Hopf bifurcation in the initial two equations, thus establishing a new model for generating synthetic ECG signals. We employed the Hopf bifurcation in the initial two equations to produce a limit cycle with periodic orbits, commonly known as "self-oscillations," originating from a stable fixed point. The proposed model is defined in Equation (4.2).

4.3.1.2 Implicit rectangular method to solve the IDE

The implicit rectangle approach is a commonly employed integration technique for integer differential equations. This study uses it to numerically solve equation 4.4.

Implicit rectangular formula:

$$x_n = T_{m-1}[x,t_0](t_n) + h^{\alpha}(\tilde{a}_n^{(\alpha)} g(t_0,x_0) \sum_{j=0}^{n-1} a_{n-1}^{(\alpha)} g(t_j,x_j)) \tag{4.10}$$

$$\tilde{a}_n^{(\alpha)} = \frac{(n-1)^{\alpha+1} - n^{\alpha}(n-\alpha-1)}{\Gamma(\alpha+2)}, \quad a_n^{(\alpha)} = \begin{cases} \frac{1}{\Gamma(\alpha+2)} & n=0 \\ \frac{(n-1)^{\alpha+1} - 2n^{\alpha+1} + (n+1)^{\alpha+1}}{\Gamma(\alpha+2)} & n=1,2,\ldots \end{cases}$$

with $x_n = T_{m-1}[x, t_0](t_n)$ is the Taylor polynomial of degree m-1 for the function x(t) centered at t0 ,that is: $T_{m-1}[x;t_0](t) = \sum_{k=0}^{m-1} \frac{(t-t_0)^k}{k!} y^{(k)}(t_0)$

4.3.1.3 Estimating and Optimizing Model Parameters with the GWO

The GWO is a nature-inspired optimization algorithm based on grey wolves' social structure and hunting behaviors in their natural habitat. Formulated by Mirjalili et al.[99], GWO is a heuristic method for addressing intricate optimization challenges.
The GWO algorithm emulates grey wolves' social interactions and hunting techniques. It is categorized into alpha, beta, delta, and omega, which rank from highest to lowest within the pack. The method functions in a population-based framework, with each wolf symbolizing a potential solution to the optimization problem.
The GWO algorithm advances over iterations; each termed a "hunt." During each hunt, the alpha, beta, and delta wolves direct the remainder of the pack toward potential ideal solutions. This guidance is accomplished by a series of mathematical calculations that modify the position of each wolf inside the search space.
GWO employs three fundamental formulas for position updates:

- Adjusting the location of the alpha wolf, which affects the entire pack.
- Modifying the roles of the beta and delta wolves, which direct a pack segment
- Modifying the locations of the omega wolves, which investigates the search space more comprehensively

Factors like the exploration rate, alpha, beta, and delta coefficients, and the current iteration count determine the location updates. The method seeks to enhance solution quality progressively through successive iterations.
The unknown characteristics of the ECG signal in our study are ascertained by minimizing the error function delineated in 4.11. The ECG data denotes the sampled ECG signal obtained from a continuous ECG signal recorded in a clinical environment with unspecified parameters. In contrast, the ECG generated refers to the signal produced by simulating equation 4.4. Both ECG data and ECG-generated signals are captured at the same frequency.

$$\text{Mean Absolute Error (MAE)} = \frac{1}{n}\sum_{i=1}^{n}\left|\text{ECG}_{\text{Data},i} - \text{ECG}_{\text{Generated},i}\right| \tag{4.11}$$

With n number of samples.

The GWO's fundamental objective is to investigate and ascertain the unknown parameters $(a_i, b_i, andj_i)$ to minimize the MAE value.
Figure 4.5 illustrates the flowchart representing the optimization of model parameters with the Grey Wolf Optimiser. The procedure comprises three primary stages:

- **Step 1** produces an initial fake ECG signal by configuring parameters for IDE systems, subsequently generating synthetic ECG signals by implicit rectangular methods for resolution.
- **Step 2** retrieves ECG recordings from the MIT-BIH Arrhythmia database.This entails normalizing each heartbeat in authentic and synthetic ECG signals to a range of 0 to 1, then implementing a filter on the ECG signal.
- **Step 3** utilizes the GWO to identify the optimal parameter configuration for the model. This entails initializing the GWO optimizer population, constructing the cost function with designated parameters, and executing the optimizer to identify the optimal parameter set that minimizes the MAE.

4.3.2 Results and discussion

We acquired both healthy and pathological ECG data from the MIT-BIH database to evaluate the model's ability to generate realistic synthetic ECG signals [107]. Specifically, we selected 150 ECG segments, including Normal Heart Beats (NHB), Right Bundle Branch Block Beats (RBBB), and Premature Ventricular Contractions (PVC), as detailed in Table 4.9.

As detailed in TABLE 4.10, the GWO method has been configured to employ 30 search agents, perform 500 iterations, and manage 15 variables. The variables include a1 to a5, b1 to b5, $\vartheta 1$ to $\vartheta 5$ parameters, each denoting distinct characteristics of the ECG signal,

Table 4.9: The records and the type of beat used to evaluate the method.

Record	**106**	**124**	**114**
Type of Beat	Normal Heart Beat (NHB)	Right Bundle Branch Block (RBBB)	Premature Ventricular Contraction (PVC)

including the P-wave (a1, b1), Q-wave (a2, b2), R-wave (a3, b3), S-wave (a4, ϑ4), and T-wave (a5, ϑ5).

Table 4.10: The Grey Wolf Optimizer (GWO) settings.

Set of parameters	**The number of variables**	**Number of wolves**	**Max iterations**
	15	30	100

The implicit rectangular approach is employed to solve equation 4.4 using the parameters listed in TABLE 4.11.

Table 4.11: Parameters of the Implicit Rectangular Method.

Set of Parameters	**Step Size**	**Tolerance**	**Max Iterations**	X_0 **(Initial Values)**
	0.00277	10^{-6}	100	[1; 0; 0.035]

The model produces synthetic normal heartbeats in its preliminary phase, as illustrated in Figure 4.6. This picture clearly illustrates the ECG signal generated by our model using the implicit rectangle technique, showcasing distinct PQRST waves.

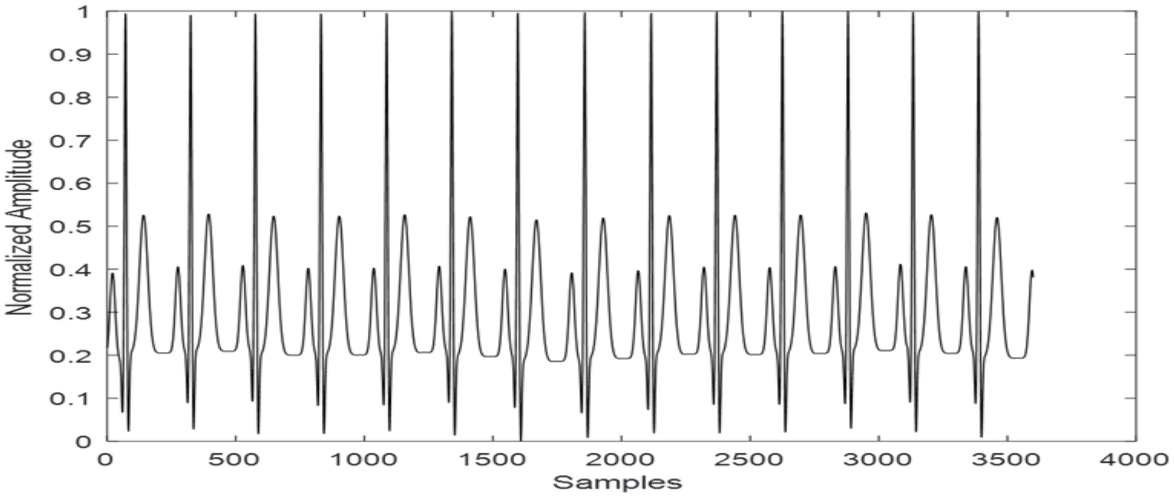

Figure 4.6: Normal ECG signal generated by our model[6].

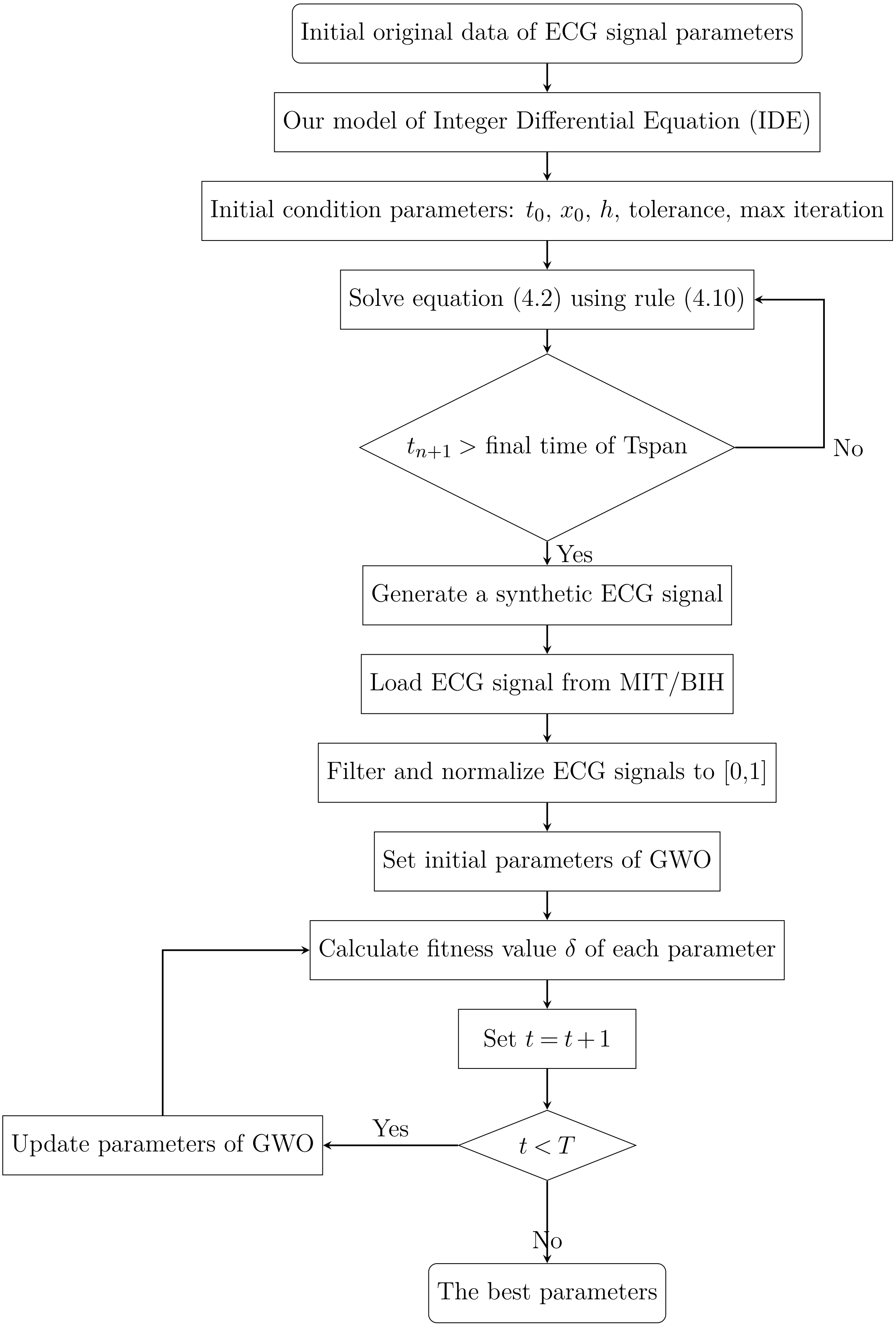

Figure 4.5: ECG synthetic (morphological and pathological) flow chart using the Grey Wolf Optimizer .

Employing the algorithm illustrated in the flowchart(figure 4.5) and the parameters specified in Tables 4.10 and 4.11, we obtain optimized parameters for each beat type, as detailed in Table 4.12.

Table 4.12 delineates a series of parameters (a1 to a5, b1 to b5, and $\vartheta1$ to $\vartheta5$) for three distinct categories of heartbeats: NHB, RBBB, and PVC. Each parameter is shown with its mean value and standard deviation, offering insight into the variability linked to the estimations.

For NHB, the mean value of a1 is 1.6592, with a standard deviation of ±0.3245, suggesting that the estimated value of a1 typically varies within this interval. Likewise, the other parameters (a2 to a5 and b1 to b5) are accompanied by their corresponding mean and standard deviation values.

In all examined instances, implementing the suggested algorithm utilizing the GWO for estimating ECG parameters has exhibited commendable performance, yielding a low error rate, as illustrated in figure 4.7.

Figure 4.7 depicts various heartbeat types obtained from the MIT database, the reconstructed signals produced by our model, and the corresponding errors.

In the scenario of NHB, the MAE was 0.0144, and MSE was 5.1620×10^{-4}. In the case of RBBB, we recorded a MAE of 0.0141 and a MSE of 3.7996×10^{-4}. For PVC, the MAE was 0.0223, and the MSE was 0.0011.

This achievement can be ascribed to the GWO's capacity to effectively explore and converge on optimal solutions inside intricate, non-linear parameter spaces. Utilizing the GWO's intrinsic capabilities, we successfully optimized the model parameters with exceptional precision, resulting in precise reconstructions of the ECG signal.

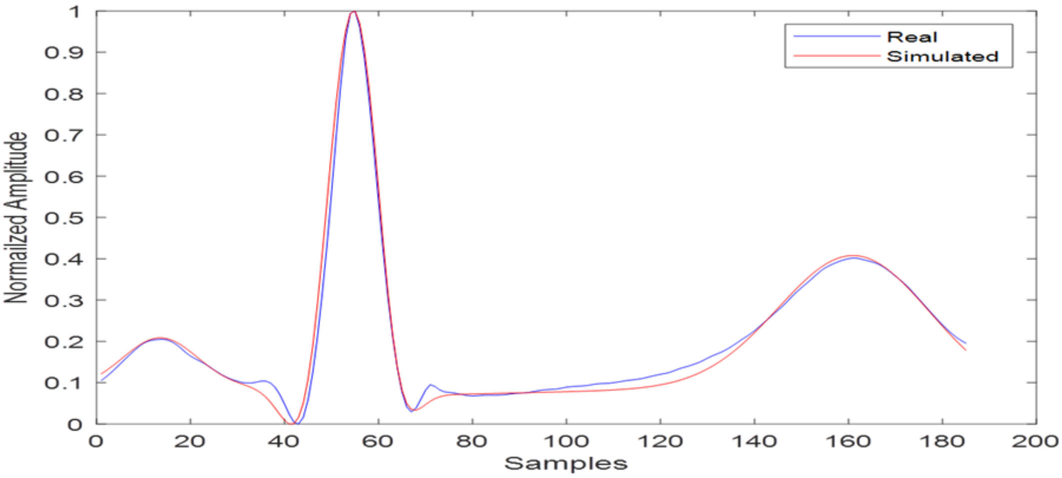

(a) NHB: MAE = 0.0144, MSE = 5.1620×10^{-4}.

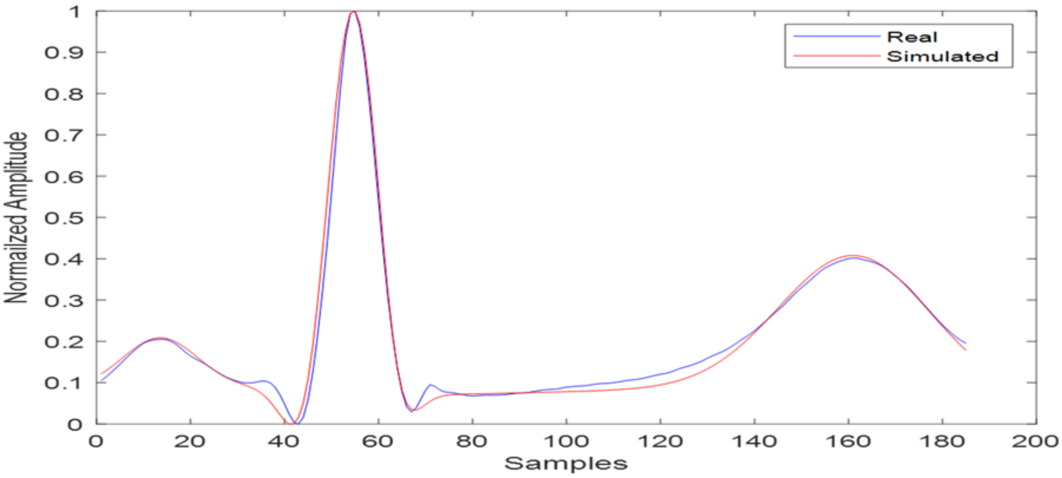

(b) RBBB: MAE = 0.0141, MSE = 3.7996×10^{-4}.

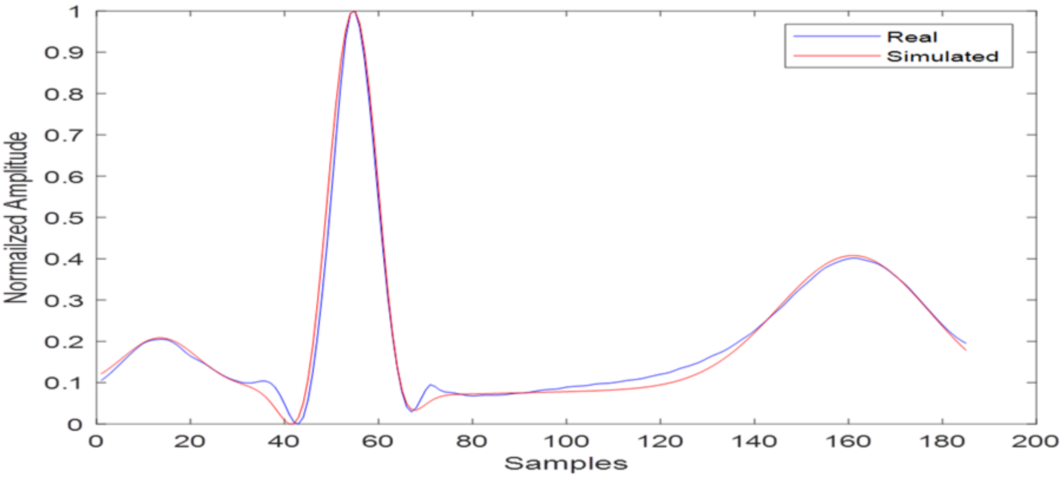

(c) PVC: MAE = 0.0223, MSE = 1.1×10^{-3}.

Figure 4.7: Displays various heartbeat types obtained from the MIT database, alongside their corresponding reconstructed signals generated by our model, as well as the respective errors[6].

Table 4.12: Summarizes the estimated parameters and their variances obtained by GWO.

	a_1	a_2	a_3	a_4	a_5	b_1	b_2	b_3	b_4	b_5	θ_1	θ_2	θ_3	θ_4	θ_5
106 NHB	1.6592±0.3245	-9.2990±0.1895	24.8497±6.2547	-10.7973±0.9984	1.1209±0.0251	0.1402±0.0018	0.0787±0.0154	0.1011±0.0055	0.0693±0.0035	0.2809±0.0081	39.8904±6.2514	-8.5430±0.5142	1.2021±0.0754	10.0331±1.2543	107.9949±20.5843
124 RBBB	0.0999±0.0325	4.3993±3.8791	15.2955±3.8791	-1.2914±0.7564	-2.2100±1.0233	0.3001±0.1253	0.0697±0.0985	0.1073±0.0325	0.0802±0.0105	0.2983±0.0983	57.9112±12.3546	-20.9872±3.5267	0.4948±0.0990	15.7166±3.5846	99.3844±16.2560
114 PVC	9.8701±1.2587	0.0993±0.0325	-11.7160±2.5849	0.0782±0.0198	0.9500±0.3120	0.0955±0.0186	0.0758±0.0754	0.1292±0.0177	0.0871±0.0201	0.3255±0.0754	-8.5979±2.310	-21.0574±2.2589	2.2999±0.4531	13.7408±2.3510	94.0185±10.3520

The use of the GWO to fine-tune the parameters of the IDE-based ECG model demonstrates a clear advancement in modeling accuracy and adaptability. By optimizing waveform features on a beat-by-beat basis, the approach enhances the alignment between synthetic and real signals across a range of cardiac morphologies. Despite this success, the method remains bound by the structural rigidity of integer-order differential equations, limiting its capacity to model the nuanced, memory-driven behaviors of the cardiovascular system. This observation reinforces the rationale for exploring fractional-order systems, which inherently capture such dynamics and are introduced as the primary focus of the following chapter.

4.4 Conclusion

This chapter has presented two complementary advancements in the modeling of ECG signals within the classical framework of integer-order differential equations. First, we introduced a modified version of the McSharry model, incorporating a Hopf bifurcation into the first two equations to generate realistic, self-sustained oscillatory dynamics. This approach improved the physiological relevance of the signal by better simulating the PQRST waveform and capturing rhythmic cardiac behavior, including arrhythmic conditions. The use of numerical solvers like the implicit rectangular method further enhanced the stability and accuracy of the simulation.

In the second part of the chapter, we applied an advanced parameter optimization strategy using the GWO. This bio-inspired algorithm effectively explored the complex parameter space of the IDE-based model, enabling the generation of ECG signals that align closely with real clinical data across various pathological and morphological patterns. The optimization not only enhanced the modeling accuracy but also demonstrated the model's adaptability when fitted on a beat-by-beat basis, a crucial requirement in computational cardiology and ECG-based diagnostics.

Despite these notable improvements, both contributions revealed intrinsic limitations of integer-order systems, particularly in their inability to capture long-range dependencies, memory effects, and fine-grained signal irregularities often seen in real physiological data. These limitations are not merely technical but stem from the foundational nature of integer-order calculus, which assumes local interactions and lacks the flexibility to model systems with memory or hereditary properties.

Consequently, the developments in this chapter serve a dual purpose: they establish the strength of classical IDE-based approaches in providing interpretable and stable ECG models, while also exposing the boundaries of their applicability in high-fidelity biomedical signal modeling. These insights strongly justify the transition to FDEs, which inherently accommodate memory effects and offer greater flexibility in tuning signal dynamics. Chapter 5 will build upon the groundwork laid here, introducing a novel ECG modeling framework based on fractional calculus to further improve accuracy, generalizability, and physiological realism in synthetic signal generation.

Chapter 5

ECG Modeling Using Fractional Differential Equations (FDEs)

5.1 Introduction

The preceding chapter explored two enhanced models based on classical IDEs, demonstrating notable improvements in ECG signal generation through structural modification and parameter optimization. However, these models remain fundamentally limited in their capacity to capture memory-dependent dynamics and the complex temporal variability observed in real ECG signals. Such limitations are inherent to the local nature of integer-order systems.

To overcome these constraints, this chapter introduces an extended modeling framework based on FDEs. The proposed approach selectively integrates fractional derivatives into the McSharry model—specifically within the equation responsible for generating the PQRST waveform—while preserving the limit cycle behavior of the original integer-order system. This hybrid structure maintains physiological consistency while significantly enhancing modeling flexibility and accuracy.

In this work, the numerical solution of the FDE-based model is carried out using the Predictor-Corrector (PC) method. Parameter estimation is performed via GA optimization to ensure close alignment between simulated and real ECG data. The model is evaluated across a diverse set of heartbeats from the MIT/BIH Arrhythmia Database. This chapter aims to:

1. Implement and validate a fractional-order extension of the McSharry model.
2. Analyze the influence of the fractional derivative on the generated ECG morphology.
3. Assess the modeling quality and compression performance of the proposed FDE model.
4. Compare the results with those of the optimized IDE-based models .

By building upon the foundation established in previous chapters, this work demonstrates the added value of fractional modeling in capturing the nuanced dynamics of cardiac activity. The findings confirm that the FDE approach provides a more precise and adaptable framework for synthetic ECG generation, with implications for improved diagnostics, simulation, and compression in biomedical signal processing.

5.2 Dynamical Model for the Generation of Synthetic ECG Signals

5.2.1 Fractional Order McSharry Model

Inspired by the McSharry model, we propose to extend this model by substituting the integer order in each equation's derivative in equation (3.1) with a fractional order α, where $0 < \alpha < 1$.

Equation 5.1 describes the new model, where $D_{t_0}^{\alpha_i}$ is the fractional differentiator operator for $i = 1,2,3$, and $0 < \alpha_i < 1$ are real positive numbers.

$$\begin{cases} D_{t_0}^{\alpha_1} x_1(t) &= \alpha x_1 - w x_2. \\ D_{t_0}^{\alpha_2} x_2(t) &= \alpha x_2 + w x_1. \\ D_{t_0}^{\alpha_3} x_3(t) &= \sum_{i\in\{P,Q,R,S,T\}} a_i \Delta\theta_i \exp\left(-\frac{\Delta\theta_i^2}{2b_i^2}\right) - (x_3 - z_0). \end{cases} \tag{5.1}$$

Formula 5.2 can be obtained by rewriting each equation in the system 5.1 using Volterra Integral Equations (VIES). This transformation offers a solution to the system delineated in :

$$\begin{cases} x_1(t_n) &= x_1(t_0) + \frac{1}{\Gamma(\alpha_1)} \int_{t_0}^{t} (t-\tau)^{\alpha_1 - 1} (\alpha_1 x_1 - w x_2) \\ x_2(t_n) &= x_2(t_0) + \frac{1}{\Gamma(\alpha_2)} \int_{t_0}^{t} (t-\tau)^{\alpha_2 - 1} (\alpha_2 x_2 + w x_1). \\ x_3(t_n) &= x_3(t_0) + \sum_{i\in\{P,Q,R,S,T\}} a_i \Delta\theta_i \exp\left(-\frac{\Delta\theta_i^2}{2b_i^2}\right) - (x_3 - z_0). \end{cases} \tag{5.2}$$

While equations 5.1 and 5.2 accurately depict a fractional model technically, the transformation of the initial two equations of McSharry's model into fractional differential equations is devoid of physical relevance. These equations illustrate a point moving over a unit circle, whereas their fractional equivalents fail to adhere to this physical understanding.

To resolve this issue, we suggest that the fractional order be applied exclusively to the third equation, which generates the PQRST waveform, while the integer order in the first two equations is maintained. This method preserves the connection between the first two derivative equations in the integer-order dynamical model and the RR interval.

The first two equations can be simplified by presuming that the fractional orders α_1 and α_2 are sufficiently close to 1 (i.e., $\alpha_1 = \alpha_2 \approx 1$. To preserve their original physical meaning, terms that involve $\Gamma(1)$ and $(t_n - \tau)^0$ are substituted. The following equation is obtained as a result of this simplification: $\Gamma(1) = 1$ and $(t_n - \tau)^0 = 1$ [7].

$$\begin{cases} x_1(t_n) & = x_1(t_0) + \int_{t_0}^{t} (\alpha_1 x_1 - w x_2)\,\mathrm{d}\tau \\ x_2(t_n) & = x_2(t_0) + \int_{t_0}^{t} (\alpha_2 x_2 + w x_1)\,\mathrm{d}\tau \\ x_3(t_n) & = x_3(t_0) + \frac{1}{\Gamma(\alpha_3)} \int_{t_0}^{t_n} (t_n - \tau)^{\alpha_3 - 1} \left(\sum_{i \in \{P,Q,R,S,T\}} a_i \dot{\Delta\theta}_i \exp\left(-\frac{\Delta\theta_i^2}{2b_i^2} \right) - (x_3 - z_0) \right) \mathrm{d}\tau \end{cases} \tag{5.3}$$

With $0 < \alpha_3 < 1$

To resolve the system outlined in 5.3 and produce the synthetic ECG, we employed the PC approach specified by Eq. (2.113). In the subsequent content, we will employ the annotations IDE and FDE to refer to the McSharry and fractional models, respectively.

5.3 Simulation results

The initial stage involves examining the impact of integrating the fractional derivative into the third equation of the IDE model, as delineated in equation 5.3, to assess the efficacy of the suggested modeling technique in generating ECG-like waveforms. Consequently, we initiated our approach by employing parameters identical to those of the IDE model, except for incorporating fractional differentiation into the third equation. The specifications of the new model are enumerated in table 5.1

Table 5.1: Establish parameters for the FDE model.

Index (i)	**P**	**Q**	**R**	**S**	**T**
Time (secs)	-0.2	-0.05	0	0.05	0.3
$\theta_i(radians)$	$-\frac{\pi}{3}$	$-\frac{\pi}{12}$	0	$\frac{\pi}{12}$	$\frac{\pi}{2}$
a_i	1.2	-5.0	30.0	-7.5	0.75
b_i	0.25	0.1	0.1	0.1	0.4
Alpha(α)			$[\alpha] \in [0.1, 0.99]$		

5.3.1 Evaluation of Numerical Techniques for Addressing Fractional Differential Equations in ECG Beat Simulation

Among the numerical strategies evaluated for solving FDEs in the modeling of ECG beats, the PC method was selected due to its balanced combination of the advantages offered by both explicit and implicit schemes, while mitigating their respective drawbacks. Table 5.2 summarizes the comparative results obtained from four methods: PI Explicit Rectangular, PI Implicit Trapezoidal, PI Implicit Rectangular, and PI Predictor-Corrector.

Table 5.2: Execution Times (in Seconds), Error, and EOC for Solving Fractional Differential Equations for Modeling Normal Heartbeats with ECG Size = 185 at Time $T = 10$, Step-Size $h = 0.00277$, and Number of ECG Beats = 100.

Type of Beat	**PI Predictor-Corrector**			**PI Implicit Trapezoidal**			**PI Implicit Rectangular**			**PI Explicit Rectangular**		
	EOC	**Times**	**MSE** ($\times 10^{-4}$)	**EOC**	**Times**	**MSE** ($\times 10^{-4}$)	**EOC**	**Times**	**MSE** ($\times 10^{-4}$)	**EOC**	**Times**	**MSE** ($\times 10^{-4}$)
NHB (185)	0.2561	40.6575	3.6029	0.2547	46.0705	3.5612	0.3393	47.1166	6.4122	0.3194	35.0562	5.7280
JHB (145)	0.1847	41.8134	2.4656	0.1849	48.0676	2.4637	0.2422	51.7048	4.1933	0.2546	33.3974	4.5534
RBBB (235)	0.2874	44.5919	3.6165	0.2885	50.4163	3.6480	0.3120	50.6119	4.2634	0.3588	42.5907	5.7102
LBBB (236)	0.2904	43.8975	3.7563	0.2882	48.9701	3.7018	0.3374	49.9086	5.0391	0.2836	32.8772	3.5592
PVC (183)	0.5233	42.4403	0.0010	0.5080	47.4339	0.0011	0.8760	49.6288	0.0013	0.7045	32.3130	0.0020

The table compares four methods for solving FDEs used in modeling different ECG beats. It evaluates their performance based on execution time, MSE, and estimated order of convergence (EOC):

1. **Execution Time:** The PI Explicit rectangular method is consistently the fastest across all types of ECG beats, with times ranging from 32.3130 to 42.5907 seconds.
2. **Mean Squared Error (MSE):** The PI Implicit trapezoidal method shows lower MSE values (scaled by 10^{-4}) across all beat types, indicating higher accuracy compared to other methods.
3. **Estimated Order of Convergence (EOC):** Similarly, the PI Implicit trapezoidal

method demonstrates lower EOC values, suggesting better convergence rates for the ECG beat models analyzed.

We found:

- **Fastest Method:** PI Explicit rectangular method.
- **Most Accurate Method:** PI Implicit trapezoidal method, offering lower MSE and EOC values.
- **Balanced Choice:** PI predictor-corrector method provides a good balance between accuracy (low MSE) and computational efficiency, making it suitable for modeling normal heartbeats.

The PC method was selected to solve the FDEs governing our ECG model due to its proven ability to balance computational efficiency, numerical stability, and solution accuracy—critical requirements for modeling non-stationary biomedical signals. Unlike classical integer-order differential equations, FDEs inherently involve memory effects and non-local operators, which necessitate methods capable of handling the integral history of the system. The PC approach addresses these challenges through a two-step iterative process:

1. **Computational Efficiency**:

   By reusing prior step evaluations and approximating fractional derivatives iteratively, the method avoids the exponential computational cost of recalculating the entire history at each time step. This is particularly advantageous for long-duration ECG simulations, where traditional methods like the GL approximation become prohibitively expensive.

2. **Numerical Stability:** The corrector step refines the initial predictor estimate, mitigating error propagation and ensuring stability even for stiff systems. This is essential for modeling pathological ECG signals, where abrupt

The solution of the FDEs outlined in equation (5.2) functions similarly to the IDEs in generating ECG waves. The PC method was employed to solve the FDEs, utilizing the parameters specified in 5.3.

Table 5.3: Parameters of the Predictor-Corrector Method.

Set of Parameters	α	**h**	**Tol**	**Mu**	**Itmax**	**mu_tol**	X_0
	[0.1, 0.99]	2^{-10}	10^{-6}	1	100	10^{-6}	[1; 0; 0.04]

Where,

- *alpha*(α) denotes the order of the fractional derivative, with $\alpha \in [0.1, 0.99]$.
- The variable h represents the step size employed in the integration process.
- Tol is a specified tolerance value used to ascertain the termination of the Newton-Raphson iterations in internal nonlinear equations.
- Itmax specifies the upper limit on the number of iterations permitted in the Newton-Raphson method. μ denotes the number of corrector iterations.
- mu tol denotes the tolerance value utilized to assess the convergence of corrector iterations as mu approaches infinity.
- X_0 denotes the matrix of initial conditions.

Figure (5.1) illustrates the ECG produced by the FDEs model for fractional order α values of 0.6, 0.7, 0.80, and 0.9, respectively.
No change in the RR interval is observed, irrespective of the fractional order α value. Figure 5.1 illustrates that the amplitudes of the various components of the generated ECG signal (PQRST waves) diminish as the fractional order α increases. This observation holds even though the parameter values governing the amplitudes of the different components in the initial model remain constant, resulting in an overall change in amplitude.

Utilizing this amplitude change may enhance the model's flexibility. This method offers an effective means to regulate various waveforms as required.

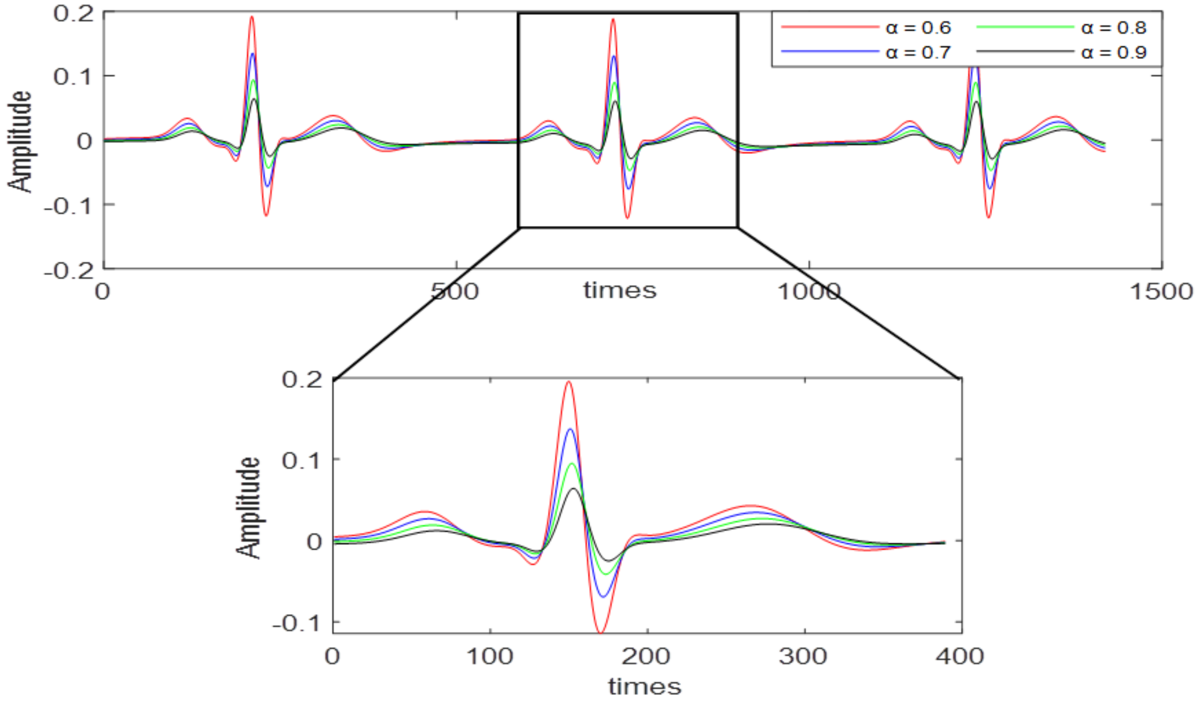

Figure 5.1: ECG Signal Synthesized with the Fractional Differential Equation Model.[7]

Our findings demonstrate that incorporating the fractional derivative in the third equation of the IDE model affects the amplitude of the produced ECG. The next step entails assessing the efficacy of the FDE model relative to the IDE models, concentrating on modelling quality and compression score. The subsequent stages will be executed to attain this objective: An optimization technique will be utilized to determine the ideal parameter set for both models. Thereafter, the obtained signal will be rebuilt, and multiple distortion metrics will be computed to evaluate the modelling quality of the two models. We will assess and contrast the Compression Ratio (CR), Percentage Root Mean Square Difference (PRD), and Quality Score (QS) of the two models. We utilized a dataset including five hundred ECG beats from the MIT/BIH Arrhythmia database [112]. We picked five unique entries from the database, each representing a separate cardiac condition: NHB,JHB, LBBB, RBBB, and PVC. We extracted a slice from each record comprising the initial one hundred consecutive beats. The study included 500 beats, with 100 beats assigned to each condition, as detailed in table 5.4.

The actual ECG signal underwent smoothing through a Savitzky-Golay filter, characterized by a frame length corresponding to the length of the ECG beats segment, an

Table 5.4: The records and the type of beat used to evaluate the method.

Record	**106**	**234**	**207**	**124**	**208**
Type of Beat	Normal Heart Beat (NHB)	Junctional Heart Beat (JHB)	Left Bundle Branch Block (LBBB)	Right Bundle Branch Block (RBBB)	Premature Ventricular Contraction (PVC)

order of 3, and a frame size of 20 [113, 114].

5.3.2 Estimation and optimisation of model parameters with GA

Diverse optimization techniques can be employed to determine the ECG signal's actual parameters and address the optimization challenge specified by equation (5.3). Genetic Algorithms were chosen for parameter estimation in both models because of their straightforward implementation in MATLAB. The unidentified parameters of the simulated ECG are computed to minimize the cost function delineated in equation (4.11) .

$$MSE = \frac{1}{N}\sum_{i=1}^{n}\left(ECG_{\text{real}} - ECG_{\text{simulated}}\right)^2 \tag{5.4}$$

The ECG_{real} signifies the authentic ECG signal, whereas $\text{ECG}_{\text{simulated}}$ indicates the intended simulated signal, with N denoting the total number of samples per ECG beat. Estimating and optimizing model parameters with a Genetic Algorithm comprises three primary processes, each succinctly outlined below and depicted in Figure 5.2.

Step 1: Preprocessing of the real ECG signal involves the following sub-steps:

- Load the real ECG segment from the MIT/BIH record.
- Filter the real ECG using the Savitzky-Golay filter.
- Extract individual heartbeats using the onset and offset from the annotation file.
- Normalize the actual ECG between 0 and 1.

Step 2: Generate and preprocess the synthetic ECG beat

- Establish the Fractional Differential Equations (FDEs) utilizing the initial parameter values a_i, b_i, θ_i, and α_i, together with the RR information detailed in Table 5.1.
- Utilize the Predictor-Corrector approach to resolve the FDE and generate a synthetic ECG signal.
- Standardize the synthetic ECG signal to a range of 0 to 1.
- Compute the MSE cost function with the actual ECG and the synthetic ECG. Construct the cost function (MSE in equation (5.4)) utilizing the parameters specified for optimization (a_i, b_i, θ_i, and α_i).

Step 3: Optimization of FDE Model Parameters by Genetic Algorithm (GA)

This phase uses a GA to identify the ideal parameter set for the FDE model. The procedure comprises the subsequent sub-steps:

- Establish the settings for the GA population.
- Generate the initial population.
- Enhance FDE Parameters via GA-Based Optimization: Apply a GA to minimize the MSE and determine the optimal set of parameters—namely a_i, b_i, θ_i, and the fractional orders α_i—that best fit the target ECG signal.

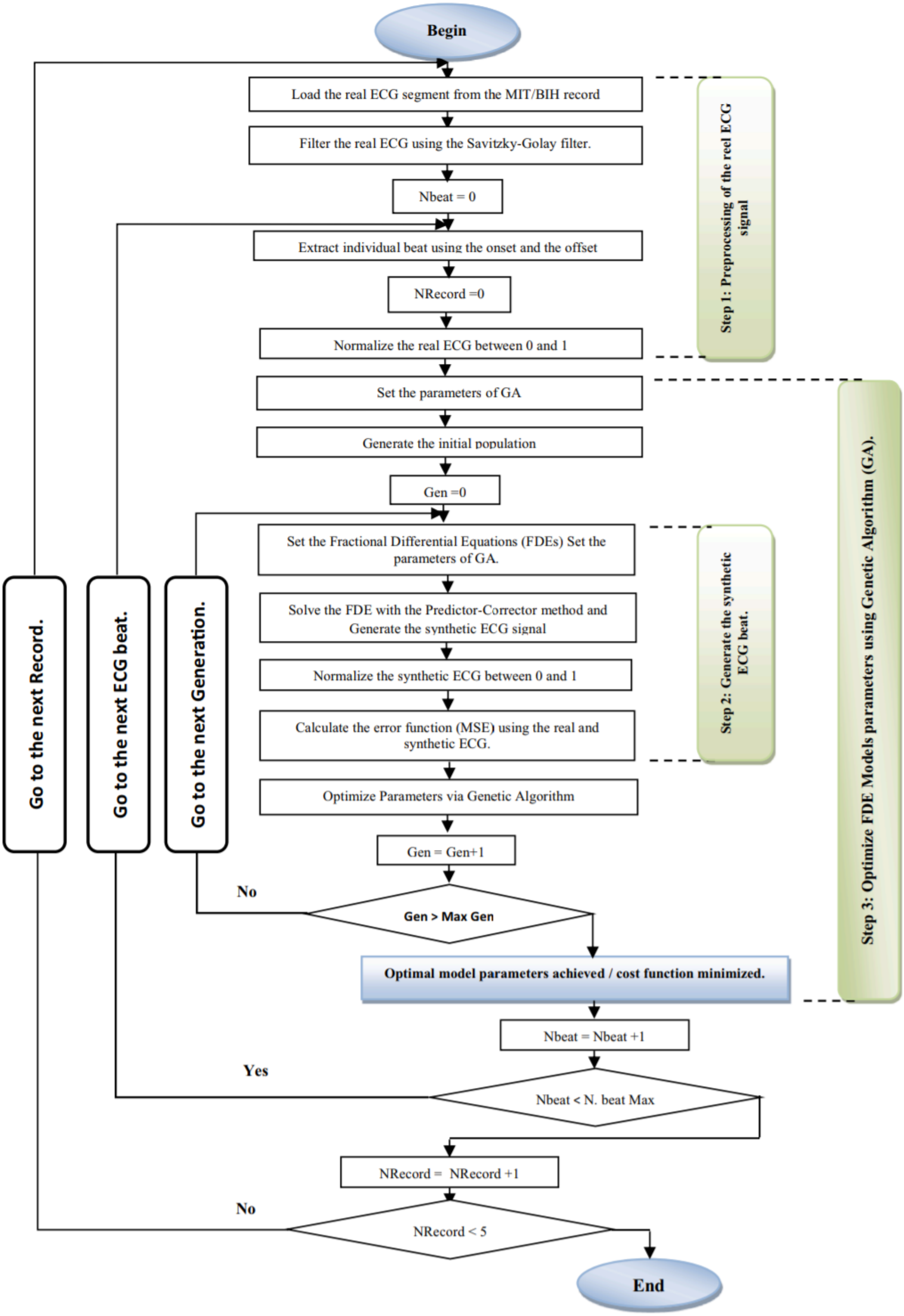

Figure 5.2: Flowchart for Parameter Estimation and Optimization Using Genetic Algorithms [7].

Figure (5.2) illustrates a flowchart with three nested loops, each fulfilling a specific function in the ECG analysis procedure. The outermost loop sequentially retrieves ECG segments from the database. Each segment comprises 100 consecutive cardiac cycles derived from specific recordings as specified in Table 5.4. This loop concludes upon the thorough processing of all accessible recordings.

The second loop, nested within the first, enables beat-by-beat processing. It functions at a maximum of 100 beats (N_{max}), deriving each beat from the beginning and offset of the cardiac cycle. The loop terminates upon the analysis of the designated maximum number of beats.

The innermost loop focuses on optimizing the parameters of the FDE model using a GA. The optimization process persists until the generated population is depleted, as signified by the condition ($\text{Gen} > \text{Gen}_{\text{max}}$). The GA offers a new set of parameters $(a_i, b_i, \theta_i, \alpha_i)$ for the Fractional Differential Equation model during each optimization iteration. The parameters are assessed according to their capacity to provide a model output ($\text{ECG}_{\text{Simulated}}$) that most accurately aligns with the actual ECG signal after the resolution of the fractional equation system. Thus, each repetition requires the resolution of a new system of fractional equations. The process achieves a steady state upon reaching the maximum generation number.

Table 5.5: Settings used in the Genetic Algorithm.

Population Size	**Mutation Rate**	**Max Generations**	**Tolerance**	**Crossover Fraction**
200	0.06	1600	1×10^{-6}	0.8

Table (1.1) in Appendix A comprehensively presents the estimated parameters and corresponding standard deviations for the FDE and IDE models throughout five heartbeats. The examination of Table 1.1 reveals that the fractional order α for the third equation in the FDE model, optimized by the GA, consistently falls between 0.96 and 0.99 across all five types of beats assessed. This range is optimal, as the proposed model improves upon the original IDE model while preserving its essential characteristics. The fractional orders, nearing 1, maintain the fundamental dynamics of the original system while integrating significant improvements in flexibility and precision. This methodology is validated by analyzing the relationship between our fractional model and its predecessor. The IDE model, incorporating an integer-order derivative in the third equation, is a specific example of our more comprehensive fractional model. Allowing a slight deviation from the integer order permits our model to encapsulate the complex nuances of intricate cardiac systems that the traditional model may neglect.

5.3.2.1 Assessment of the FDE Model: Modeling Quality

We utilized optimal parameters to recreate signals for the FDE and IDE models to assess their modelling effectiveness. We assessed the deviation between the original and reconstructed signals utilizing MSE, MAE, RMSE , NRMSE , and the corelation coefficient (CORR), with the formulas for these metrics delineated in Appendix B. Table 5.6 delineates the optimization outcomes for various ECG signals, with the FDE model's results highlighted in bold font. Both models exhibit comparatively low standard deviation (SD) values relative to their metric values. The FDE model frequently exhibits reduced SD values, indicating enhanced robustness.

Table 5.6: Comparison of different metrics across NHB, JHB, RBBB, LBBB, PVC, and Mean Metric.

Metric	**NHB**	**JHB**	**RBBB**	**LBBB**	**PVC**	**Mean Metric (Metric ± SD)**
MAE	0.0176 ± 0.0033 **0.0136 ± 0.0017**	0.0195 ± 0.0047 **0.0107 ± 0.0023**	0.0161 ± 0.0028 **0.0136 ± 0.0023**	0.0207 ± 0.0062 **0.0122 ± 0.0029**	0.0264 ± 0.0029 **0.0289 ± 0.0035**	0.0201 ± 0.0028 **0.0150 ± 0.0014**
MSE ($\times 10^{-4}$)	5.8015 ± 0.4258 **3.6082 ± 0.0861**	6.5017 ± 2.9558 **2.4656 ± 1.1464**	4.6502 ± 1.5748 **3.6165 ± 1.2287**	9.1088 ± 5.4846 **3.7563 ± 1.6985**	14.0000 ± 3.2207 **11.0000 ± 1.1793**	8.0100 ± 2.7300 **4.8900 ± 1.0700**
RMSE	0.0238 ± 0.0040 **0.0189 ± 0.0023**	0.0249 ± 0.0055 **0.0153 ± 0.0036**	0.0213 ± 0.0036 **0.0187 ± 0.0032**	0.0291 ± 0.0082 **0.0189 ± 0.0043**	0.0375 ± 0.0043 **0.0317 ± 0.0018**	0.0273 ± 0.0051 **0.0207 ± 0.0030**
NRMSE	0.0734 ± 0.0120 **0.0586 ± 0.0067**	0.0953 ± 0.0181 **0.0586 ± 0.0130**	0.0863 ± 0.0151 **0.0759 ± 0.0137**	0.0386 ± 0.0113 **0.0251 ± 0.0059**	0.0505 ± 0.0062 **0.0424 ± 0.0025**	0.0688 ± 0.0125 **0.0521 ± 0.0084**
CORR	0.9935 ± 0.0023 **0.9958 ± 0.0011**	0.9957 ± 0.0011 **0.9977 ± 0.0012**	0.9948 ± 0.0017 **0.9959 ± 0.0015**	0.9916 ± 0.0049 **0.9966 ± 0.0016**	0.9896 ± 0.0026 **0.9908 ± 0.0012**	0.9934 ± 0.0025 **0.9954 ± 0.0013**

Using fractional derivatives in the IDE model significantly enhances the representation of ECG beat dynamics. The enhancement was measured by computing the average metrics across beat types for both models and establishing the Enhancement Ratio (ER) as follows:

$$ER = \left(\frac{\text{Metric}_{\text{IDE}} - \text{Metric}_{\text{FDE}}}{\text{Metric}_{\text{IDE}}} \right) \times 100. \tag{5.5}$$

The findings, illustrated in Figure (5.3) and , Table (5.7) indicate that the FDE model consistently surpasses the IDE model in performance. The observed improvements include:

- **21.22%** in Mean Absolute Error (MAE),
- **48.40%** in Mean Squared Error (MSE),
- Approximately **24%** in both Root Mean Squared Error (RMSE) and Normalised Root Mean Squared Error (NRMSE).

The CORR indicates a minimal increase of 0.23% in the FDE model. Both models demonstrate elevated CORR values, signifying robust positive correlations between the modeled and actual ECG signals, with the FDE model typically exhibiting marginally higher correlations.

The findings demonstrate the enhanced accuracy and reliability of the FDE model in modeling various ECG beat types.

Table 5.7: Enhancement ratios (%) illustrating the superiority of the IDE model compared to the FDE model.

Metric	**MAE**	**MSE** ($\times 10^{-6}$)	**RMSE**	**NRMSE**	**CORR**
Enhancement Ratio (%)	21.22	48.40	24.22	24.27	0.23

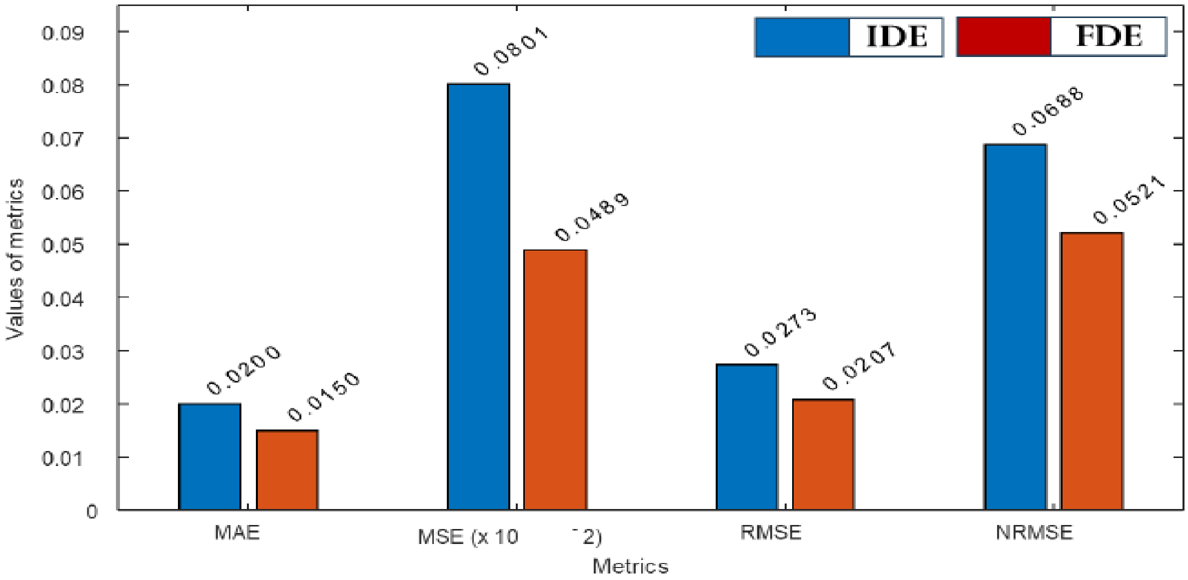

Figure 5.3: Average Metric Value Comparison for FDE and IDE Models [7].

5.4.1.1.1.Comparative analysis of current ECG modeling methodologies. Differences in data sources, evaluation metrics, and methodological variations among studies complicate the comparison of methodologies in the ECG signal modeling literature. This complexity hinders the development of a standardized framework for evaluating and comparing ECG signal modeling quality. We will compare our FDE model with existing approaches, including other FDE-based models and those that employ parameter optimization.

This comparison encompasses research based on fractional differential equations (FDE) [25, 26], as well as studies focused on model parameter optimization [26, 87], as illustrated in Table 5.8. Although FDE-based investigations are relatively novel, they exhibit limitations in terms of evaluative metrics. For example, the study in [25] employs only the MAE, reporting a maximum value of 283.53—significantly higher than the results presented in both the broader literature and our research. Similarly, the work in [26] evaluates its model solely using the MSE and RMSE, whereas our model demonstrates improved performance across both metrics.

Our results in the parameter optimization category are compared with the methods proposed by Awal [87], Awal (2011) [26], and the IDE model [24]. Awal's (2021) method and our FDE model exhibit enhanced performance across various metrics compared to alternative methods. The lowest values for MSE (7.56×10^{-5} and 1.2177×10^{-4}), RMSE (0.00869 and 0.0110), and Normalised RMSE (0.00563 and 0.0357) are achieved, alongside the highest correlation values (0.99907 and 0.9986). The results demonstrate that Awal's (2021) method and our FDE model yield more precise fits to the data and effectively capture ECG signal patterns.

Our model of FDEs exhibits significant advantages. Awal's (2021) static model utilizes two Gaussian procedures, focuses on beat-by-beat modelling, and incorporates a sophisticated array of 35 parameters. Conversely, our methodology employs a more concise parameter set of 16 variables, enhancing computing efficiency. Furthermore, our model maintains the dynamic attributes of the IDE model by incorporating fluctuations in heart rate, PQRST cycle shape, and power spectrum elements of the RR tachogram.

5.3.2.2 Assessment of FDEs Model: Compression Efficiency

We assess the efficiency of the suggested modelling technique for compressing ECG signals by comparing the performance of the FDE model and the IDE model across

Table 5.8: Mean outcomes of several ECG models employed to mimic normal heartbeat.

Metric	**Templos-Hernández [22]**	**Awal (2011) [49]**	**Awal (2021) [50]**	**IDE**	**FDE**
MSE	0.08782	0.00779	7.56×10^{-5}	2.3562×10^{-4}	1.2177×10^{-4}
RMSE	0.2963	0.08826	0.00869	0.0153	0.0110
NRMSE	—	0.02974	0.00563	0.0511	0.0357
CORR	—	0.9205	0.99907	0.9971	0.9986

five categories of beats. This analysis employs three metrics: compression ratio (CR), Percentage Root Mean Square Difference (PRD), and Quality Score (QS). The formulas for these measurements are in Appendix C for reference.

The compression method is implemented on a beat-by-beat basis. The IDE or FDE model parameters represent each heartbeat to capture the beat's morphology rather than the original sample values. The FDE model has 16 parameters, denoted as Np, while the IDE model has 15. The parameters facilitate the generation of the simulated ECG waveform for each heartbeat. The quantity of ECG samples (N) depends on the specific type of heartbeat being analyzed. It is essential to recognize that although the number of parameters is consistent across models (FDE or IDE), the values of these parameters differ for each beat to represent its unique morphology precisely.

We analyzed the optimization of the Compression Ratio (CR) calculation using the formula (Appendix C) by determining the ideal average bit count (N_b) for encoding each parameter. The optimization is essential because the model's parameters have diverse ranges, requiring a representation format that balances signal quality and compression efficiency.

The methodology utilized involved creating synthetic ECG beats using the FDE model with varying decimal precisions for the parameters a_i, b_i, θ_i, and α_i. We evaluated the precision of one, two, and three decimal places, examining the impact of truncation via the PRD metric. Figure 5.4 vividly contrasts genuine ECG beats with their reconstructions at different precision levels, clearly illustrating the relationship between decimal precision and reconstruction fidelity.

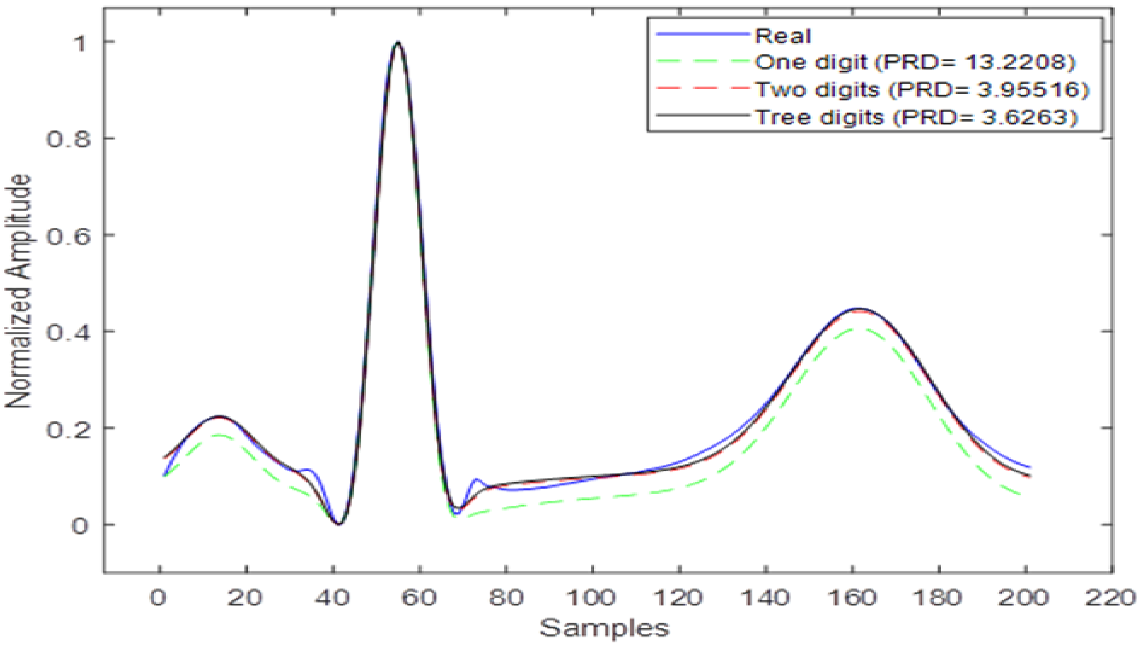

Figure 5.4: Initial values and parameter ranges (lower and upper limits) [7].

The analysis demonstrated that employing two decimal places for a_i, b_i, θ_i, and α_i effectively preserved modeling quality while enhancing compression efficiency. In light of these findings, we determined suitable bit resolutions for encoding each model parameter, as illustrated in Table 5.10, corresponding to the parameter ranges delineated in Table 5.9.

Table 5.9: Parameter Ranges and Initial Values for FDE Model Variables

Variable	a_1	a_2	a_3	a_4	a_5	b_1	b_2	b_3	b_4	b_5	θ_1	θ_2	θ_3	θ_4	θ_5	α
LB	1.27	-11.30	18.05	-10.60	0.85	0.11	0.07	0.11	0.08	0.25	-41.19	-8.54	0.7	10.03	93.28	0.95
UB	3.6	-4.8	25.05	-5.1	1.93	0.16	0.1	0.12	0.11	0.31	-33.09	-6.54	2.99	10.63	114.59	0.99
Initial Value	1.2	-5	30	-7.5	0.75	0.25	0.01	0.1	0.1	0.4	-70	-15	0	15	90	0.96

Our reference, the MIT/BIH arrhythmia database, employs 11 bits to encode each original ECG sample ($N_e = 11$). capable

Figure 5.5 depicts several types of heartbeats along with their respective reconstructed signals from the IDE and FDE models. Table 5.11 encapsulates the compression outcomes for five normal and pathological cardiac beats. The highlighted numbers represent the FDE model, whereas the other values signify the IDE model. The results in Table 5.11 reveal that the FDE model outperforms the IDE model for all analyzed beat types, exhibiting enhanced proficiency in compressing, reconstructing, and maintaining the characteristics of ECG signals.

Table 5.10: Sufficient precision for encoding the FDE model parameters.

Parameters	$a_i[-11.30, 25.05]$	$b_i[0.07, 0.31]$	$\theta_i[-41.19, 114.59]$	$\alpha[0.95, 0.99]$
Total bits	13	8	15	8
$Average number of bit (N_b)$		11		

Table 5.11: Summary of the outcomes for five recordings: CR, PRD, and QS.

Metric	NHB	JHB	RBBB	LBBB	PVC
CR	11.09 **10.40**	8.75 **8.21**	14.09 **13.21**	14.15 **13.27**	10.98 **10.28**
PRD	5.10 **3.56**	6.33 **3.45**	5.41 **4.51**	1.63 **1.30**	5.04 **4.07**
QS	2.17 **2.92**	1.38 **2.37**	2.60 **2.92**	8.68 **10.20**	2.17 **2.52**

5.4.2.2.1. Evaluation of ECG Compression in Comparison with Existing Approaches :

Fig 5.6 presents a comparative analysis of CR, PRD, and QS among different ECG signal compression methodologies, including the FDE model. This comparison provides insights into their efficiency, accuracy, and overall performance in processing ECG signals from the MIT-BIH arrhythmia database.

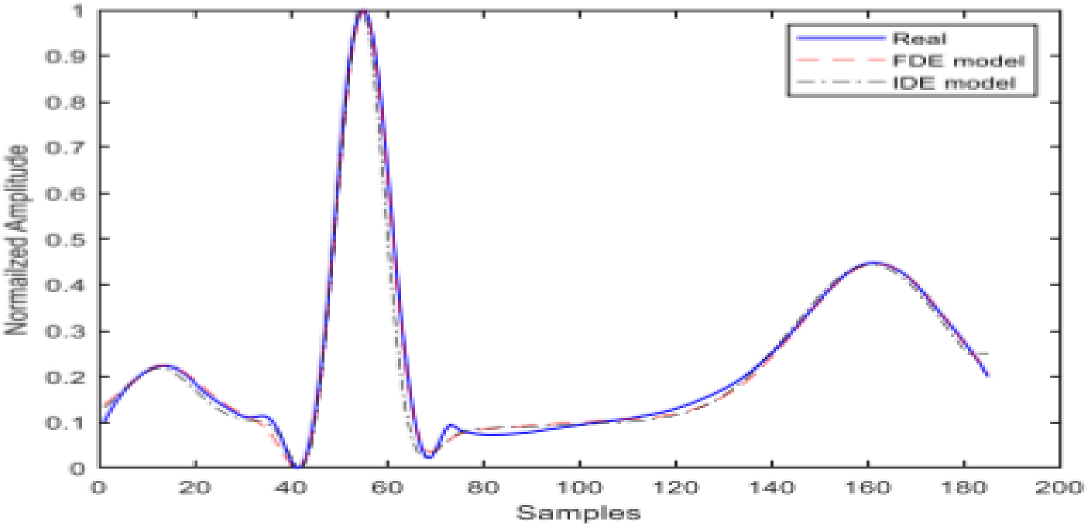

(a) NHB: FDE, CR = 11.56, PRD = 3.56
IDE, CR = 12.33, PRD = 5.10

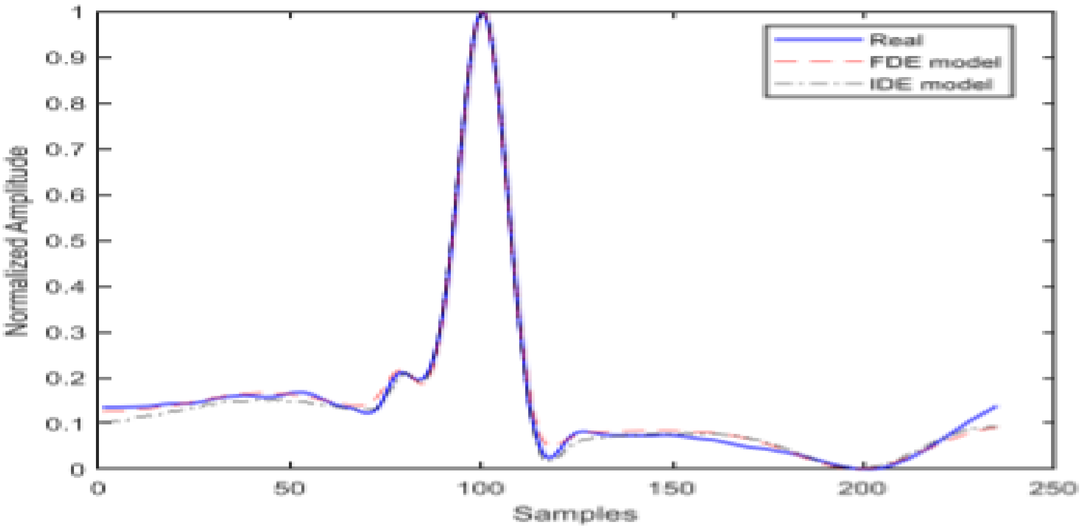

(b) RBBB: FDE, CR = 14.68, PRD = 4.51
IDE, CR = 15.66, PRD = 5.51

Figure 5.5: Reconstructed ECG Signals for Various Heartbeat Types Using IDE and FDE Models: Comparison of Compression Ratio (CR) and Percentage Root Mean Square Difference (PRD) across NHB, RBBB, PVC, JHB, and LBBB beats [7].

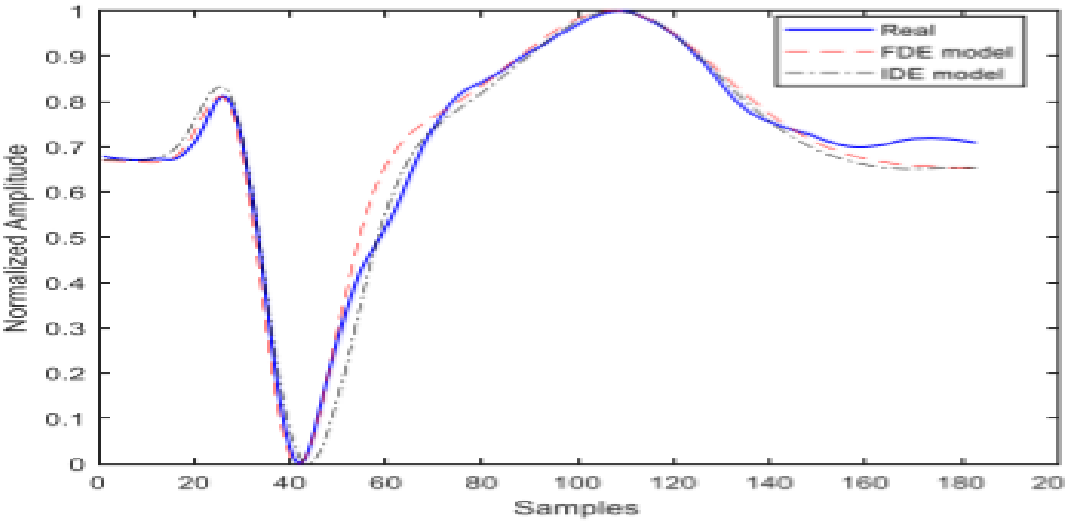

(c) PVC: FDE, CR = 11.43, PRD = 4.07
IDE, CR = 12.20, PRD = 5.04

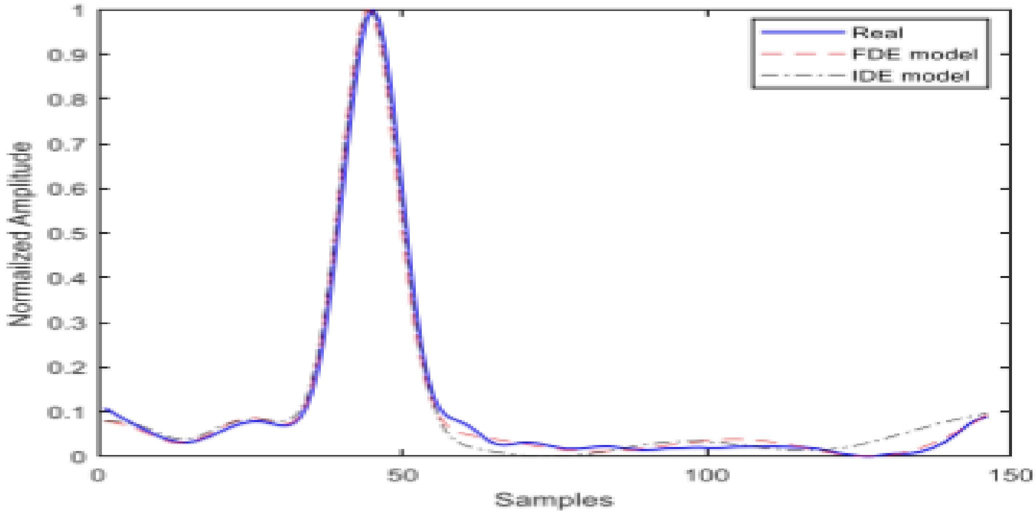

(d) JHB: FDE, CR = 9.13, PRD = 3.45
IDE, CR = 9.73, PRD = 6.33

Figure 5.5: (Continued) Reconstructed ECG Signals Using IDE and FDE Models.

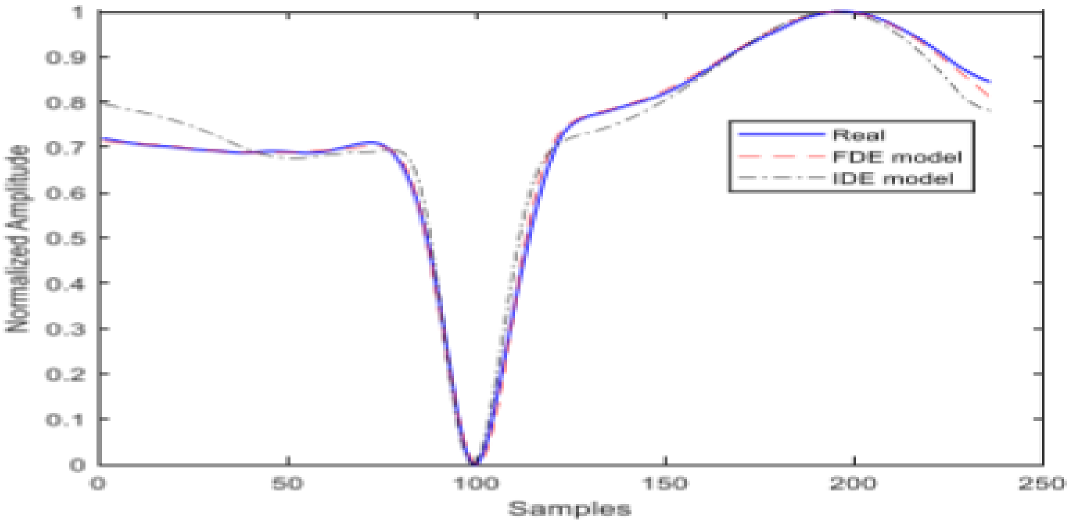

(e) LBBB: FDE, CR = 14.75, PRD = 1.30
IDE, CR = 15.73, PRD = 1.63

Figure 5.5: (Continued) Reconstructed ECG Signals Using IDE and FDE Models.

Figure 5.6 illustrates the CR values as blue bars, reflecting significant variability among the evaluated methods. The Kovacs [115] method attains the maximum compression ratio (CR) of 20.26, signifying exceptional compression efficiency. At the same time, the FDE model exhibits a competitive CR of 10.40, exceeding numerous other strategies documented in the literature. The PRD values, represented by red bars, are consistently low across all approaches, indicating negligible distortion in the reconstructed signals. The FDE model and Talbi [116] demonstrate comparatively lower PRD values of 3.56 and 2.77, respectively, in contrast to other techniques such as Benzid [117] and Kovacs [115]. This indicates that the FDE model attains superior signal retention while ensuring excellent compression efficiency. The QS results, represented as yellow bars, exhibit high consistency across most approaches. The FDE model attains a QS of 2.92, almost approaching Benzid [117]'s 2.96. The elevated QS highlights the superior quality of the reconstructed ECG signal generated by the FDE model. This comparison illustrates that the FDE model attains an outstanding balance between compression efficiency and signal fidelity. It exhibits competitive performance across all metrics—CR, PRD, and QS—when juxtaposed with other recognized methodologies in the literature. The FDE model's capacity to attain elevated compression ratios while preserving little distortion and superior signal quality underscores its efficacy in ECG signal reconstruction and reduction .

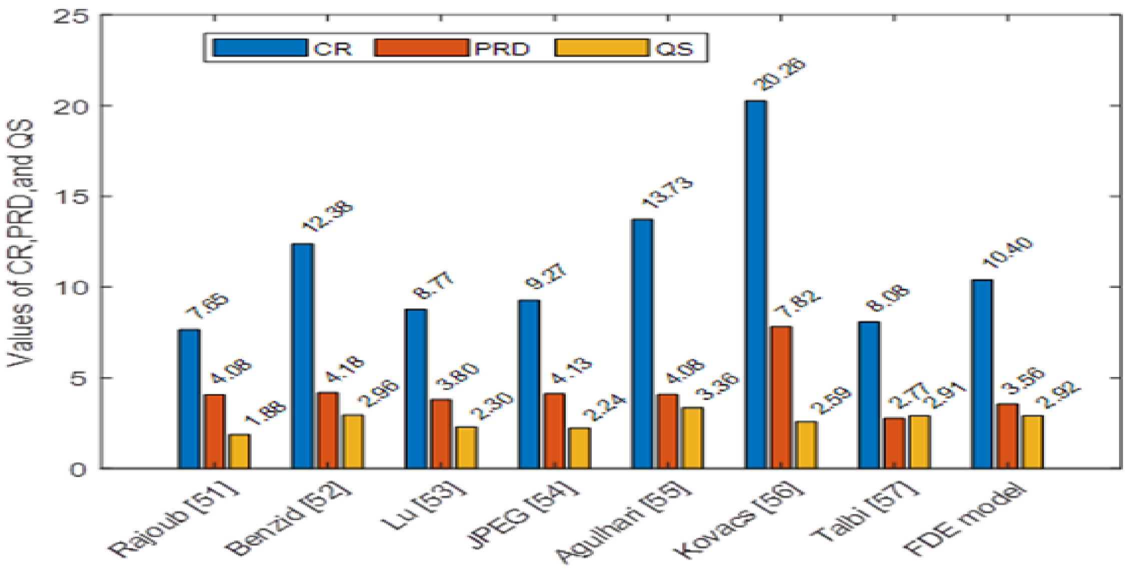

Figure 5.6: Comparison of the performance of the FDE Model with established ECG compression techniques.

5.3.2.3 The constraints of the FDE modelling

FDE modelling offers adaptability and precision for intricate systems but also entails considerable constraints. The fractional operator lacks a well-accepted physical meaning, necessitating that fractional differential equation models be more intuitive than their integer-order equivalents [118, 119]. This hinders the understanding of modelled phenomena. Furthermore, computational complexity is a considerable challenge. Both classical IDE and fractional models require numerical solutions because of significant nonlinearity, complicating the understanding of solution behaviour as the fractional order α varies. Numerical approaches for FDE generally demonstrate increased complexity and processing expense compared to IDE methods. The interpretative difficulties in generalizing IDE to FDE systems [120] hinder precise physical interpretations of the generalized IDE model. Notwithstanding these constraints, fractional models provide more flexibility and precision, producing significant insights into intricate systems, while their physical interpretation may be unclear.

5.4 Conclusion

In this chapter, we developed and validated a fractional-order extension of the McSharry model for ECG signal generation. By introducing a fractional derivative selectively into the third equation—responsible for shaping the PQRST morphology—while maintaining the integer-order structure of the first two equations to preserve the circular limit cycle, the proposed model achieved an improved balance between physiological realism and mathematical flexibility.

Using the PC method to numerically solve the FDEs, and a GA for parameter optimization, the model was evaluated on five types of heartbeats from the MIT/BIH Arrhythmia Database. Results demonstrated a clear enhancement in modeling accuracy, with the fractional-order model achieving a reduction of over 48% in mean squared error and improved compression efficiency compared to the classical integer-order version.

Importantly, the fractional derivative acted as a tunable control over waveform amplitude without affecting RR interval timing, allowing for better adaptation across diverse cardiac morphologies—including pathological beats—while preserving the core dynamics of the McSharry framework. The fractional order remained consistently within the range [0.96, 0.99], showing that even minor deviations from integer-order dynamics can significantly enhance modeling fidelity.

This work validates the application of fractional calculus as a meaningful and practical extension to traditional ECG modeling frameworks. The findings underscore the limitations of purely integer-order systems in capturing the memory-dependent behavior of cardiac activity and demonstrate that fractional-order models can provide a more accurate and compact representation of ECG signals. These results lay the foundation for further exploration of FDE-based modeling in biomedical signal processing, particularly in areas such as diagnostic decision support, personalized modeling, and efficient signal compression.

General Conclusion

This thesis focused on improving ECG signal modeling using differential equations. ECG signals are widely used in medicine to analyze the heart's activity. Creating accurate synthetic ECG signals helps in research, training, and testing medical devices.

In the first part of the work, we studied and improved models based on IDEs. First, we modified the McSharry model by adding a Hopf bifurcation, which made the model generate more realistic heartbeats with natural oscillations. Then, we applied the GWO to automatically adjust the model parameters. This optimization improved the match between simulated ECG signals and real signals from the MIT/BIH database. These two contributions increased the modeling accuracy, but the IDE models still had limits. They were not able to represent long-term memory effects, which are important in real ECG signals.

To solve this problem, we proposed a new model using FDEs . In this model, only the third equation (which controls the PQRST waveform) was replaced with a fractional derivative, while the first two equations remained in integer order. This allowed us to keep the original structure and improve the model's flexibility. We used the PC method to solve the equations and the GA to optimize parameters.

We tested the model on five types of heartbeats from the MIT/BIH Arrhythmia Database. The results showed clear improvements. The fractional-order model reduced the MSE by 48.4% compared to the integer-order model. It also improved compression efficiency by 23.2%, while keeping a high correlation with the original signals. The optimized fractional order values were between 0.96 and 0.99, showing that only a small change in the order gave a strong effect.

In conclusion, this thesis showed that fractional-order models can better simulate ECG signals than classical models. The new approach keeps the advantages of the original McSharry model and adds more flexibility and accuracy. These results support the use of fractional calculus in biomedical signal modeling and open new possibilities for ECG analysis, compression, and clinical applications.

References

[1] Leif Sörnmo and Pablo Laguna. *Bioelectrical signal processing in cardiac and neurological applications.* Academic press, 2005.

[2] Weili Fang, Dongrui Wu, Peter ED Love, Lieyun Ding, and Hanbin Luo. Physiological computing for occupational health and safety in construction: Review, challenges and implications for future research. *Advanced Engineering Informatics*, 54:101729, 2022.

[3] T Lindow, Y Birnbaum, K Nikus, A Maan, U Ekelund, and O Pahlm. Why complicate an important task? an orderly display of the limb leads in the 12-lead electrocardiogram and its implications for recognition of acute coronary syndrome. *BMC Cardiovascular Disorders*, 19:1–8, 2019.

[4] John E Madias. A proposal for a reconstruction (derivation) of v1-v6 using leads i, ii, and a "sternal notch lead": A solution to the problem of non-reproducibility of precordial leads in serial 12-lead standard electrocardiograms. *Journal of Electrocardiology*, 53:109–111, 2019.

[5] A. Takha, M. L. Talbi, and G. Khenichet. Generation of ecg synthetic signal using coupled ordinary differential equations and hopf bifurcation. In *The 1st International Conference on Electronics, Artificial Intelligence and New Technologies*, pages 136–152, 2021.

[6] A. Takha, M. L. Talbi, and G. Khenichet. Optimization of parameters of coupled ordinary differential equations for ecg signal generation using grey wolf optimizer. In *The 1st International Conference on Electronics Engineering, Technology of Telecommunications Advanced Applications*, 2023.

[7] A Takha, , M. L. Talbi, and Ph Ravier. Fractional calculus integration for improved ecg modeling: A mcsharry model expansion. *Medical Engineering & Physics*, 132:104237, 2024.

[8] Pradip Sircar. Parametric modeling of non-stationary signals. *arXiv preprint arXiv:1801.09045*, 2018.

[9] Jagdeep Rahul, Marpe Sora, and Lakhan Dev Sharma. An overview on biomedical signal analysis. *Int. J. Recent Technol. Eng*, 7(5):206–209, 2019.

[10] Karthikeyan Umapathy and Sridhar Krishnan. Non-stationary analysis of pathological signals. *Biomedical Signal Processing and Control*, 1(1):33–40, 2006.

[11] N Jafarnia-Dabanloo, DC McLernon, H Zhang, A Ayatollahi, and V Johari-Majd. A modified zeeman model for producing hrv signals and its application to ecg signal generation. *Journal of theoretical biology*, 244(2):180–189, 2007.

[12] Reza Sameni, Gari D Clifford, Christian Jutten, and Mohammad B Shamsollahi. Multichannel ecg and noise modeling: Application to maternal and fetal ecg signals. *EURASIP Journal on Advances in Signal Processing*, 2007:1–14, 2007.

[13] Gari D Clifford, Shamim Nemati, and Reza Sameni. An artificial vector model for generating abnormal electrocardiographic rhythms. *Physiological measurement*, 31(5):595, 2010.

[14] Ebadollah Kheirati Roonizi and Reza Sameni. Morphological modeling of cardiac signals based on signal decomposition. *Computers in biology and medicine*, 43(10):1453–1461, 2013.

[15] Marian Gidea, Claudia Gidea, and William Byrd. Deterministic models for simulating electrocardiographic signals. *Communications in Nonlinear Science and Numerical Simulation*, 16(10):3871–3880, 2011.

[16] MA Quiroz-Juárez, O Jiménez-Ramírez, R Vázquez-Medina, V Breña-Medina, JL Aragón, and RA Barrio. Generation of ecg signals from a reaction-diffusion model spatially discretized. *Scientific reports*, 9(1):19000, 2019.

[17] Krzysztof Grudziński and Jan J Żebrowski. Modeling cardiac pacemakers with relaxation oscillators. *Physica A: statistical Mechanics and its Applications*, 336(1-2):153–162, 2004.

[18] Mario A Quiroz-Juarez, Omar Jiménez-Ramírez, Ruben Vazquez-Medina, Elena Ryzhii, Maxim Ryzhii, and Jose L Aragon. Cardiac conduction model for generating 12 lead ecg signals with realistic heart rate dynamics. *IEEE transactions on nanobioscience*, 17(4):525–532, 2018.

[19] Elena Ryzhii and Maxim Ryzhii. Modeling of heartbeat dynamics with a system of coupled nonlinear oscillators. In *International Conference on Biomedical Informatics and Technology*, pages 67–75. Springer, 2013.

[20] BZ Kaplan, I Gabay, G Sarafian, and D Sarafian. Biological applications of the “filtered” van der pol oscillator. *Journal of the Franklin Institute*, 345(3):226–232, 2008.

[21] Sandra RFSM Gois and Marcelo A Savi. An analysis of heart rhythm dynamics using a three-coupled oscillator model. *Chaos, Solitons & Fractals*, 41(5):2553–2565, 2009.

[22] Bianca Borem Ferreira, Marcelo Amorim Savi, and Aline Souza de Paula. Chaos control applied to cardiac rhythms represented by ecg signals. *Physica Scripta*, 89(10):105203, 2014.

[23] Elena Ryzhii and Maxim Ryzhii. A heterogeneous coupled oscillator model for simulation of ecg signals. *Computer methods and programs in biomedicine*, 117(1):40–49, 2014.

[24] Patrick E McSharry, Gari D Clifford, Lionel Tarassenko, and Leonard A Smith. A dynamical model for generating synthetic electrocardiogram signals. *IEEE transactions on biomedical engineering*, 50(3):289–294, 2003.

[25] Saptarshi Das and Koushik Maharatna. Fractional dynamical model for the generation of ecg like signals from filtered coupled van-der pol oscillators. *Computer methods and programs in biomedicine*, 112(3):490–507, 2013.

[26] Diana J Templos-Hernandez, Luis A Quezada-Tellez, Brian M Gonzalez-Hernandez, Gerardo Rojas-Vite, Jose E Pineda-Sanchez, Guillermo Fernandez-Anaya, and Erika E Rodriguez-Torres. A fractional-order approach to cardiac rhythm analysis. *Chaos, Solitons & Fractals*, 147:110942, 2021.

[27] Aqeel Ahmad, Muhammad Farman, Parvaiz Ahmad Naik, Nayab Zafar, Ali Akgul, and Muhammad Umer Saleem. Modeling and numerical investigation of fractional-order bovine babesiosis disease. *Numerical Methods for Partial Differential Equations*, 37(3):1946–1964, 2021.

[28] Parvaiz Ahmad Naik. Global dynamics of a fractional-order sir epidemic model with memory. *International journal of biomathematics*, 13(08):2050071, 2020.

[29] Muhammad Bilal Ghori, Parvaiz Ahmad Naik, Jian Zu, Zohreh Eskandari, and Mehraj-ud-din Naik. Global dynamics and bifurcation analysis of a fractional-order seir epidemic model with saturation incidence rate. *Mathematical Methods in the Applied Sciences*, 45(7):3665–3688, 2022.

[30] Parvaiz Ahmad Naik, Kolade M Owolabi, Mehmet Yavuz, and Jian Zu. Chaotic dynamics of a fractional order hiv-1 model involving aids-related cancer cells. *Chaos, Solitons & Fractals*, 140:110272, 2020.

[31] Parvaiz Ahmad Naik, Anum Zehra, Muhammad Farman, Aamir Shehzad, Sundas Shahzeen, and Zhengxin Huang. Forecasting and dynamical modeling of reversible enzymatic reactions with a hybrid proportional fractional derivative. *Frontiers in Physics*, 11:1307307, 2024.

[32] A. C. Guyton and J. E. Hall. *Textbook of Medical Physiology.* W. B. Saunders, Philadelphia, 10th edition, 2000.

[33] A. J. Vander, J. H. Sherman, and D. S. Luciano. *Human Physiology: The Mechanisms of Body Function.* McGraw-Hill, New York, 5th edition, 1990.

[34] J. Enderle. Bioelectric phenomena. In J. Enderle, S. Blanchard, and J. Bronzino, editors, *Introduction to Biomedical Engineering*, chapter 3, pages 79–138. Academic Press, San Diego, 2000.

[35] R. Plonsey and R. C. Barr. *Bioelectric Phenomena: A Quantitative Approach.* Plenum, New York, 1988.

[36] Jaakko Malmivuo and Robert Plonsey. *Bioelectromagnetism: principles and applications of bioelectric and biomagnetic fields.* Oxford University Press, USA, 1995.

[37] R. M. Gulrajani. *Bioelectricity and Biomagnetism.* John Wiley & Sons, Montreal, 1998.

[38] K Ahlbeck, K Fredriksson, O Rooyackers, G Måbäck, S Remahl, T Ansved, L Eriksson, and P Radell. Signs of critical illness polyneuropathy and myopathy can be seen early in the icu course. *Acta anaesthesiologica scandinavica*, 53(6):717–723, 2009.

[39] Arto Tennilä, Tapani Salmi, Ville Pettilä, Risto O Roine, Tero Varpula, and Olli Takkunen. Early signs of critical illness polyneuropathy in icu patients with systemic inflammatory response syndrome or sepsis. *Intensive care medicine*, 26:1360–1363, 2000.

[40] Rangaraj M Rangayyan and Sridhar Krishnan. *Biomedical signal analysis.* John Wiley & Sons, 2024.

[41] RG Mark, PS Schluter, GB Moody, PH Devlin, and D Chernoff. An annotated ecg database for evaluating arrhythmia detectors. In *Proceedings of IEEE Frontiers in Engineering and Health Care*, pages 205–210. IEEE, 1982.

[42] GB Moody and RG Mark. The impact of the mit-bih arrhythmia database: History, lessons learned, and its influence on current and future databases. *IEEE Engineering in Medicine and Biology Magazine*, 20(3):45–50, 2001.

[43] RE Hermes, DB Geselowitz, and GC Oliver. Development, distribution, and use of the american heart association database for ventricular arrhythmia detector evaluation. In *Proceedings of Computers in Cardiology*, pages 263–266. IEEE Computer Society Press, 1980.

[44] Alessandro Taddei, G Distante, M Emdin, P Pisani, GB Moody, C Zeelenberg, and C Marchesi. The european st-t database: standard for evaluating systems for the analysis of st-t changes in ambulatory electrocardiography. *European heart journal*, 13(9):1164–1172, 1992.

[45] FJ Jager, A Taddei, GB Moody, M Emdin, G Antolič, R Dorn, A Smrdel, C Marchesi, and RG Mark. Long-term st database: A reference for the development and evaluation of automated ischaemia detectors and for the study of the dynamics of my-

ocardial ischaemia. *Medical and Biological Engineering and Computing*, 41(2):172–183, 2003.

[46] GB Moody, WK Muldrow, and RG Mark. A noise stress test for arrhythmia detectors. In *Proceedings of Computers in Cardiology*, pages 381–384. IEEE Computer Society Press, 1984.

[47] Y Ichimaru and GB Moody. Development of the polysomnographic database on cd-rom. *Psychiatry and Clinical Neurosciences*, 53:175–177, 1999.

[48] G Klösch, B Kemp, T Penzel, A Schlögl, P Rappelsberger, E Trenker, G Gruber, J Zeitlhofer, B Saletu, WM Herrmann, et al. The siesta project polygraphic and clinical database. *IEEE Engineering in Medicine and Biology Magazine*, 20:51–57, 2001.

[49] GB Moody, RG Mark, and AL Goldberger. Physionet: A web-based resource for study of physiologic signals. *IEEE Engineering in Medicine and Biology Magazine*, 20:70–75, 2001.

[50] P.W. Macfarlane and T.D.W. Lawrie, editors. *Comprehensive Electrocardiology: Theory and Practice in Health and Disease*, volume 1-3. Pergamon Press, New York, 1989.

[51] R.L. Lux. Mapping techniques. In P.W. Macfarlane and T.D.W. Lawrie, editors, *Comprehensive Electrocardiology: Theory and Practice in Health and Disease (Vol. 2)*, chapter 26, pages 1001–1014. Pergamon Press, New York, 1989.

[52] L. De Ambroggi, E. Musso, and B. Taccardi. Body-surface mapping. In P.W. Macfarlane and T.D.W. Lawrie, editors, *Comprehensive Electrocardiology: Theory and Practice in Health and Disease (Vol. 2)*, chapter 27, pages 1015–1049. Pergamon Press, New York, 1989.

[53] D.H. Brooks and R.S. MacLeod. Electrical imaging of the heart. *IEEE Signal Processing Magazine*, 14:24–42, 1997.

[54] J.M. Jenkins and S.A. Caswell. Detection algorithms in implantable cardioverter defibrillators. *Proceedings of the IEEE*, 84:428–445, 1996.

[55] Frank N Wilson, Franklin D Johnston, A Garrard Macleod, and Paul S Barker. Electrocardiograms that represent the potential variations of a single electrode. *American Heart Journal*, 9(4):447–458, 1934.

[56] Emanuel Goldberger. A simple, indifferent, electrocardiographic electrode of zero potential and a technique of obtaining augmented, unipolar, extremity leads. *American Heart Journal*, 23(4):483–492, 1942.

[57] M. Malik and A. J. Camm, editors. *Heart Rate Variability.* Futura Publishing Co., Armonk, 1995.

[58] R. E. Kleiger, J. P. Miller, J. T. Bigger, and A. J. Moss. Decreased heart rate variability and its association with increased mortality after myocardial infarction. *American Journal of Cardiology*, 59:256–262, 1987.

[59] D. Andresen, T. Brüggemann, S. Behrens, and C. Ehlers. Heart rate response to provocative maneuvers. In M. Malik and A. J. Camm, editors, *Heart Rate Variability*, chapter 21, pages 267–274. Futura Publishing Co., Armonk, 1995.

[60] Shantanu Das. *Functional fractional calculus*, volume 1. Springer, 2011.

[61] KS Miller. An introduction to the fractional calculus and fractional differential equations. *John Wiley & Sons*, 1993.

[62] Igor Podlubny. *Fractional differential equations: an introduction to fractional derivatives, fractional differential equations, to methods of their solution and some of their applications.* elsevier, 1998.

[63] Rudolf Gorenflo and Francesco Mainardi. *Fractional calculus: integral and differential equations of fractional order.* Springer, 1997.

[64] Anatoliĭ Aleksandrovich Kilbas, Hari M Srivastava, and Juan J Trujillo. *Theory and applications of fractional differential equations*, volume 204. Elsevier, Amsterdam, 2006.

[65] Mabrouk BRAGDI. *On the theory and applications of fractional differential equations.* PhD thesis, Ecole normale supérieure de Kouba-Mohamed Bachir El Ibrahimi-
.

[66] Alan Freed, Kai Diethelm, and Yury Luchko. Fractional-order viscoelasticity (fov): Constitutive development using the fractional calculus: First annual report. Technical report, 2002.

[67] Igor Podlubny. Fractional differential equations, mathematics in science and engineering, 1999.

[68] F Mainardi. Fractional calculus and waves in linear viscoelasticity, imperial college press, london. 2010.

[69] Stefan G Samko. Fractional integrals and derivatives. *Theory and applications*, 1993.

[70] Francesco Mainardi and Rudolf Gorenflo. Time-fractional derivatives in relaxation processes: a tutorial survey. *arXiv preprint arXiv:0801.4914*, 2008.

[71] Kai Diethelm and Neville J Ford. Analysis of fractional differential equations. *Journal of Mathematical Analysis and Applications*, 265(2):229–248, 2002.

[72] Rudolf Hilfer et al. Threefold introduction to fractional derivatives. *Anomalous transport: Foundations and applications*, pages 17–73, 2008.

[73] D Constantinescu and M Stoicescu. Fractal dynamics as long range memory modeling technique. *Physics AUC*, 21:114–120, 2011.

[74] Victor Guillemin. Im gel′ fand and ge shilov, generalized functions. 1980.

[75] Roberto Garrappa. Numerical solution of fractional differential equations: A survey and a software tutorial. *Mathematics*, 6(2):16, 2018.

[76] Roberto Garrappa. A short course on computational techniques for fractional models. *ComputationalMethods_FractionalCalculus_Dhahran. pdf*, 2018.

[77] Ch Lubich. Runge-kutta theory for volterra and abel integral equations of the second kind. *Mathematics of computation*, 41(163):87–102, 1983.

[78] Yue Han, Dusit Niyato, Cyril Leung, Chunyan Miao, and Dong In Kim. Dynamics in coded edge computing for iot: A fractional evolutionary game approach. *IEEE Internet of Things Journal*, 9(15):13978–13994, 2022.

[79] Andrew Young. Approximate product-integration. *Proceedings of the Royal Society of London. Series A. Mathematical and Physical Sciences*, 224(1159):552–561, 1954.

[80] K. Diethelm and A. D. Freed. The fracpece subroutine for the numerical solution of differential equations of fractional order. In F. Keil, W. Mackens, H. Voß, and J. Werther, editors, *Scientific Computing in Chemical Engineering II: Computational Fluid Dynamics, Reaction Engineering, and Molecular Properties*, pages 57–71. Springer-Verlag, 1999.

[81] Kai Diethelm, Neville J Ford, and Alan D Freed. Detailed error analysis for a fractional adams method. *Numerical algorithms*, 36:31–52, 2004.

[82] Kai Diethelm, Neville J Ford, and Alan D Freed. A predictor-corrector approach for the numerical solution of fractional differential equations. *Nonlinear Dynamics*, 29:3–22, 2002.

[83] Kai Diethelm. Efficient solution of multi-term fractional differential equations using p (ec) m e methods. *Computing*, 71:305–319, 2003.

[84] Roberto Garrappa. On linear stability of predictor–corrector algorithms for fractional differential equations. *International Journal of Computer Mathematics*, 87(10):2281–2290, 2010.

[85] Ch Lubich. Discretized fractional calculus. *SIAM Journal on Mathematical Analysis*, 17(3):704–719, 1986.

[86] Christian Lubich. Convolution quadrature and discretized operational calculus. i. *Numerische Mathematik*, 52(2):129–145, 1988.

[87] Md Abdul Awal, Sheikh Shanawaz Mostafa, Mohiuddin Ahmad, Mohammad Ashik Alahe, Mohd Abdur Rashid, Abbas Z Kouzani, and MA Parvez Mahmud. Design and optimization of ecg modeling for generating different cardiac dysrhythmias. *Sensors*, 21(5):1638, 2021.

[88] Mark Potse. Mathematical modeling and simulation of ventricular activation sequences: implications for cardiac resynchronization therapy. *Journal of cardiovascular translational research*, 5:146–158, 2012.

[89] Rachanart Soontornvorn, Hiroyuki Fujioka, Vanvisa Chutchavong, and Kanok Janchitrapongvej. Modeling ecg waveform using optimal smoothing bézier-bernstein curves. In *TENCON 2017-2017 IEEE Region 10 Conference*, pages 1235–1238. IEEE, 2017.

[90] R Sassi, LT Mainardi, P Maison Blanche, Sergio Cerutti, et al. Estimation of spectral parameters of residual ecg signal during atrial fibrillation using autoregressive models. *Folia Cardiologica*, 12(suppl. C):108–110, 2005.

[91] Ebadollah Kheirati Roonizi and Roberto Sassi. A signal decomposition model-based bayesian framework for ecg components separation. *IEEE Transactions on Signal Processing*, 64(3):665–674, 2015.

[92] Zheying Li and Minjie Ma. Ecg modeling with dfg. In *2005 IEEE Engineering in Medicine and Biology 27th Annual Conference*, pages 2691–2694. IEEE, 2006.

[93] Mitsuo Gen and Runwei Cheng. *Genetic algorithms and engineering optimization*, volume 7. John Wiley & Sons, 1999.

[94] David E Golberg. Genetic algorithms in search, optimization, and machine learning. *Addion wesley*, 1989(102):36, 1989.

[95] Yorgos Goletsis, Costas Papaloukas, Dimitrios I Fotiadis, Aristidis Likas, and Lampros K Michalis. Automated ischemic beat classification using genetic algorithms and multicriteria decision analysis. *IEEE transactions on Biomedical Engineering*, 51(10):1717–1725, 2004.

[96] Mitsuo Gen, Runwei Cheng, and Lin Lin. *Network models and optimization: Multiobjective genetic algorithm approach*. Springer Science & Business Media, 2008.

[97] David E Goldberg. Genetic algorithm in search, optimization and machine learning, addison. *W esley Publishing Company, R eading, MA*, 1(98):9, 1989.

[98] NG Bhuvaneswari Amma. Cardiovascular disease prediction system using genetic algorithm and neural network. In *2012 international conference on computing, communication and applications*, pages 1–5. IEEE, 2012.

[99] Seyedali Mirjalili, Seyed Mohammad Mirjalili, and Andrew Lewis. Grey wolf optimizer. *Advances in engineering software*, 69:46–61, 2014.

[100] NM Hatta, Azlan Mohd Zain, Roselina Sallehuddin, Z Shayfull, and Yusliza Yusoff. Recent studies on optimisation method of grey wolf optimiser (gwo): a review (2014–2017). *Artificial intelligence review*, 52:2651–2683, 2019.

[101] Xianhai Song, Li Tang, Sutao Zhao, Xueqiang Zhang, Lei Li, Jianquan Huang, and Wei Cai. Grey wolf optimizer for parameter estimation in surface waves. *Soil Dynamics and Earthquake Engineering*, 75:147–157, 2015.

[102] HA Deepak and T Vijayakumar. Optimal threshold estimation using grey wolf optimization for emd-dtcwt based ecg denoising. *International Journal of Recent Technology and Engineering*, 2020.

[103] Muhammad Suhail Shaikh, Changchun Hua, Munsif Ali Jatoi, Muhammad Mohsin Ansari, and Aleem Ahmed Qader. Application of grey wolf optimisation algorithm in parameter calculation of overhead transmission line system. *IET Science, Measurement & Technology*, 15(2):218–231, 2021.

[104] Heba Al Nsour, Mohammed Alweshah, Abdelaziz I Hammouri, Hussein Al Ofeishat, and Seyedali Mirjalili. A hybrid grey wolf optimiser algorithm for solving time series classification problems. *Journal of Intelligent Systems*, 29(1):846–857, 2019.

[105] Hossam Faris, Ibrahim Aljarah, Mohammed Azmi Al-Betar, and Seyedali Mirjalili. Grey wolf optimizer: a review of recent variants and applications. *Neural computing and applications*, 30:413–435, 2018.

[106] Hans Jürgen Korsch, Hans-Jörg Jodl, and Timo Hartmann. *Chaos: a program collection for the PC*. Springer Science & Business Media, 2007.

[107] PhysioNet. Ptb diagnostic ecg database, 2024. Accessed: 16-Nov-2024.

[108] Mohammad Hossein Vafaie, Mohammad Ataei, and Hamid Reza Koofigar. Heart diseases prediction based on ecg signals' classification using a genetic-fuzzy system and dynamical model of ecg signals. *Biomedical Signal Processing and Control*, 14:291–296, 2014.

[109] Hongqiang Li, Danyang Yuan, Xiangdong Ma, Dianyin Cui, and Lu Cao. Genetic algorithm for the optimization of features and neural networks in ecg signals classification. *Scientific reports*, 7(1):41011, 2017.

[110] Hamed Danandeh Hesar and Amin Danandeh Hesar. Ecg enhancement using a modified bayesian framework and particle swarm optimization. *Biomedical Signal Processing and Control*, 80:104280, 2023.

[111] S Suja Priyadharsini and S Edward Rajan. An efficient method for the removal of ecg artifact from measured eeg signal using pso algorithm. *Int J Adv Soft Comput Appl*, 6(1):1–19, 2014.

[112] GB Moody. Mit-bih arrhythmia database directory; hypertext edition, 24 may 1997 (based on the printed third edition, 23 july 1992); harvard-mit division of health sciences and technology. *Biomedical Engineering Center: Cambridge, MA, USA*, 1997.

[113] Deepshikha Acharya, Asha Rani, Shivangi Agarwal, and Vijander Singh. Application of adaptive savitzky–golay filter for eeg signal processing. *Perspectives in science*, 8:677–679, 2016.

[114] Fars Samann and Thomas Schanze. An efficient ecg denoising method using discrete wavelet with savitzky-golay filter. *Current Directions in Biomedical Engineering*, 5(1):385–387, 2019.

[115] Péter Kovács, Sándor Fridli, and Ferenc Schipp. Generalized rational variable projection with application in ecg compression. *IEEE Transactions on Signal Processing*, 68:478–492, 2019.

[116] Mohamed Lamine Talbi and Philippe Ravier. Flexible ecg signal modeling and compression using alpha stable functions. *Medical Engineering & Physics*, 109:103865, 2022.

[117] Redha Benzid, Farid Marir, and Nour-Eddine Bouguechal. Quality-controlled compression method using wavelet transform for electrocardiogram signals. *International Journal of Biomedical Sciences*, 1(1):1306–1216, 2006.

[118] Manuel Duarte Ortigueira. *Fractional calculus for scientists and engineers*, volume 84. Springer Science & Business Media, 2011.

[119] Anatoly Kochubei and Yuri Luchko. *Basic theory.* Walter de Gruyter GmbH & Co KG, 2019.

[120] Dumitru Baleanu, Kai Diethelm, Enrico Scalas, and Juan J Trujillo. *Fractional calculus: models and numerical methods*, volume 3. World Scientific, 2012.

Appendix A

Estimated parameter values and their standard deviations

Tables 1.1 and 1.2 present a summary of the estimated parameters and their standard deviations for five categories of beats within the frameworks of Fractional Differential Equations (FDE) and Integer Differential Equations (IDE) employing the genetic algorithm.

Table 1.1: Summary of Estimated Parameters and Their Variances Obtained via Genetic Algorithm in the Context of Fractional Differential Equation Modeling.

	a_1	a_2	a_3	a_4	a_5	b_1	b_2	b_3	b_4	b_5	θ_1	θ_2	θ_3	θ_4	θ_5	α
106 NHB	2.3381± 0.5306	−7.3515± 1.0907	22.7330± 1.7249	−8.9591± 0.9750	1.2364± 0.1547	0.1455± 0.0065	0.0857± 0.0080	0.1116± 0.0044	0.0974± 0.0076	0.2780± 0.0111	−36.9304± 1.6428	−8.4180± 0.5291	1.9862± 0.4842	10.0192± 0.1179	102.6030± 4.2158	0.9633± 0.0075
234 JHB	−0.6962± 0.1876	0.9981± 0.3179	16.2286± 3.5275	−0.1385± 0.0369	0.3028± 0.0591	0.1174± 0.0344	0.0952± 0.0091	0.0861± 0.0045	0.3458± 0.0024	0.3028± 0.0377	−36.2200± 2.9290	−11.0003± 0.1999	−1.9773± 0.3314	39.5157± 1.0000	83.3243± 5.4442	0.9827± 0.0000
207 LBBB	−0.0786± 0.0011	1.3656± 0.0131	−10.8727± 0.9108	1.1810± 0.0000	0.4319± 0.0024	0.2875± 0.0031	0.1439± 0.0000	0.1571± 0.0004	0.1199± 0.0000	0.5483± 0.0008	−60.3279± 1.7395	−13.8467± 1.4213	−0.5555± 0.0708	12.2608± 0.7774	95.5465± 18.2620	0.9846± 0.0001
124 RBBB	0.0919± 0.0109	3.6092± 0.2892	15.7987± 0.7028	−1.9138± 0.3478	0.2414± 0.0205	0.3050± 0.0092	0.0698± 0.0009	0.1073± 0.0000	0.0802± 0.0000	0.2919± 0.0088	−55.9112± 0.0000	−20.8367± 0.5514	0.4463± 0.2268	15.2166± 0.7109	99.6059± 2.0935	0.9944± 0.0056
208 PVC	5.999± 0.9639	0.0000± 0.0000	−10.6160± 0.1481	0.0000± 0.0000	0.4952± 0.2507	0.1491± 0.0102	0.0000± 0.0000	0.1615± 0.0148	0.0000± 0.0000	0.4122± 0.1128	−5.2979± 0.0073	21.0547± 0.0120	0.1598± 0.6654	13.7408± 0.0000	70.0185± 6.2936	0.9930± 0.0000

Table 1.2: Summary of Estimated Parameters and Their Variances Obtained via Genetic Algorithm in the Context of Integer Differential Equation Modeling.

	a_1	a_2	a_3	a_4	a_5	b_1	b_2	b_3	b_4	b_5	θ_1	θ_2	θ_3	θ_4	θ_5
106 NHB	1.8494± 0.1336	−3.0054± 0.2773	19.4776± 5.6322	−6.0926± 1.5298	0.8218± 0.0141	0.2005± 0.0004	0.1000± 0.0000	0.1360± 0.0000	0.1193± 0.0001	0.3952± 0.0003	−52.2695± 4.4681	−15.9036± 0.1873	2.7185± 0.0991	15.0161± 0.0001	143.4385± 34.4824
234 JHB	−0.9500± 0.0135	−0.8640± 0.0398	17.0205± 4.3352	−0.1459± 0.0004	−0.1759± 0.0025	0.1220± 0.0001	0.1025± 0.0000	0.1162± 0.0000	0.3364± 0.0000	0.3881± 0.0009	−48.6384± 4.7971	−14.3166± 5.2208	−2.6669± 0.2037	40.3728± 0.2001	103.0777± 43.7185
207 LBBB	−0.2971± 0.1403	0.4857± 0.1281	−6.0000± 0.0000	−6.5000± 0.0000	0.4297± 0.1847	0.2289± 0.0973	0.0940± 0.0150	0.1912± 0.0247	0.0932± 0.0149	0.6886± 0.0750	−70.0000± 0.0000	−12.0000± 0.0000	0.0000± 0.0000	12.0000± 0.0000	115.0000± 0.0000
124 RBBB	0.1286± 0.0001	3.1402± 0.0980	9.9911± 0.1244	−2.9329± 0.3995	−0.1690± 0.0003	0.3799± 0.0005	0.0991± 0.0000	0.1600± 0.0000	0.1292± 0.0000	0.4073± 0.0000	−84.0819± 13.0021	−30.4213± 1.4798	0.8416± 0.1720	17.8264± 6.6439	136.5064± 15.1598
208 PVC	6.9701± 0.0000	0.0000± 0.0000	−9.6160± 0.0000	0.0000± 0.0000	0.5813± 0.0844	0.1545± 0.0100	0.0000± 0.0000	0.1872± 0.0098	0.0000± 0.0000	0.4440± 0.0899	−7.5979± 0.0000	−20.0547± 0.0000	2.0122± 0.1057	11.7408± 0.0000	100.9185± 0.0000

Appendix B

Measure of distortion

ECG_real refers to the ECG signal taken from the MIT-BIH database, while ECG_simulated signifies the synthetic signal generated by the fractional model. N denotes the number of discrete time points or samples within each ECG beat.

The mean-absolute-error (MAE) is given by:

$$\mathrm{MAE} = \frac{1}{n}\sum_{i=1}^{n}\left|\mathrm{ECG}_{\mathrm{real},i} - \mathrm{ECG}_{\mathrm{simulated},i}\right|$$

where n is the quantity of samples.

The mean square error (MSE) is given by:

$$\mathrm{MSE} = \frac{1}{n}\sum_{i=1}^{n}\left(\mathrm{ECG}_{\mathrm{real},i} - \mathrm{ECG}_{\mathrm{simulated},i}\right)^2$$

Another metric is the root mean square error (RMSE), computed as follows:

$$\mathrm{RMSE} = \sqrt{\frac{1}{n}\sum_{i=1}^{n}\left(\mathrm{ECG}_{\mathrm{real},i} - \mathrm{ECG}_{\mathrm{simulated},i}\right)^2}$$

The Normalized RMSE (NRMSE) is:

$$\mathrm{NRMSE} = \sqrt{\frac{\sum_{i=1}^{n}\left(\mathrm{ECG}_{\mathrm{real},i} - \mathrm{ECG}_{\mathrm{simulated},i}\right)^2}{\sum_{i=1}^{n}\mathrm{ECG}_{\mathrm{real},i}^2}}$$

The Correlation Coefficient (CORR) is the Pearson correlation coefficient, calculated as:

$$\mathrm{CORR} = \frac{\sum \left(\mathrm{ECG}_{\mathrm{real},i} - \mu_{\mathrm{real}}\right)\left(\mathrm{ECG}_{\mathrm{simulated},i} - \mu_{\mathrm{simulated}}\right)}{\sigma_{\mathrm{real}} \cdot \sigma_{\mathrm{simulated}}}$$

Where μ_{real} and $\mu_{\mathrm{simulated}}$ denote the means, while σ_{real} and $\sigma_{\mathrm{simulated}}$ represent the standard deviations of the actual and simulated ECG signals, respectively.

Appendix C

Analysis of Compression Ratio (CR) and Percent Root-Mean-Square Difference (PRD)

The Compression Ratio (CR)

The compression ratio (CR) is the proportion of the original signal size to the size of the compressed signal. The CR formula is delineated as follows:

$$\mathrm{CR} = \frac{N \cdot N_e}{N_b \cdot N_p}$$

where:

- N represents the quantity of ECG beat samples,
- N_e signifies the number of bits allocated for encoding each ECG sample,
- N_p indicates the number of model parameters,
- N_b denotes the number of bits designated for encoding each parameter.

The Percent Root-Mean-Square Difference (PRD)

The PRD measures the disparity between the original signal $\mathrm{ECG}_{\mathrm{real}}(n)$ and the reconstructed signal $\mathrm{ECG}_{\mathrm{simulated}}(n)$ following compression. The PRD formula is as follows:

$$\mathrm{PRD}(\%) = \sqrt{\frac{\sum_{i=1}^{n} \left(\mathrm{ECG}_{\mathrm{real},i} - \mathrm{ECG}_{\mathrm{simulated},i}\right)^2}{\sum_{i=1}^{n} \mathrm{ECG}_{\mathrm{real},i}^2}} \times 100$$

The Quality Score (QS)

The Quality Score (QS) quantifies performance as the ratio of the compression ratio to the Percent Root-Mean-Square Difference (PRD), and is calculated using the following expression:

$$\mathrm{QS} = \frac{\mathrm{CR}}{\mathrm{PRD}}$$